Theory, Design and Development of Artificial Magnetic Materials

by

Leila Yousefi

A thesis
presented to the University of Waterloo
in fulfillment of the
thesis requirement for the degree of
Doctor of Philosophy
in
Electrical and Computer Engineering

Waterloo, Ontario, Canada, 2009

Abstract

Artificial Magnetic Materials (AMMs) are a subgroup of metamaterials which are engineered to provide desirable magnetic properties not seen in natural materials. These artificial structures are designed to provide either negative or enhanced positive (higher than one) relative permeability. AMMs with negative permeability are used to develop Single Negative (SNG), or Double Negative (DNG) metamaterials. AMMs with enhanced positive permeability are used to provide magneto-dielectric materials at microwave frequencies where the natural magnetic materials fail to work efficiently. AMMs are realized by embedding metallic resonators in a host dielectric. These inclusions provide desirable magnetic properties near their resonance frequency.

Artificial magnetic materials used as SNG, or DNG have many applications such as: sub-wavelength cavity resonators, sub-wavelength parallel-plate wave guides, sub-wavelength cylindrical and spherical coreshell systems, efficient electrically small dipole antennas, super lenses, THz active devices, sensitivity enhancement near-field probes using double and single negative media, and mutual coupling reduction between antennas. On the other hand, artificial magnetic materials used as magneto-dielectrics have other applications in developing enhanced bandwidth efficient miniaturized antennas, low profile enhanced gain antennas using artificial magnetic superstrates, wide band woodpile Electromagnetic Band Gap (EBG) structures, EBGs with enhanced in-phase reflection bandwidth used as artificial magnetic ground planes.

In this thesis, several advances are added to the existing knowledge of developing artificial magnetic materials, in terms of analytical modeling, applications, realization, and experimental characterization.

To realize AMMs with miniaturized unit cells, new inclusions based on fractal Hilbert curves are introduced, and analyzed. Analytical models, numerical full wave simulation, and experimental characterization are used to analyze, and study the new structures. A comprehensive comparison is made between the new inclusions, and perviously developed inclusions in terms of electromagnetic properties. The new inclusions have advantages of miniaturization, and less dispersion when compared to the existing structures in the literature.

To realize multi-band AMMs, unit cells with multiple inclusions are proposed, designed, and analyzed. The new unit cells can be designed to give the desired magnetic properties either over distinguished multiple frequency bands, or over a single wide frequency band. Numerical full wave simulation is used to verify the proposed concept, and analytical models are provided for design, and optimization of the new unit cells. Unit cells with different configurations are optimized to get a wideband responce for the effective permeability. Space mapping technique is used to provide a link between analytically optimized structures, and full wave numerical simulation results.

Two new methods are proposed for experimental characterization of artificial structures using microstrip, and strip line topologies. Using numerical results, the effect of anisotropy on the accuracy of the extracted parameters are investigated, and a fitting solution is proposed, and verified to address this challenge. New structures based on 2nd , and 3rd order fractal Hilbert curves are fabricated, and characterized using microstrip line, and strip line fixtures. Experimental results are presented, and compared with numerical results. The new experimental methods have advantages of lower cost, easier to fabricate and measure, and smaller sample size when compared to the existing methods in the literature.

A new application is proposed for use of magnetic materials to develop wide band artificial magnetic conductors (AMC). Analytical models, and numerical analysis is used to validate the concept. A new ultra wideband AMC is designd, and analysed. The designed AMC is used as the ground plane to develop a low profile high gain ultra wide band antenna. The designed antenna is simulated, and its return loss, and gain is presented over a wide range of frequencies.

A comprehensive study is presented on the performance of AMMs for the application of miniaturized antennas. A miniaturized antenna, using fractal Hilbert metamaterials as substrate, is fabricated, and measured. Measurement results are presented, and compared with numerical results. A parametric study is presented on the effect of the constitutive parameters of the artificial substrate on the performance of the miniaturized antenna. In this study, the effect of magnetic loss of AMM on the gain, and efficiency of the antenna, as well as the effect of dispersion of AMM on the bandwidth of the antenna is investigated.

Acknowledgements

I would like to take this opportunity to express my deepest gratitude to my supervisor Prof. Omar M. Ramahi. During the course of this study, he supported me in every aspect. He never hesitated, when I needed his time. I never forget the day when I gave him a conference paper for review, just the day before the deadline, and he was sick, but he revised it for me. Thanks to him for his kindness, understanding and support during these four years.

I'm thankful to the committee members, Prof. Engheta, Prof. Khamesee, Prof. Safavi-Naeini , and Prof. Mansour, for spending their valuable time to review my thesis and give valuable comments. I'm specially grateful to Prof. Engheta for accepting to come to Canada for attending my defense exam.

I also would like to acknowledge my dear family. First of all, my dear mother, who was the first one who encouraged me to explore new things. She was the first teacher and role model in my life. My dear father comes next. Thanks to him for his endless support, sacrifice, and patience. Growing up having his home library around, and watching his great interest in reading surely influenced me to develop my own personal interest in learning new things. I also would like to thank my dear siblings for their warm support, and love.

My warmest thanks to my beloved husband for his great emotional, and technical support. Having him is the greatest fortune in my life. I need to appreciate also my little angle, Aryan, for his understanding the fact that mommy is not just his mommy, and she needs to spend some time on research too :)

I'm specially grateful to my mother and father in-laws for their help and support in the recent months when I was writing this thesis. If it wasn't their help in taking care of Aryan, I would not have been able to finish my thesis on time.

During the course of this study, I enjoyed being a member of an active and friendly research group. Thanks to all my friends for their technical help, and friendship.

Special thanks to Dr. Bakr, and Dr. Bandler with whom I had fruitful discussions for the optimization part of this work.

This work was financially supported by Research in Motion (RIM) and the National Science and Engineering Research Council of Canada (NSERC) under the NSERC/RIM Industrial Research Chair Program and the NSERC Discovery Grant Program.

Dedication

This thesis is dedicated to all brave women and men who are fighting for freedom, and human rights all around the world.

Contents

List of Tables x

List of Figures xvi

1 Introduction 1

- 1.1 Motivation 1
- 1.2 Pervious Works 2
- 1.3 Thesis Work 3
- 1.4 Thesis Organization 4

2 Natural and Artificial Magnetic Materials 6

- 2.1 Introduction 6
- 2.2 Magnetic Dipole Moment and Permeability 7
- 2.3 Natural Magnetic Materials 8
- 2.4 Proposed Application: Low Profile Ultra Wide Band Antennas using EBG Structures with Magneto-Dielectric Materials 11
  - 2.4.1 Artificial Magnetic Ground Planes 11
  - 2.4.2 Using Magneto-Dielectric Materials to Increase the In-Phase Reflection Bandwidth of Artificial Magnetic Grounds 12
  - 2.4.3 Low Profile Spiral Antenna Using the Designed EBG as an AMC Ground Plane 15
- 2.5 Artificial Magnetic Materials 18
  - 2.5.1 Formulating Effective Permeability for a Topology with Arbitrary Shape 19

2.5.2 Simulation Setup for Numerically Characterization of Metamaterials 23
2.5.3 SRR inclusions 26
2.5.4 Spiral Inclusions 28
2.6 Conclusion 30

3 New Inclusions based on Fractal Hilbert Curves 32
3.1 Introduction 32
3.2 Proposed Structures 33
3.3 Analytical Model 34
3.4 Resultant Permeability 39
3.5 Conclusions 41

4 New Experimental Method for Retrieval of Constitutive Parameters of Artificial Structures using a Microstrip Fixture 43
4.1 Introduction 43
4.2 Characterization Method 44
4.3 Measurement Results 48
4.4 Conclusion 53

5 A New Retrieval Method for Characterization of Metamaterials Using a Strip Line Fixture 54
5.1 Introduction 54
5.2 Retrieval Method 55
5.3 Full Wave Numerical Analysis 58
5.3.1 Results for Isotropic Samples 58
5.3.2 Results for Anisotropic Metamaterial and Fitting Solution . 60
5.4 Measurement Results 63
5.5 Conclusion 71

6 Miniaturized Antennas using Artificial Magnetic Materials 75

6.1 Introduction . . . 75

6.2 Miniaturized Enhanced Bandwidth Antennas . . . 76

6.3 Numerical Analysis . . . 78

6.4 Measurement Results . . . 79

6.5 Parametric Study . . . 81

6.5.1 Lossy Substrate . . . 82

6.5.2 Dispersive Substrate . . . 83

6.6 Conclusion . . . 85

7 Artificial Magnetic Materials with Multi-Resonator Unit Cells 88

7.1 Introduction . . . 88

7.2 Unit Cells with Multiple Inclusions . . . 88

7.3 Developing Analytical Formulas for Multi-Resonator Configurations 90

7.4 Optimized Multi-Resonator Configurations . . . 92

7.4.1 Analytically Optimized Unit Cell with 4 Fractal Inclusions . 93

7.4.2 Analytically Optimized Unit Cell with 4 SRR Inclusions . . 94

7.5 Full Wave Optimization using Implicit Space Mapping . . . 96

7.5.1 Problem Definition . . . 98

7.5.2 Optimization Results . . . 100

7.6 Conclusion . . . 101

8 Concluding Remarks 104

8.1 Summary and Thesis Contribution . . . 104

8.2 Future Work . . . 107

References 108

List of Tables

2.1 Simulation results for EBGs with different permeability. 15

3.1 The ratio of the parameter of Hilbert inclusion to that of spiral . . 38

5.1 Comparison of the accuracy of the different measurement methods. 74

7.1 Optimal value for optimization variables. 95
7.2 Optimal value for optimization variables for the design of Fig. 7.8. 97
7.3 Table of optimization variables in each iteration. 100
7.4 Table of preassigned parameters in each iteration. 100

List of Figures

2.1 Magnetic dipole moment of a closed circuit. 8

2.2 Permeability (solid line) and magnetic loss tangent (dot line) of Cobalt Hexaferrite printed from [1]. 10

2.3 Schematic showing the mushroom EBG structure. 12

2.4 Incident plane wave simulation setup where a periodic boundary condition (PBC) is placed around the cell to model an infinite EBG surface. 14

2.5 The phase of the reflected plane wave for the EBG structure with $\mu_r = 6.0$ and for the conventional EBG introduced in [2]. 15

2.6 Schematic of the low profile spiral antenna above the EBG surface. 17

2.7 Return loss of the spiral antenna on different ground planes. 18

2.8 Gain of the spiral antenna at 9GHz when placed in free space, over a PEC surface, and over the designed EBG surface. 19

2.9 Gain of the spiral antenna at 14GHz when placed in free space, over a PEC surface, and over the designed EBG surface. 20

2.10 Gain of the spiral antenna at 18GHz when placed in free space, over a PEC surface, and over the designed EBG surface. 21

2.11 An engineered magnetic substrate composed of metallic inclusions. . 21

2.12 Some of the particles used as unit cell of artificial magnetic substrates a)SRR b)Metasolenoid c) Spiral d) Square LC resonator. 22

2.13 A unit cell of engineered magnetic substrate composed of particles with arbitrary shape. 22

2.14 Simulation setup used for numerically characterization of metamaterials. 24

2.15 Transmission line equivalent for Fig. 2.14 setup. 25

2.16 the numerically extracted permeability for the metasolenoid magnetic material proposed in [3]. 26

2.17 A unit cell of the engineered magnetic substrate composed of split ring resonators (SRR). 27

2.18 Calculated Permeability for the SRR inclusion shown in Fig. 2.17 is compared with simulation results. 29

2.19 A unit cell of the engineered magnetic substrate composed of spiral rings. 29

2.20 Calculated Permeability for the spiral inclusion shown in Fig. 2.19 is compared with simulation results. 30

3.1 (a)SRR. (b) Square spiral. (c) Second-order fractal Hilbert inclusion. (d) Third-order fractal Hilbert inclusion. (e) Fourth-order fractal Hilbert inclusion. Note that as the order of Hilbert curve increases, the size of inclusion decreases 35

3.2 A unit cell of engineered magnetic substrate composed of inclusions with 3rd order Hilbert Curve. 36

3.3 Real part of resultant permeability for engineered materials with inclusions shown in Fig. 3.1. Analytical results (solid line) are compared with numerical results (dash line). 39

3.4 Imaginary part of resultant permeability for engineered materials with inclusions shown in Fig. 3.1. Analytical results (solid line) are compared with numerical results (dash line). 40

3.5 Imaginary part of the resultant permeability at frequencies below the resonance. The frequency is normalized to the resonance frequency. 41

4.1 The setup configuration used for extraction of the permeability of the artificial media 47

4.2 Characterization Process 48

4.3 Fractal Hilbert2 inclusion used for constructing artificial magnetic material. $l_1 = l_3 = l_4 = l_5 = l_6 = l_7 = 3.03mm, l_2 = 6.06mm, \Delta y = 3.028mm, \Delta x = \Delta z = 11mm$ 50

4.4 A single strip containing 6 unit cells of inclusions fabricated using printed circuit board technology. 50

4.5 The fabricated fixture used for permeability measurement 51

4.6 Measured Input Impedance 51

4.7 The measured and numerically simulated real part of the permeability for the artificial magnetic material shown in Fig. 4.5. 52

4.8 The measured and numerically simulated imaginary part of the permeability for the artificial magnetic material shown in Fig. 4.5. . . . 53

5.1 The setup configuration for the strip line fixture used for extraction of the permittivity and permeability of the artificial media 56

5.2 The transmission line model of the setup configuration in Fig. 5.1 57

5.3 The constitutive parameters of the sample under test (Frequency-dependent case) 59

5.4 Extracted permittivity for the data shown in Fig. 5.3. 60

5.5 Extracted permeability for the data shown in Fig. 5.3. 61

5.6 Results of simulation for anisotropic sample. Extracted permittivity is plotted versus actual value of permittivity. 62

5.7 Results of simulation for anisotropic sample. Extracted permeability is plotted versus actual value of permeability. 64

5.8 Results of simulation for anisotropic sample. Real part of extracted permeability before and after fitting is plotted and compared with the actual data. 65

5.9 Results of simulation for anisotropic sample. Imaginary part of extracted permeability before and after fitting is plotted and compared with the actual data. 65

5.10 Results of simulation for anisotropic sample. Real part of extracted permittivity before and after fitting is plotted and compared with the actual data. 66

5.11 Results of simulation for anisotropic sample. Imaginary part of extracted permittivity before and after fitting is plotted and compared with the actual data. 66

5.12 Fractal Hilbert3 inclusion used for constructing artificial magnetic material. $l_x = 8mm, \Delta y = 1.5mm, \Delta x = \Delta z = 11mm$ 67

5.13 A single strip containing 2 unit cells of inclusions fabricated using printed circuit board technology. 67

5.14 The fabricated strip line fixtures. a) without artificial sample. This fixture is measured to be used as a reference b) with artificial sample in between. 68

5.15 Magnitude of the measured S parameters of the reference fixture (see Fig. 5.14 (a)) 69

5.16 Phase of the measured S21 of the reference fixture (see Fig. 5.14 (a)) 70

5.17 Magnitude of the measured S parameters of the fixture with artificial sample in between(see Fig. 5.14 (b)) 71

5.18 Phase of the measured S parameters of the fixture with artificial sample in between(see Fig. 5.14 (b)) 72

5.19 The Extracted constitutive parameters from measured S parameters. No fitting is done in this figure. 72

5.20 The Extracted measured permeability after fitting, using (5.12), is compared with numerical simulation results. 73

5.21 The Extracted measured permittivity after fitting, using (5.13), is compared with numerical simulation results. 73

6.1 The structure of the probe-fed patch antenna. 77

6.2 The return loss of the miniaturized antenna using magneto-dielectric material ($\epsilon_r = \mu_r = 7$) is compared with the case of using dielectric with high permittivity ($\epsilon_r = 49$). 78

6.3 Coaxial probe feed Patch Antenna radiating over an engineered substrate. 79

6.4 The alternative choice for structure of Fig. 6.3, which is used for simulation. The engineered material is modeled as a homogenous substrate with effective parameters 79

6.5 The fabricated miniaturized antenna, a=3.3 cm , b=4.2 cm , X0 =1.7 cm , Y0 =1.4 cm. 80

6.6 The measured return loss of the miniaturized antenna. 81

6.7 The measured Pattern of the miniaturized antenna is compared with simulation results. 82

6.8 The Gain of the miniaturized antenna versus magnetic loss tangent (numerical results). 83

6.9 The Efficiency of the miniaturized antenna versus magnetic loss tangent (numerical results). 84

6.10 The simulation results of an antenna with dispersive substrate is compared with the case of using dispersion-free substrate. 85

6.11 Real part of permeability with different dispersion. The dispersion varies as the slope of the line varies. 86

6.12 The return loss of the miniaturized antenna on substrates with permeability shown in Fig. 6.11. 86

7.1 A unit cell with two inclusions. 89

7.2 Real part of resultant permeability of configuration of Fig. 7.1 is compared with that of each resonator when the other one dose not exist. 90

7.3 Imaginary part of resultant permeability of configuration of Fig. 7.1 is compared with that of each resonator when the other one dose not exist. 91

7.4 Circuit model for a unit cell with four resonators. 92

7.5 Numerical, and analytical results for the structure of Fig. 7.1. . . . 93

7.6 A unit cell with 4, 3rd order fractal Hilbert inclusions. 94

7.7 Resultant permeability of the optimized inclusion containing 4 inclusions with 3rd order fractal Hilbert configuration. 95

7.8 Circuit model for a unit cell with four resonators. 96

7.9 Permeability of the optimized inclusion containing 4 SRR. The analytical result is compared with numerical result. 97

7.10 A unit cell of the structure used for implicit space mapping optimization. 99

7.11 The optimization results at the iteration 1. 101

7.12 The optimization results at the iteration 2. 102

7.13 The optimization results at the iteration 3. 102
7.14 The optimization results at the iteration 6. 103

Chapter 1

Introduction

1.1 Motivation

Metamaterials have attracted enormous interest among electromagnetic research groups as they provide electromagnetic properties which do not exist in natural materials [4]–[7].

Artificial magnetic materials are a branch of metamaterials which are designed to provide desirable magnetic properties which do not exist in natural materials. These artificial structures are designed to provide either negative or enhanced positive (higher than one) relative permeability.

Materials with negative permeability do not exist in nature. Artificial magnetic materials with negative permeability can be used alone, to construct single negative (SNG) metamaterials, or they can be used along with artificial structures providing negative permittivity, to construct double negative metamaterials (DNG). In recent years, researchers have proposed many interesting applications for both SNG, and DNG metamaterials. These applications include but not restricted to: sub-wavelength cavity resonators and parallel-plate wave guides [8]–[10], sub-wavelength cylindrical and spherical coreshell systems [11], resonant enhancements of source-generated fields [5], efficient electrically small dipole antennas [12], sensitivity enhancement near-field probes using double and single negative media [13]–[15], and mutual coupling reduction between antennas [16]–[18].

For low-loss applications in the microwave region, natural material choice is limited to nonmagnetic dielectrics. When requiring relatively high positive permeability, the choices are limited to ferrite composites which provide high levels of magnetic loss [19]–[22]. Therefore, artificial magnetic materials are designed to provide desirable enhanced positive value for permeability at microwave frequencies [23]–[31]. Recently it has been shown that utilizing magneto-dielectric materials instead of dielectrics with high permittivity offers many advantages in an important class of applications [32]–[37]. These applications include but not restricted to: enhanced bandwidth efficient miniaturized antennas [32]–[34], low profile enhanced gain antennas using artificial magnetic superstrates [35], enhancement of bandgap in the woodpile EBG structures [33], and enhancement of in-phase reflection bandwidth of EBGs when they are used as artificial magnetic ground planes [36], [28].

1.2 Pervious Works

The idea of using the split-ring as an artificial magnetic particle was introduced first in [38]. The works on realizing such a media started in the late 1990's [23]–[25]. Since then, engineers have proposed numerous types of inclusions [3]–[31]. The single and coupled split ring resonators (SRR), modified ring resonators, paired ping resonators, metasolenoid [3], spiral configuration [1], [30] are some of the most popular configurations used in previous works. Each proposed structure provides its own advantages and disadvantages in terms of resultant permeability and dissipation. For example, in [3] it was shown that the metasolenoid configuration provides higher permeability in comparison to SRR configurations, or using spiral configuration results in artificial magnetic materials with smaller unit cells when compared to SRR and metasolenoid [1], [30].

In terms of modeling, and analysis, a number of analytical models have been developed to explicate the physics behind the peculiar characteristics of artificial magnetic materials (AMMs) [24]–[25], [39]–[41]. When the periodicity and the size of the inclusions are small compared to the wavelength, electromagnetic mixing formulas such as the effective medium theory (EMT) and homogenization theories (HT) can be used to derive the effective permeability and permittivity for composite media [41]. Using the EMT technique, Pendry in [24] calculated the effective permeability of a medium containing looped metallic inclusions such as metal cylinders, Swiss Rolls, and SRRs, and showed that the negative permeability can be obtained in microwave frequencies. Effective medium theory allows identifying the average field propagating inside a composite medium with respect to the field propagating inside a homogeneous medium with an effective electrical characteristic of the medium [40]. The circuit-based models of metamaterials, especially artificial magnetic materials, are developed to capture either the behavior of the entire composite medium or the behavior of the separate inclusions [3]. Mostly the circuit models are proposed to describe the magnetic behavior of the inclusions rather than the electric behavior. In circuit-based models, the model depends on the geometry of the inclusions and the dimension of its different sections.

In terms of experimental characterization, So far several experimental methods have been reported for retrieval of parameters of artificial structures such as the resonator method [42],[43], the free space method [44]–[46], and the waveguide method [47]-[48]. Each of these methods has its own advantages and disadvantages. For example, The resonator method provides high accuracy but it is inherently narrow band, and an individual measurement setup should be prepared for retrieval of the constitutive parameter at each single frequency, or free space approach, and the waveguide method need expensive setups [44]–[48].

1.3 Thesis Work

In this thesis, several advances are added to the existing knowledge of developing artificial magnetic materials, in terms of analytical modeling, applications, realization, and experimental characterization.

New inclusions based on fractal Curves are proposed for realization of artificial magnetic materials. The new inclusions have advantages of miniaturization, and less dispersion when compared to the existing structures in the literature.

The concept of multi-resonator unit cells for realization of multi-band artificial magnetic materials is proposed. The new unit cells can be designed to give the desired magnetic properties either over multiple distinguished frequency bands, or over a single wide frequency band.

Two new methods are proposed for experimental characterization of artificial structures using microstrip, and strip line topologies. The proposed structures have advantages of lower cost, easier to fabricate and measurement, and smaller sample size when compared to the existing methods in the literature.

A new application is proposed for use of magnetic materials to enhance the bandwidth of artificial magnetic ground planes. The developed new magnetic conductor can be used to develop low profile high gain ultra wide band antennas.

For the application of miniaturized antennas, a parametric study is done on the effect of the constitutive parameters of the artificial substrate on the performance of miniaturized antenna such as gain, bandwidth, and efficiency.

1.4 Thesis Organization

Thesis contains 8 chapters including the introduction chapter.

In chapter 2, natural, and artificial magnetic materials, and their applications are discussed. The discussion includes, the limitations of natural magnetic materials, operation principle of artificial magnetic materials, circuit models, and numerical simulation methods for design and analysis of artificial structures. Furthermore, SRR, and spiral inclusions as two examples of artificial magnetic inclusions are studied in detail. In addition, a new application for magnetic materials is proposed. In the new application, materials with permeability higher than one are used as the substrate of mushroom-type EBGs, resulting in wider in-phase reflection bandwidth. The performance of the designed EBG as the ground plane to implement low-profile wide band antennas is presented through full wave numerical analysis.

In chapter 3 , new inclusions based on fractal Hilbert curves are introduced for realization of artificial magnetic materials with smaller unit cells. Analytical formulas for design and analysis of the proposed structures are presented, and full-wave numerical characterization is performed to verify the analytical results. Furthermore, using the analytical model and numerical simulation results, the proposed inclusions are compared to spiral inclusions.

Chapter 4 proposes a new experimental method for characterization of artificial magnetic materials using microstrip topology. The retrieval method is introduced and explained in detail. The proposed method is used to measure the constitutive parameters of artificial magnetic materials with 2nd order fractal Hilbert inclusions that were introduced in chapter 3. Measurement results are presented and comparison is made with the numerical simulation results.

Chapter 5 proposes a new experimental method for characterization of artificial magnetic materials using a strip line topology. The retrieval method is explained in detail, and using numerical full wave analysis, the accuracy of the method has been verified for various type of metamaterials. Then the method has been used for experimental characterization of artificial magnetic materials with unit cells of 3rd order fractal Hilbert configuration. Measurement results of the Hilbert inclusions are presented, and compared with numerical simulation results.

In chapter 6, the performance of artificial magnetic materials for the application of miniaturized antennas is investigated. Full wave analysis as well as measurement results are used to study miniaturized antennas with artificial magnetic materials as substrate. A comprehensive parametric study is performed on the effect of specifications of the artificial substrate such as loss, and dispersion over gain, efficiency, and bandwidth of the miniaturized antenna.

In chapter 7, the concept of multi-resonator unit cells for realization of multi-band artificial structures is introduced, and investigated using both analytical models, and full wave numerical simulation. The concept is applied to unit cells with different inclusions such as fractal Hilbert, circular SRRs, and square SRRs. Circuit models for different configurations of multi-resonator structures are proposed and optimized to give a wide band response for permeability. Implicit space mapping technique is used to make a mapping between analytically optimized structures, and the designs used for full wave numerical analysis.

Finally Chapter 8 presents concluding remarks, and summery of the thesis. Contributions of the thesis, possible future directions for this research, as well as publication work of the thesis are presented in chapter 8.

Chapter 2

Natural and Artificial Magnetic Materials

2.1 Introduction

In this chapter natural and artificial magnetic materials are introduced, and discussed. In this discussion, the principle operation of magnetic materials, their applications, and the methods to model, simulate, and realize them are presented.

The organization of this chapter is as follows: First, in section 2.2, the definition of magnetic dipole moment is presented. Then in section 2.3 the mechanism of operation for natural magnetic materials is discussed, and the limitation of these natural materials in microwave frequencies is investigated. Section 2.4 introduces a new application for magntic materials, in which magnetic materials are used to develop ultra wide-band artificial magnetic ground planes. In section 2.4, it is shown that using materials with permeability higher than one, as the substrate of mushroom-type EBGs, results in wider in-phase reflection bandwidth. The idea is then verified using incident plane wave analysis for EBG designs with different values of permeability. Then the performance of the designed EBG used as the ground plane to implement low-profile wideband antennas is presented through numerical full wave analysis. Section 2.5, introduces artificial magnetic materials, and presents analytical models for analysis of these materials. In section 2.5.1, a general circuit model is presented for artificial magnetic particles. The model is general and can be used for design and optimization of artificial magnetic particles with arbitrary shape. To be able to characterize the artificial structures numerically, in section 2.5.2 a simulation setup is discussed based on reflection, and transmission from a slab of metamaterials. In sections 2.5.3, 2.5.4, SRR, and spiral inclusions as two examples of artificial magnetic inclusions are studied. Analytical formulas are presented for analysis, and design of artificial materials with SRR, and spiral inclusions, and a comparison is made between analytical, and numerical results. Finally, a summery and conclusion is presented in section 7.6.

2.2 Magnetic Dipole Moment and Permeability

According to Lorentz Law, a charge particle in motion in a magnetic field of flux density B, experiences a force as:

$$\overline{F} = q\overline{V}X\overline{B} \tag{2.1}$$

where q and are the charge and velocity of the particle, respectively. Since a current by definition is the moving charges, the force applied to a closed circuit carrying current I, can be obtained from integrating the force applied to small current filaments:

$$\overline{F} = I\oint(\overline{dl}X\overline{B}) \tag{2.2}$$

Using above equations and definition of the torque, the electromagnetic torque applied to a small closed circuit carrying current I, will be equal to :

$$\overline{T} = I\overline{S}X\overline{B} \tag{2.3}$$

where S is the surface enclosed by the small loop. Using above equation, differential magnetic dipole moment is defined for a small circulating current as:

$$\overline{m} = I\overline{S} \tag{2.4}$$

Fig. 2.1 shows the geometry leading to the definition given in 2.4. In a bulk material, orbital and spin motions of the electrons provide magnetic dipole moments for each individual atom. The magnetic polarization vector, M is defined as the average of the individual magnetic dipole moments of the atoms, m_i:

$$\overline{M} = lim_{\Delta v\rightarrow 0}\frac{1}{\Delta v}\sum_{i=1}^{n}\overline{m_i} \tag{2.5}$$

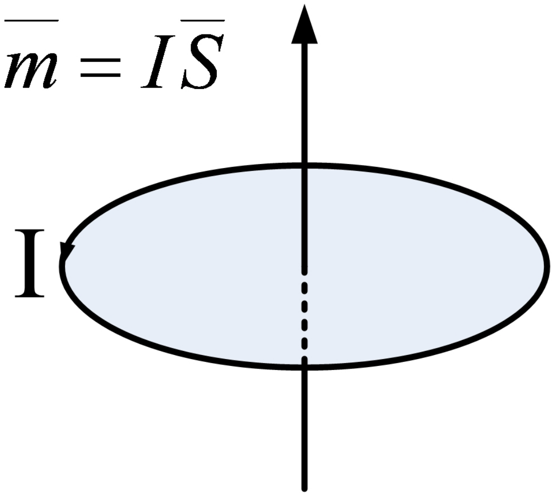

Figure 2.1: Magnetic dipole moment of a closed circuit.

In the absence of an external magnetic field, in most of the materials the individual magnetic moments of electrons cancel each other and the net magnetic polarization will be zero. When an external magnetic field exists, the torque applied to the magnetic dipoles turns the loops such that their magnetic moments align parallel or anti-parallel to the external magnetic field leading to a net value for magnetic polarization vector. How easily a material experiences magnetization is quantified by its magnetic susceptibility χ_m:

$$\chi_m = \frac{M}{H_{ext}} \tag{2.6}$$

The permeability of a material which is a quantitative description of how the material experience magnetization, is defined as the ratio of total magnetic flux and the applied magnetic field in the material :

$$\mu = \frac{B}{H} = \frac{\mu_0(H_{ext} + M)}{H_{ext}} = \mu_0(1 + \chi_m) \tag{2.7}$$

2.3 Natural Magnetic Materials

Although a thorough understanding of microscopic magnetic phenomena that occurs in natural magnetic materials need knowledge of quantum theory, using the simple atomic model can lead to meaningful qualitative results. In the simple atomic model, it is assumed that there is a positive nucleus surrounded by electrons in circular orbits. In this model, each electron has two motions, one rotating around the nucleus in the orbit and another spinning around its axes. These motions are the source of two kinds of magnetic moments. The third contribution to the magnetic moment of an atom is caused by movement of protons in the atomic nucleus and is named nuclear spin. Due to the much greater nuclear mass, the magnitude of nuclear magnetic moment is much smaller and negligible compared to electron magnetic moment. In each individual atom, when there is no external magnetic field, the orbital magnetic moments of electron pairs cancel each other. This cancelation occurs also for paired spin moments. Therefore for an atom with completely filled electron shells, there is total cancelation of moments. When there is an applied magnetic field, it tries to align the magnetic moment of atoms with the field direction. According to their response to the external magnetic field, materials can be classified into four major groups: diamagnetic, paramagnetic, ferromagnetic, and ferrimagnetic materials [22].

Diamagnetism is a very weak form of magnetism which occurs when orbital moments of atoms align in the opposite direction to that of applied field [22]. For these materials χ_m is a very small negative number leading to permeability less but very close to one. Silver with $\mu_r = 0.99998$ and lead with $\mu_r = 0.999983$ are two examples of materials with this property.

Paramagnetism occurs when atomic magnetic dipoles are free to rotate and align with the applied external field [22]. In paramagnetism the net susceptibility χ_m is very small but positive resulting in permeability higher but very close to one. For example, aluminum with $\mu_r = 1.00002$, and Palladium with $\mu_r = 1.0008$, are two paramagnetic materials.

Ferromagnetism is exhibited in some metallic materials such as iron, cobalt, and nickel. In these materials, magnetic moments due to the uncanceled electron spins of adjacent atoms interact to align with each other and produce susceptibility as high as [22]. However, the use of these materials as magneto-dielectrics is limited due to their high conductivity which results in high loss.

Ferrimagnetism is a kind of magnetism which occurs in some kind of ceramics due to their complex crystal structure. In these materials, there are parallel and antiparallel coupling interactions between the ions, and the net magnetic moment arises from incomplete cancelation of spin magnetic moments [22]. In these materials the permeability and conductivity are highly dependent to temperature and processing, thus desirable magnetic properties can be obtained by a proper process.

Almost all natural magnetic materials do not exhibit proper magnetic properties in the microwave frequencies. The challenge to microwave applications arises from the inertia of atomic system. Although the mass of electron is small, it is not zero and the attempts of the electron magnetic dipole moments to track the external field deteriorate and finally fail as the frequency increases and approaches the microwave region. Thus, for magnetic materials, the upper frequency of operation is limited by the gyromagnetic resonances occurring in the VHF-UHF range. As an example, Fig. 2.2 shows the relative permeability and magnetic loss tangent of Cobalt Hexaferrite, a magnetic material recently developed by Trans-Tech company. As shown in this figure, the maximum useful frequency for this material is below 500MHz. Since natural magnetization dose not occur in microwave frequencies, engineered magnetic materials are designed to provide desirable magnetic properties in these frequencies. The idea of developing artificial magnetic materials is to design a mechanism similar to what happens in natural magnetic materials for microwave operation. In these materials, metallic inclusions are inserted inside the substrate in which the induced current provides magnetic dipole moments. In the following sections, we will present this idea and discuss the mechanism of operation of artificial magnetic materials.

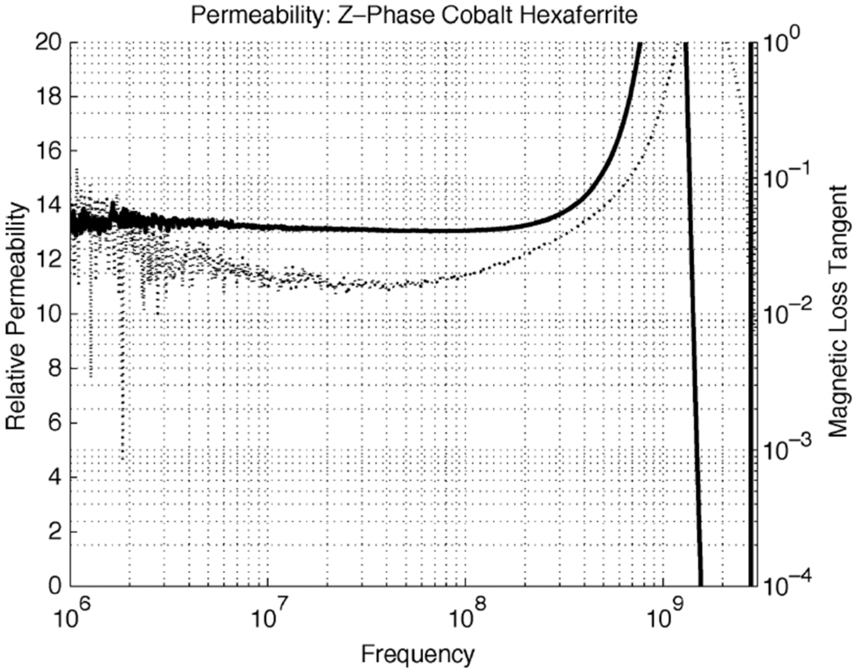

Figure 2.2: Permeability (solid line) and magnetic loss tangent (dot line) of Cobalt Hexaferrite printed from [1].

2.4 Proposed Application: Low Profile Ultra Wide Band Antennas using EBG Structures with Magneto-Dielectric Materials

In this section, a novel application for magneto-dielectric materials is introduced. Materials with permeability higher than one are used to increase the in-phase reflection bandwidth of the mushroom-type EBGs, and the designed EBG structure is used to implement a low-profile wideband antenna.

2.4.1 Artificial Magnetic Ground Planes

When an antenna is radiating near a surface, there is an interaction between the waves radiated by the antenna and the waves reflected from the surface. If the reflected waves are in phase with the incident waves, this interaction will be constructive, otherwise; it will be destructive. This interaction can be described by invoking the concept of surface impedance for the reflector plane. The surface impedance is defined as the ratio of the tangential component of the electric field to the tangential component of the magnetic field at the surface. Using the transmission line model for the normal incidence of plane waves, the reflection coefficient for the electric field is defined as

$$\Gamma = \frac{Z_s - Z_0}{Z_s + Z_0} \tag{2.8}$$

where Z_s is the surface impedance of the reflector and Z_0 is the wave impedance in the air. For example Z_s of a perfect electric conductor (PEC) surface is zero leading to $\Gamma = -1$ or out of phase reflection. On the other hand, Z_s of a perfect magnetic conductor (PMC) surface is infinite leading to $\Gamma = +1$ or in-phase reflection.

Although PMC dose not exist in nature, EBG structures act as high impedance surfaces in their in-phase reflection bandwidth thus emulating a PMC surface [49],[50]. Most EBG structures, however, have desirable properties over a narrow frequency range where the resonance occurs thus limiting their application in the design of low profile ultra wideband antennas. For example, in [51],[52], EBG structures were used as the ground plane to implement low profile spiral antennas, but in these works the frequency independent behavior of the spiral antenna was limited by the relatively narrow in-phase reflection bandwidth of the EBG surface.

In the next section, we propose a new method to increase the in-phase reflection bandwidth of EBGs.

2.4.2 Using Magneto-Dielectric Materials to Increase the In-Phase Reflection Bandwidth of Artificial Magnetic Grounds

The mushroom structure, first introduced in [53] and shown in Fig. 2.3, emulates a high impedance surface (HIS) in its in-phase reflection bandwidth.

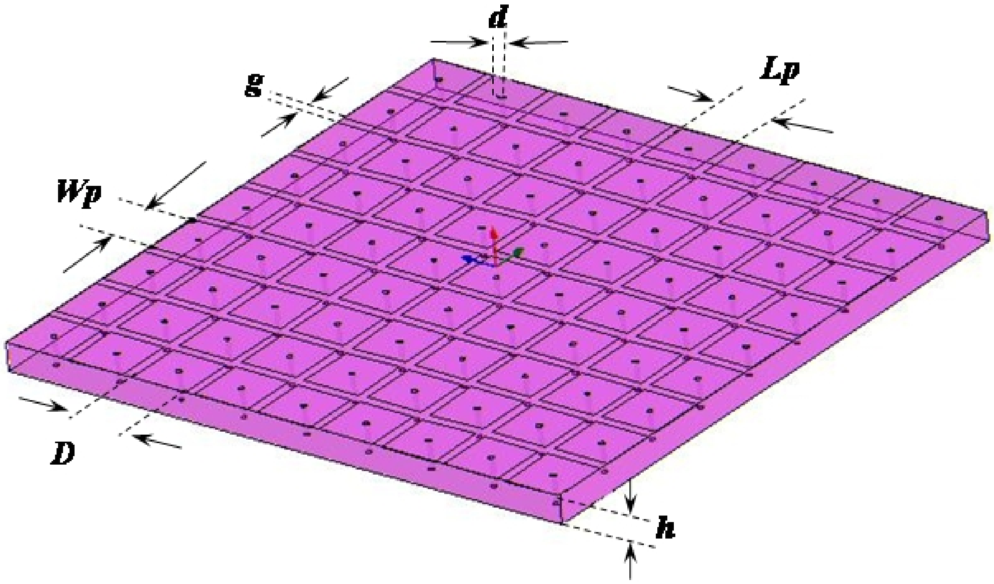

Figure 2.3: Schematic showing the mushroom EBG structure.

For normal incidence, the surface impedance of a mushroom EBG can be modeled as an inductor in parallel with a capacitor. The capacitance part is due to the gap (physical separation) between the patches and is equal to [54]:

$$C = \frac{D\epsilon_0(\epsilon_r + 1)}{\pi} \ln(\frac{2D}{\pi g}) \tag{2.9}$$

where ϵ_r is the relative permittivity of the dielectric, D is the grid period and g is the gap between the patches (see Fig. 2.3). The inductance part is due to the metal backed substrate and can be calculated using transmission lines theory. A metal backed slab of thickness h can be modeled as a shorted transmission line leading to a surface impedance of:

$$Z_s = j\eta \tan(\beta h) \tag{2.10}$$

where η and β are the wave impedance and phase constant in the slab, respectively. When $h << \lambda$, the above impedance becomes inductive and can be approximated as $Zs = j\omega L$, where L is given by

$$L = \mu_0 \mu_r h \tag{2.11}$$

It was demonstrated in [55] that the LC circuit model leads to significant error only in the case when the grid period D is very large compared to the substrate height h.

The usable bandwidth of an EBG, when operating as an artificial magnetic conductor (AMC), has been considered to be the frequencies over which the phase of the reflection coefficient is bounded by ±45 degrees [56], and is usually given as the percentage bandwidth with respect to the center frequency. It is well known from filter theory, that this in-phase reflection bandwidth for a parallel LC circuit is proportional to $\sqrt{\frac{L}{C}}$, while the resonance frequency is proportional to $\frac{1}{\sqrt{LC}}$. Here, we use magneto-dielectric materials where the relative permeability, μ_r is greater than one to increase L and thus to increase the in-phase reflection bandwidth. The increase in L, for a specific resonance frequency, has the added advantage of reducing the size of the patch as smaller capacitance would be needed to achieve the same resonant frequency. Therefore, the in-phase reflection bandwidth increases more due to the reduced C.

To verify the idea, a mushroom EBG with substrate of permeability higher than one is designed and compared with a conventional EBG. To see the effect of permeability, new structures with the following dimensions $W_p = L_p = 0.5mm, g = 0.15mm, D = L_p + g = W_p + g = 0.65mm, h = 1.57mm, d = 0.1mm, \epsilon_r = 2.51$ and with different values of permeability (μ_r) varying from $\mu_r = 1-9$ are considered. In recent works [23]–[25], magnetic loss tang of about 0.01 is achieved for engineered magnetic materials. In this work $tan\delta m = 0.01$ is assumed to model the loss in the designs with permeability higher than one. The structures are simulated with Ansoft HFSS using plane wave excitation with normal incidence. The simulation setup is the same as used in [49] and is shown in Fig. 2.4. The simulation results for different value of permeability are summarized in Table 2.1. This table illustrates the reflection-phase bandwidth (the range of frequencies in which reflection phase is bounded by ±45 degrees) as well as center frequency in which the reflected phase is zero. As shown in this table, reflection-phase bandwidth increases as permeability increases.

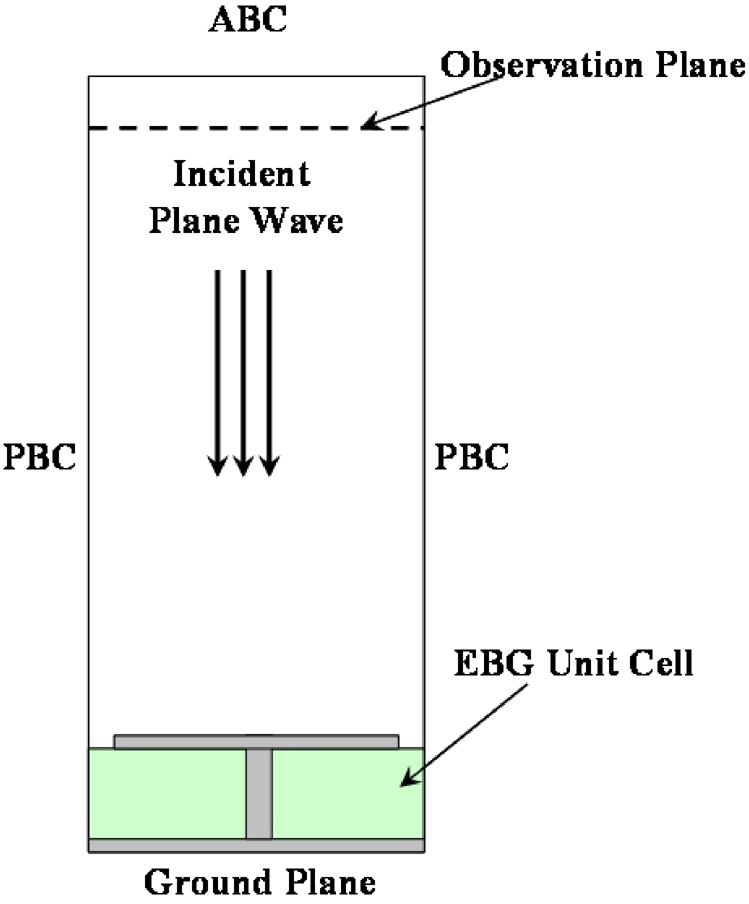

Figure 2.4: Incident plane wave simulation setup where a periodic boundary condition (PBC) is placed around the cell to model an infinite EBG surface.

To compare with the conventional case ($\mu_r = 1$), Fig. 2.5 shows the results of the simulation where the reflection wave phase is presented as a function of frequency for EBG structure with $\mu_r = 6$ as well as the results for a conventional EBG ($\mu_r = 1$). For the conventional EBG, we used the structure introduced, simulated and experimentally tested in [2] with the following dimensions: $W_p = L_p = 2.44mm, g = 0.15mm, D = 2.59mm, h = 1.57mm, d = 0.25mm, \mu_r = 1, and \epsilon_r = 2.51$. The results presented in this figure show that the EBG with $\mu_r = 6$ has an in-phase bandwidth of 70%, while the in-phase bandwidth for the EBG with $\mu_r = 1$ is only 18%.

Table 2.1: Simulation results for EBGs with different permeability.

μ_r	In phase reflection bandwidth (GHz)	Center frequency (GHz)	Percentile bandwidth (%)
1	22-30	25.9	30.9
3	11.3-19	15	51.3
6	7.1-14.6	10.65	70.4
9	5.4-12.7	8.7	83.9

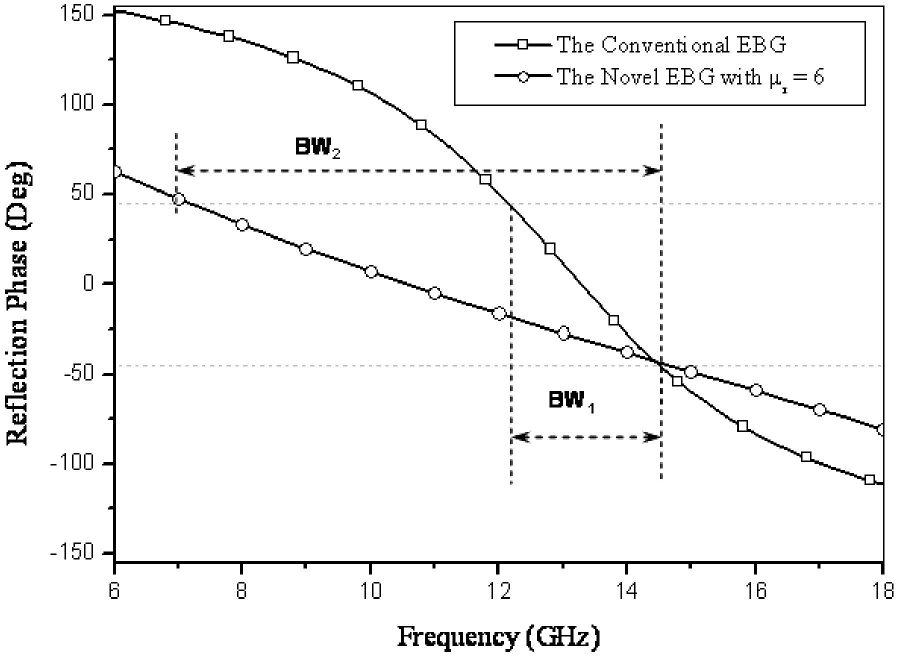

Figure 2.5: The phase of the reflected plane wave for the EBG structure with $\mu_r = 6.0$ and for the conventional EBG introduced in [2].

2.4.3 Low Profile Spiral Antenna Using the Designed EBG as an AMC Ground Plane

The idea of using an EBG structure as a ground plane to mimic the behavior of a PMC surface was first introduced in [53]. In theory, by placing an impressed current source a distance d above a PMC ground plane, a perfect image of the current source is induced at a distance d below the ground plane. If d is very small compared to the wavelength, then the source and its image almost coincide thus doubling the radiated field intensity. Now if an antenna is placed above an EBG surface, then one would hope that over the range of frequencies in the in-phase reflection bandwidth of the EBG (where the EBG acts as a PMC), the radiated field intensity would double in comparison to the case when the antenna is in free space.

Earlier works, especially the ground breaking work in [53], showed that the EBG does indeed mimic a PMC surface and the radiation increases. However, because the EBG structure is within the near field of the antenna, one would expect that the resonant frequency of the antenna to be shifted due to the interaction between the antenna and the EBG.

Guided by image theory, the previous findings in [53] and the EBG designed in pervious section using magneto-dielectric material, we designed a printed square spiral antenna to radiate effectively over the frequency range of 8 to 18GHz. Square spirals are easier to model and fabricate and as shown in [57], they approximate the most well known Archimedean spiral antennas. To have coincidence with the in-phase reflection bandwidth of the EBG structure and the radiation band of the antenna, the EBG design with $\mu_r = 6$ in the last section is selected. The structure and dimensions of the spiral over the EBG surface are illustrated and provided in Fig. 2.6. The strip width of the spiral and the gap between the arms are set to 0.4 mm. The side length of the spiral is 11.6 mm which is equivalent to one third of the wavelength at the lowest frequency of 8GHz. The finite EBG surface (14mm x 14mm) covered an area approximately equal to the footprint of the antenna.

The spiral antenna over the finite EBG surface is simulated using Ansoft HFSS and the results are illustrated in Figs. 2.7- 2.10. Fig. 2.7 shows the return loss of the low profile spiral antenna when placed at a distance of only 0.2mm, ($\frac{\lambda}{105}$ at the center frequency f_c of 14GHz), above the proposed EBG ground plane. For comparison and for a perspective on the low profile antenna, we show in this figure the return loss for the same antenna when placed 0.2mm ($\frac{\lambda}{105}$ at f_c) above a PEC ground plane, and when placed at the same distance above the conventional EBG ($\mu_r = 1$). As shown in Fig. 2.7, the designed low profile antenna has a bandwidth ($S_{11} < -10dB$) of 9-19GHz, while the antenna over conventional EBG has a bandwidth of only 13-16GHz. The achieved bandwidth for the designed low profile antenna is even wider than the in-phase reflection bandwidth of the EBG. The 1 GHz upward shift in the bandwidth of the antenna is attributed to the near field interaction between the antenna and the EBG. A similar shift was observed for the dipole antenna in [49],[50].

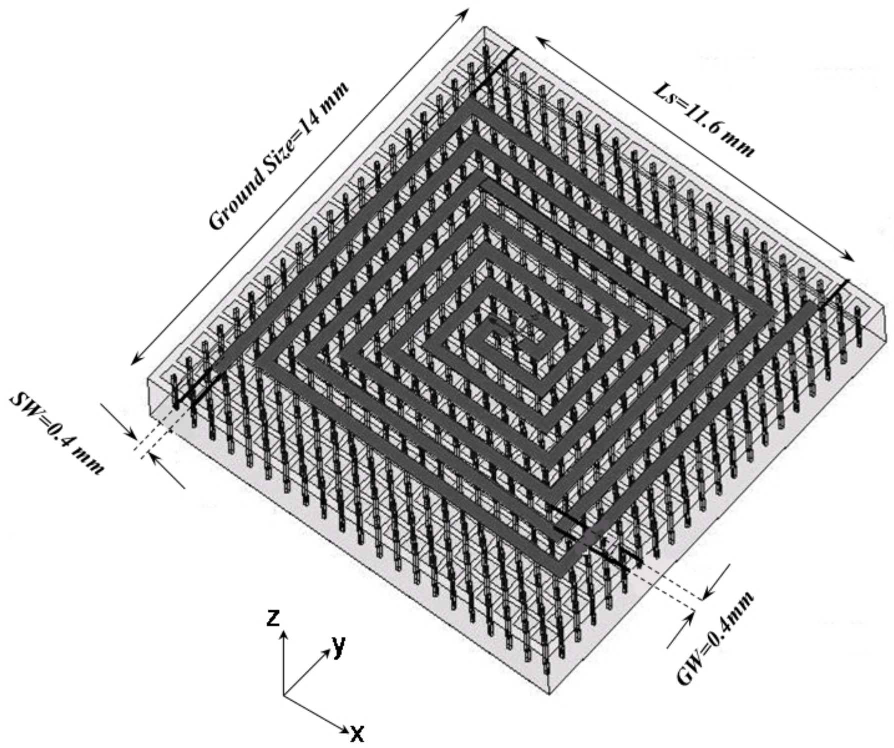

Figure 2.6: Schematic of the low profile spiral antenna above the EBG surface.

The gain of the proposed antenna in the x-z plane is shown in Figs. 2.8- 2.10 for different frequencies. The new design is compared to the same spiral antenna when placed 5.4 mm ($\frac{\lambda}{4}$ at f_c) above a PEC ground plane with the same size of the EBG ground plane (14mm x 14mm) and when suspended in free space. The comparison presented in Figs. 2.8- 2.10 shows that the gain of the low profile antenna, at the center frequency of 14GHz is about 6.2dB that is 1.6dB higher than the spiral in free space, and it has a front to back ratio of 16dB. Furthermore, the low profile antenna shows a very better front to back ratio rather than antenna over the PEC at low frequencies (see Figs. 2.8). However, when compared to the antenna backed by a PEC at $\frac{\lambda}{4}$, we observe a 2dB decrease in the gain. This can be attributed to the magnetic loss of the material.

Therefore, the simulation results of VSWR and gain of the designed low profile antenna shows that the antenna radiates efficiently over the designed EBG ground plane.

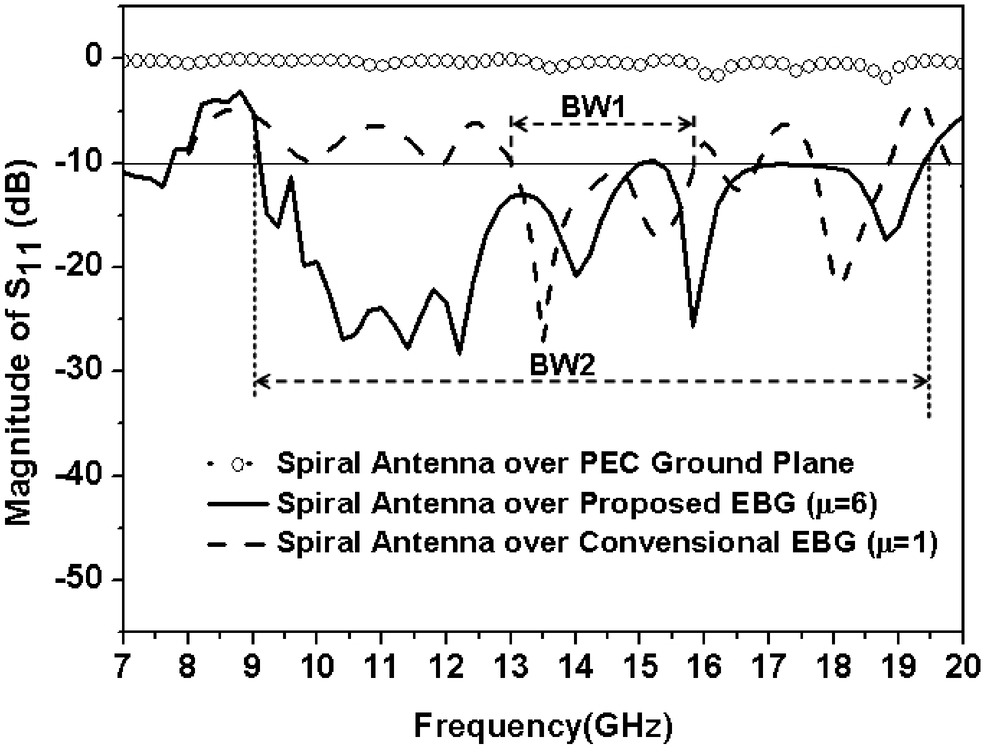

Figure 2.7: Return loss of the spiral antenna on different ground planes.

2.5 Artificial Magnetic Materials

As discussed in pervious section, natural magnetization does not occur in materials in the microwave regime. Therefore designing engineered substrates with permeability higher than that of free space has become increasingly attractive [23]–[25]. Generally an engineered magnetic media is composed of small resonating particles which provide effective permeability around their resonance frequency. Fig. 2.11 shows an engineered magnetic media composed of spiral rings as proposed in [1]. As shown in Fig. 2.11, resonating particles are stacked in the x and y directions to provide a homogenous magnetic media. Many shapes have been proposed for artificial magnetic particles [23]–[25]. Fig. 2.12 shows some of these topologies. In spite of their different structures, the mechanism of operation for all is the same. When the resonating cells are submerged in a media where an external magnetic field H_{ext} exists, according to Faraday's Law, the change in the magnetic flux enclosed by these rings induces an Electromotive Force (emf) in the rings. The emf voltage supplies a current in the ring which in turn produces magnetic dipole moment. This magnetic dipole moment is the source of the effective permeability. In the next

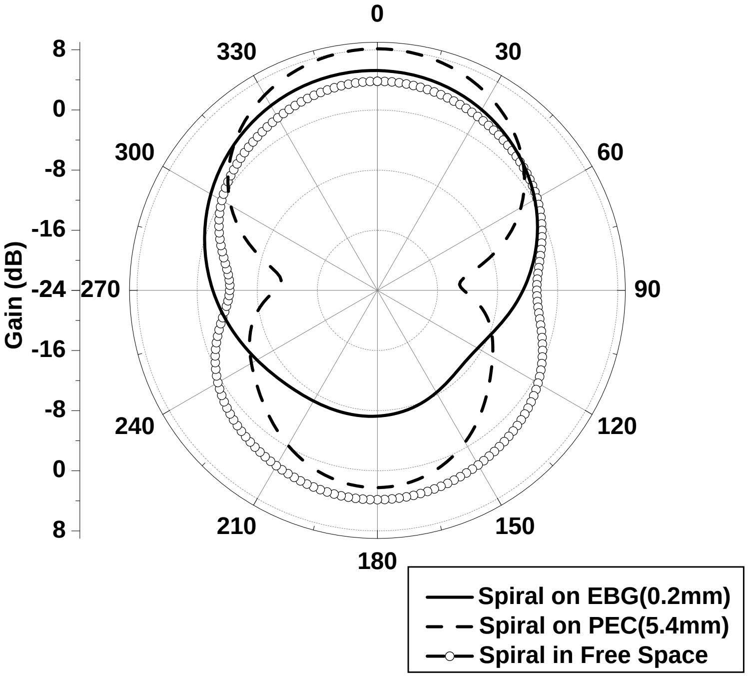

Figure 2.8: Gain of the spiral antenna at 9GHz when placed in free space, over a PEC surface, and over the designed EBG surface.

section, this magnetic moment for a ring with an arbitrary shape is formulated and an equivalent circuit model is presented to model the resultant permeability.

2.5.1 Formulating Effective Permeability for a Topology with Arbitrary Shape

Fig. 2.13 shows an artificial magnetic particle with arbitrary shape. A unit cell of this material with dimension Δx, Δy, and Δz is illustrated in this figure. Assuming an external magnetic field H_{ext} applied in the Y direction, it induces an Electromotive Force (emf) in the rings. This emf induces the current I in the ring. Now H field is the sum of two fields, external magnetic field H_{ext} and induced magnetic field H_{ind}. Assuming N as the number of turns of wires that carry the induced current I (N for inclusion in Fig. 2.13 is equal to 2), induced magnetic field can be obtained as:

$$H_{ind} = \frac{NI}{\Delta y} \tag{2.12}$$

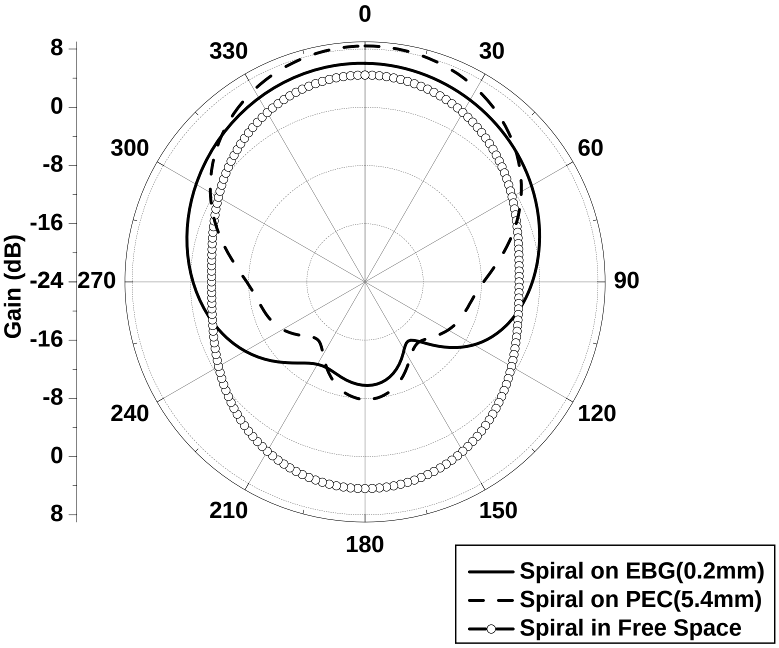

Figure 2.9: Gain of the spiral antenna at 14GHz when placed in free space, over a PEC surface, and over the designed EBG surface.

where Δy is the dimension of the unit cell in the y direction (see Fig. 2.13). In this equation, it is assumed that dimensions of unit cell is much smaller than the wavelength, as it is true for all the designs that will be discussed in this work, so there is a uniform magnetic field in whole the unit cell. Applying Faraday's law, and using (2.12), one can obtain the induced emf as:

$$\begin{aligned} emf &= -j\omega\phi = -j\omega\mu_0 S(H_{ext} + H_{ind}) \\ &= -j\omega\mu_0 S(H_{ext} + N\frac{I}{\Delta y}) \end{aligned} \tag{2.13}$$

where ω is the frequency of the external field, and S is the area enclosed by the inclusion. The generated emf is related to the impedance of the rings and the induced current as

$$emf = Z_{inc} I \tag{2.14}$$

where Z_{inc} is the impedance of the metallic inclusion. Equating (2.13) and (2.14) yields

$$-j\omega\mu_0 S H_{ext} = (Z_{inc} + j\omega\frac{NS\mu_0}{\Delta y})I \tag{2.15}$$

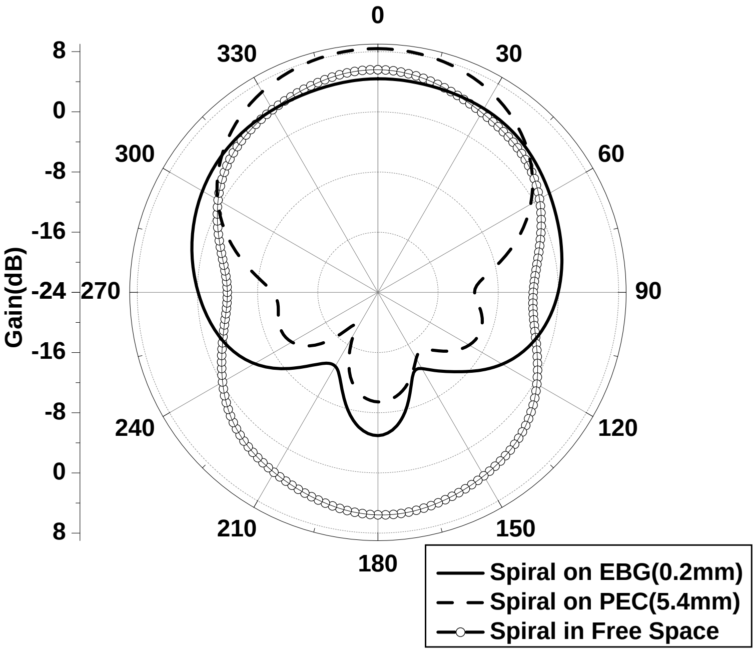

Figure 2.10: Gain of the spiral antenna at 18GHz when placed in free space, over a PEC surface, and over the designed EBG surface.

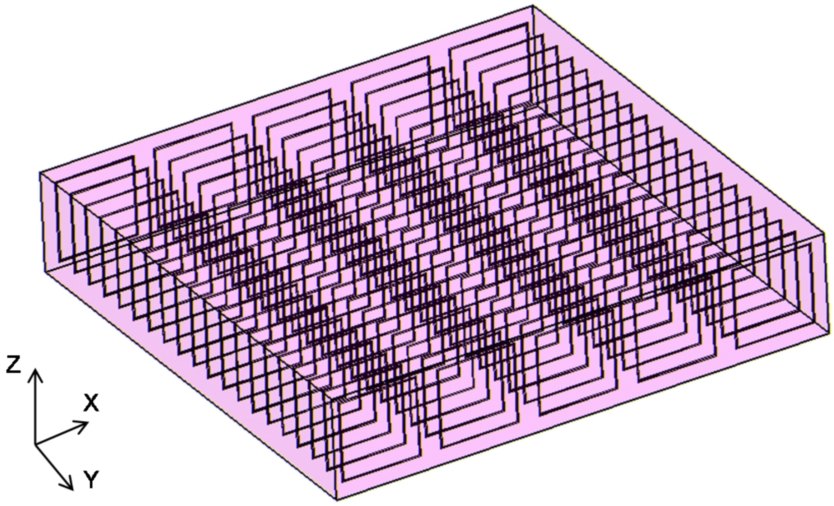

Figure 2.11: An engineered magnetic substrate composed of metallic inclusions.

From (2.15), it is observed that the effective inductance, L_{eff} of the inclusions can

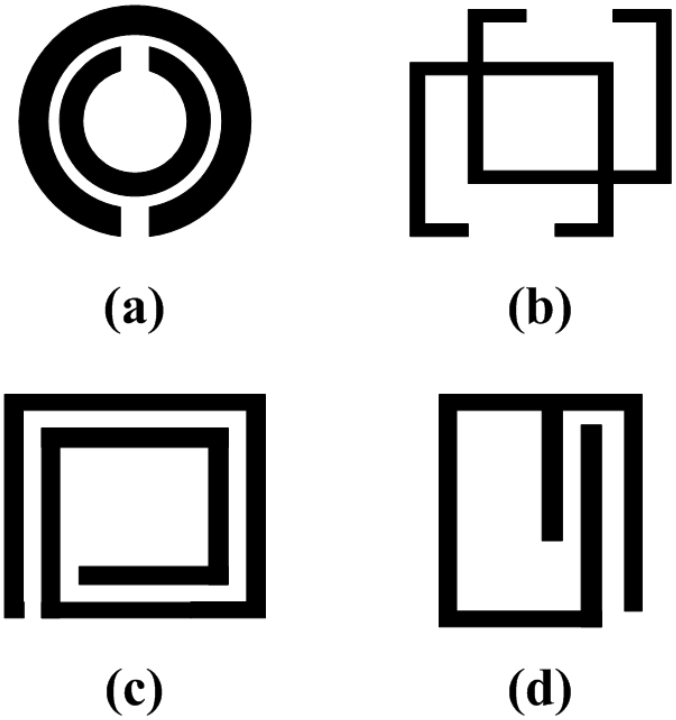

Figure 2.12: Some of the particles used as unit cell of artificial magnetic substrates a)SRR b)Metasolenoid c) Spiral d) Square LC resonator.

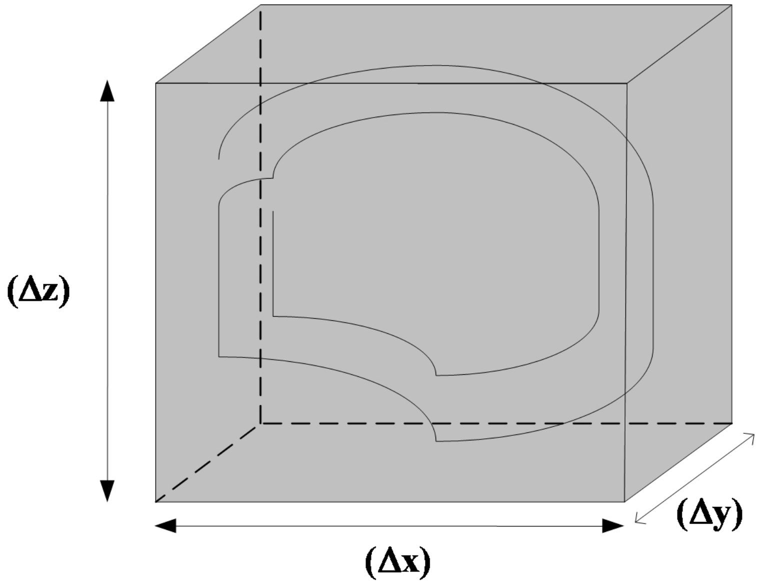

Figure 2.13: A unit cell of engineered magnetic substrate composed of particles with arbitrary shape.

be defined as

$$L_{eff} = \frac{NS\mu_0}{\Delta y} \tag{2.16}$$

The Magnetic polarization, M defined as the average of the induced magnetic dipole moments can be expressed as

$$M = lim_{\Delta v \to 0} \frac{1}{\Delta v} \sum_{i=1}^{n} m_i = \frac{NSI}{\Delta x \Delta y \Delta z} \tag{2.17}$$

Using (2.15) and (2.17), the relative permeability μ_r is obtained as

$$\mu_r = 1 + K \frac{j\omega L_{eff}}{Z_{inc} + j\omega L_{eff}}, K = -\frac{S}{\Delta x \Delta z} \tag{2.18}$$

This formula is general and once one calculates the components of the circuit model of an inclusion, the effective permeability can be obtained from this formula.

It should be noted that the substrate whose unit cell is shown in Fig. 2.13 can provide magnetic moment vectors only in the direction perpendicular to the inclusion surface (i.e. the effective permeability formulated in (2.18) represents the yy component of the permeability tensor). For x-directed and z-directed magnetic fields, the effective permeability will be equal to that of the host media which is unity for nonmagnetic substrates. Therefore, the artificial substrate will be anisotropic with permeability tensor of

$$\mu = \mu_0 \begin{pmatrix} 1 & 0 & 0 \\ 0 & \mu_r & 0 \\ 0 & 0 & 1 \end{pmatrix} \tag{2.19}$$

To achieve isotropic artificial substrates with the same effective permeability in all the three directions of x, y, and z, two inclusions with the surfaces perpendicular to the x, and z directions should be added to the unit cell shown in Fig. 2.13. If these two inclusions have the same structure as the inclusion perpendicular to the y direction, the same effective permeability formulated in (2.18) will be achieved in the x, and z directions.

2.5.2 Simulation Setup for Numerically Characterization of Metamaterials

In this section a simulation setup is presented to perform numerical full-wave analysis for characterization of metamaterials. For the numerical analysis, the commercial software based on the finite element method, Ansoft HFSS is used. The simulation setup is shown in Fig. 2.14. To model an infinite slab, the Periodic

Boundary Conditions (PMC) is used in the x and y directions around a unit cell of the meta-material. Plane wave analysis is used to extract the effective permeability. A plane wave is incident normally on the slab and the average value of the reflection and transmission coefficients, Γ and T, are evaluated over surfaces A1 and A2 respectively (see Fig. 2.14). Then the effective parameters, μ_{eff} and ϵ_{eff}, are extracted from reflection and transmission coefficient using transmission line theory [58]–[59]. The equivalent transmission line model of Fig. 2.14 is shown in Fig. 2.15. In this figure, the metamaterial unit cell is substituted with a transmission line with characteristic impedance, $Z_{eff} = \sqrt{\frac{\mu_{eff}}{\epsilon_{eff}}}$ and refractive index, $n_{eff} = \sqrt{\mu_{eff}\epsilon_{eff}}$, where effective values are assumed for permeability and permittivity.

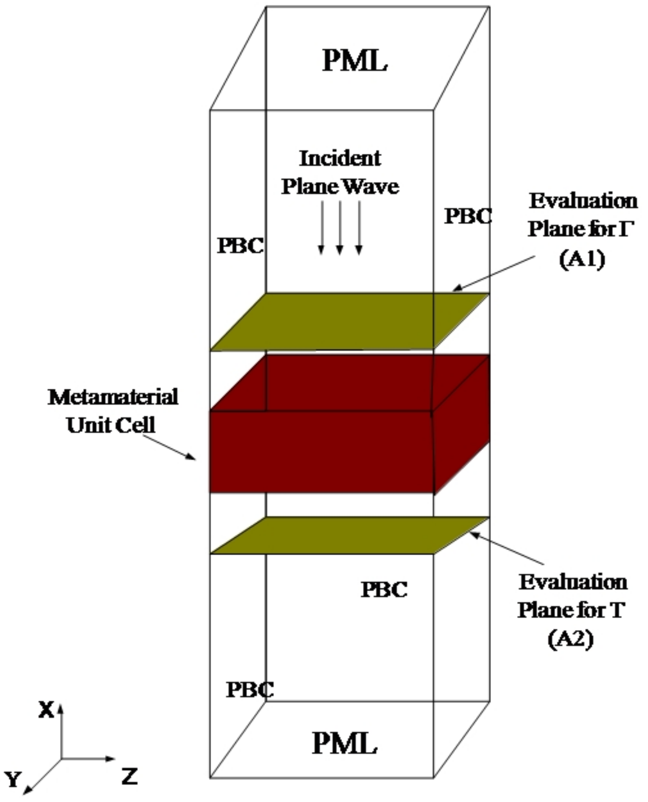

Figure 2.14: Simulation setup used for numerically characterization of metamaterials.

Using transmission line theory, the voltage and current in all three regions are formulated in (2.20)-(2.22).

$$Region I : V_I = e^{-jk_0 z} + \Gamma e^{+jk_0 z}, I_I = \frac{1}{Z_0}(e^{-jk_0 z} - \Gamma e^{+jk_0 z}), \quad (2.20)$$

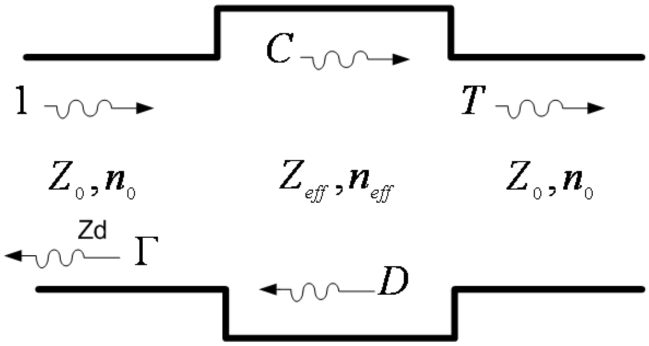

Figure 2.15: Transmission line equivalent for Fig. 2.14 setup.

$$RegionII : V_{II} = Ce^{-jk_0 n_{eff} z} + De^{+jk_0 n_{eff} z}, I_{II} = \frac{1}{Z_{eff}}(Ce^{-jk_0 n_{eff} z} - De^{+jk_0 n_{eff} z}), \tag{2.21}$$

$$RegionIII : V_{III} = Te^{-jk_0(z-d)}, I_{III} = \frac{T}{Z_0}e^{-jk_0(z-d)} \tag{2.22}$$

In (2.20)-(2.22), we have four unknowns that can be obtained by applying boundary conditions at $z = 0$, and $z = d$, for voltage and current:

$$\Gamma = \frac{R_{01}(1 - e^{-2jk_0 n_{eff} d})}{1 - R_{01}^2 e^{-2jk_0 n_{eff} d}}, \quad R_{01} = \frac{Z_{eff} - Z_0}{Z_{eff} + Z_0} \tag{2.23}$$

$$T = e^{+jk_0 d}\frac{(1 - R_{01}^2)e^{-jk_0 n_{eff} d}}{1 - R_{01}^2 e^{-j2k_0 n_{eff} d}} \tag{2.24}$$

Consequently, the effective parameters can be obtained from the transmission and reflection coefficients as:

$$\begin{aligned} Z_{eff} &= \pm Z_0\sqrt{\frac{(1+\Gamma)^2 - T^2 e^{-j2k_0 d}}{(1-\Gamma)^2 - T^2 e^{-j2k_0 d}}} && (2.25)\\ e^{-jn_{eff}k_0 d} &= X \pm j\sqrt{1 - X^2}, && (2.26)\\ X &= \frac{1 - \Gamma^2 + T^2 e^{-j2k_0 d}}{2Te^{-jk_0 d}} && (2.27)\\ \mu_{eff} &= Z_{eff} n_{eff}, \epsilon_{eff} = \frac{n_{eff}}{z_{eff}} && (2.28) \end{aligned}$$

where Z_0 and k_0 are the air characteristic impedance and wave number, respectively; Z_{eff}, n_{eff}, ϵ_{eff}, and μ_{eff} are the effective characteristic impedance, refractive index, permittivity, and permeability of the engineered material, respectively; Γ and T are the reflection and transmission coefficients, and d is the thickness of the engineered material. The sign in (2.25), and (2.26) is determined by the requirements that $Re(Z_{eff}) > 0$ and $Im(n_{eff}) < 0$ for passive media.

To verify the accuracy of the simulation setup, here we compare the results with measurement results reported in [3]. Fig. 2.16 shows the numerically extracted permeability for the metasolenoid magnetic material proposed in [3]. The resonance frequency measured for this material is reported as 1.2GHz in [3]. The 125 MHz difference in the resonance frequency can be due to the air gap between meta cells that is unavoidable in fabrication. Since meta materials are fabricated by stacking small printed meta cells, this air gap is created by thickness of printed metals.

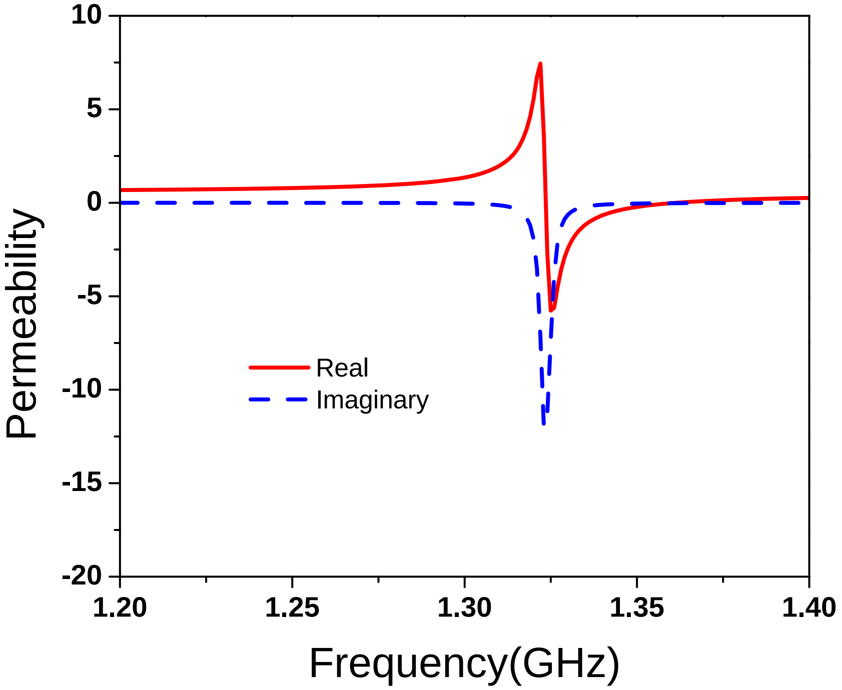

Figure 2.16: the numerically extracted permeability for the metasolenoid magnetic material proposed in [3].

2.5.3 SRR inclusions

Using the formulas achieved in the previous sections, we calculate the effective permeability for a split ring resonator (SRR) inclusion. The unit cell configuration of this artificial substrate is shown in Fig. 2.17.

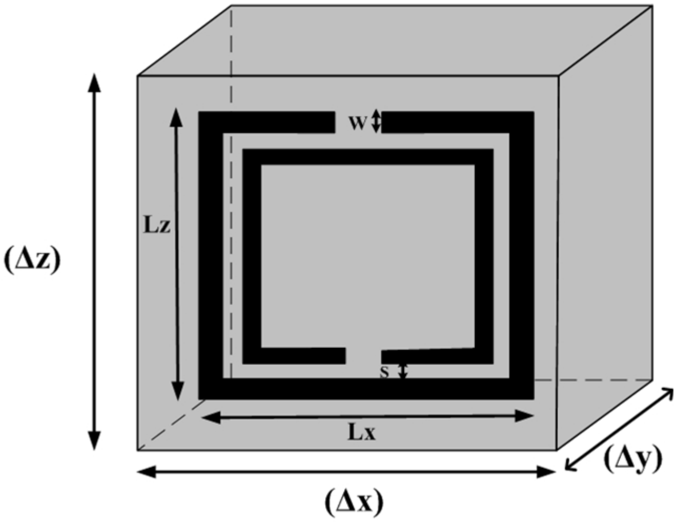

Figure 2.17: A unit cell of the engineered magnetic substrate composed of split ring resonators (SRR).

At this stage, we need to calculate components of the circuit model for this configuration. The effective inductance L_{eff} is calculated from (2.16):

$$L_{eff} = \frac{N\mu_0 S}{\Delta y} = \frac{\mu_0(l_x - W)(l_z - W) + (l_x - 2S - 3W)(l_z - 2S - 3W)}{\Delta y} \tag{2.29}$$

where l_x and l_z are the outer dimensions of the SRR in x and z directions, respectively, W is the width of the metallic strips, and S is the space between strips (see Fig. 2.17). The inclusion impedance, Z_{inc}, consists of two parts: R_{eff}, which models the ohmic loss of the metallic inclusions due to the finite conductivity of the strips, and the other part models the mutual impedance between external and internal loops, Z_{mut}. R_{eff}, can be calculated using the Ohm's law

$$R_{eff} = \frac{l_{total}}{\sigma(W\delta)} = \frac{4(l_x + l_z - 2S - 4W)}{\sigma(W\delta)}, \quad \delta = \sqrt{\frac{2}{\sigma\omega\mu_0}} \tag{2.30}$$

where σ and δ are the conductivity and the skin depth respectively. the mutual impedance between external and internal loops Z_{mut} can be modeled as the per-unit-length mutual impedance of the strips, Z_{pul}, times the average length of the strips, l_{avg}.

$$Z_{mut} = Z_{pul} l_{avg} \tag{2.31}$$

where

$$l_{avg} = (l_x + l_z - 4W - 2S)/2 \tag{2.32}$$

The per-unit-length impedance, Z_{pul} is calculated using conformal mapping technique for the coplanar strip lines [60]–[63]

$$\begin{aligned} Z_{pul} &= \frac{1}{j\omega\epsilon_0\epsilon_r(1-jtan\delta)}\frac{K(g)}{K(\sqrt{1-g^2})}, \\ g &= \frac{S}{S+2W}, \\ K(g) &= \int_0^{\frac{\pi}{2}} \frac{d\phi}{\sqrt{1-g^2\sin^2\phi}} \end{aligned} \tag{2.33}$$

where ϵ_r and $tan\delta$ are the relative permittivity and the loss tangent of the host substrate, respectively. The impedance given in (2.33) contains a parallel combination of a capacitance and a conductance to model the capacitance between the metallic strips and the loss due to the conductivity of the host substrate.

Using the above equations, the relative permeability of the unit cell of Fig. 2.17 is calculated and illustrated in Fig. 2.18. The parameters are used in this calculation are: S=W=0.127mm, Host Dielectric:RO4003(ϵ_r =3.38, $tan\delta$=0.0027), $l_x = l_z = 16mm$, $\Delta y = 3.028mm$, $\Delta x = \Delta z = 20mm$, and strips are assumed to be made of copper. In this figure, analytical results are compared with numerical full wave results. For numerical results, the simulation setup explained in section 2.5.2, and Ansoft HFSS 10 is used. The difference between analytical and simulation results, for the the resonance frequency is 13% ,and for the magnitude at resonance is 31%.

2.5.4 Spiral Inclusions

The unit cell configuration of this artificial substrate is shown in Fig. 2.19. Using circuit models, it was shown in [30] that the effective capacitance of the spiral configuration is four times of that of the SRR. Therefore, spirals can reduce the resonance frequency of the inclusion by a factor of 2, resulting in the miniaturization of the unit cells of artificial structures.

The components of circuit model for this configuration would be the same as the SRR configuration except for the mutual impedance Z_{mut} part which is 4 times of that of SRR:

$$Z_{mut} = 2(l_x + l_z - 4W - 2S)Z_{pul} \tag{2.34}$$

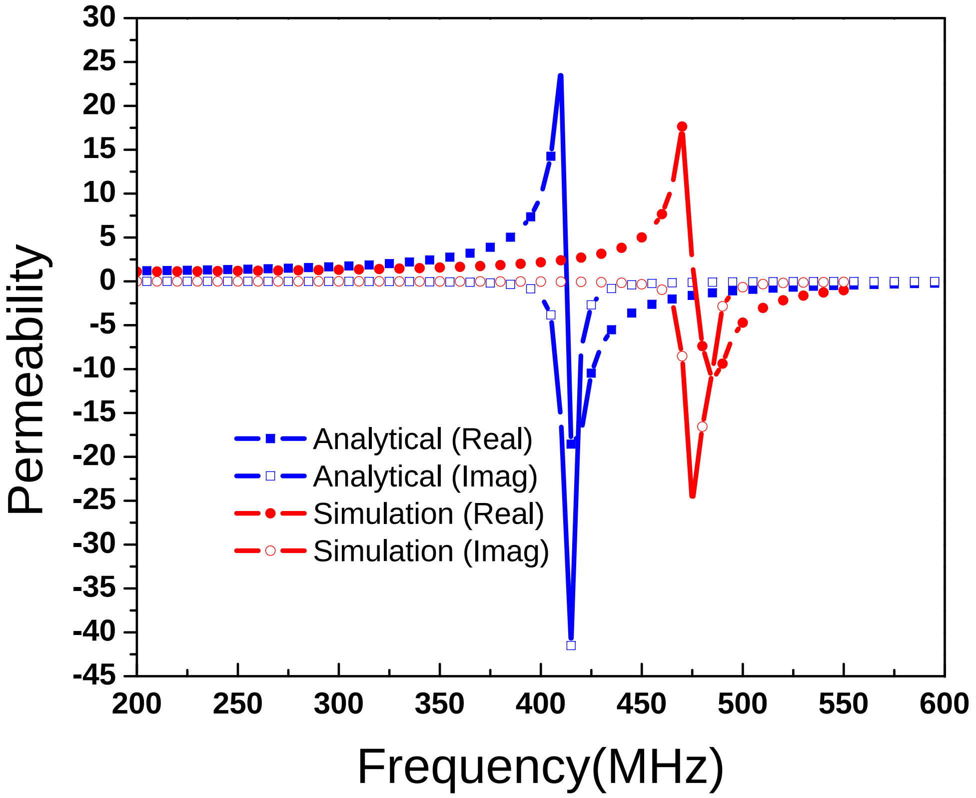

Figure 2.18: Calculated Permeability for the SRR inclusion shown in Fig. 2.17 is compared with simulation results.

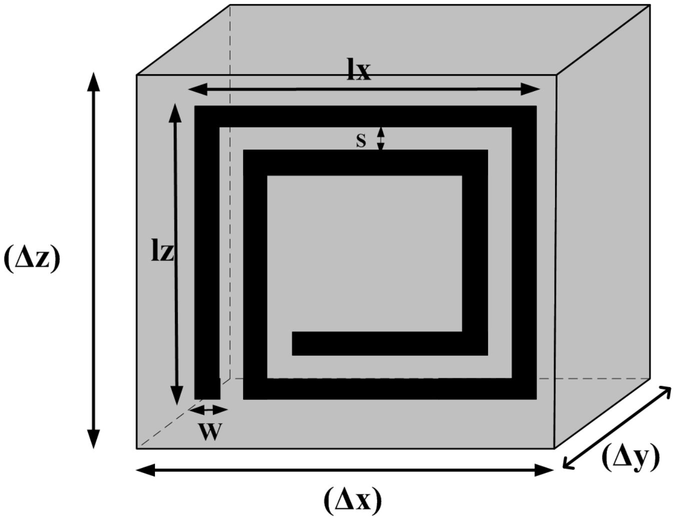

Figure 2.19: A unit cell of the engineered magnetic substrate composed of spiral rings.

where Z_{pul}, was calculated in (2.33). Using the above equations, the relative permeability of the unit cell of Fig. 2.19 is calculated and illustrated in Fig. 2.20. The parameters are used in this calculation is the same as parameters used for SRR in the pervious section. In this figure, analytical results are compared with numerical full wave results. The difference between analytical and simulation results, for the the resonance frequency is 6.4% ,and for the magnitude is 30%.

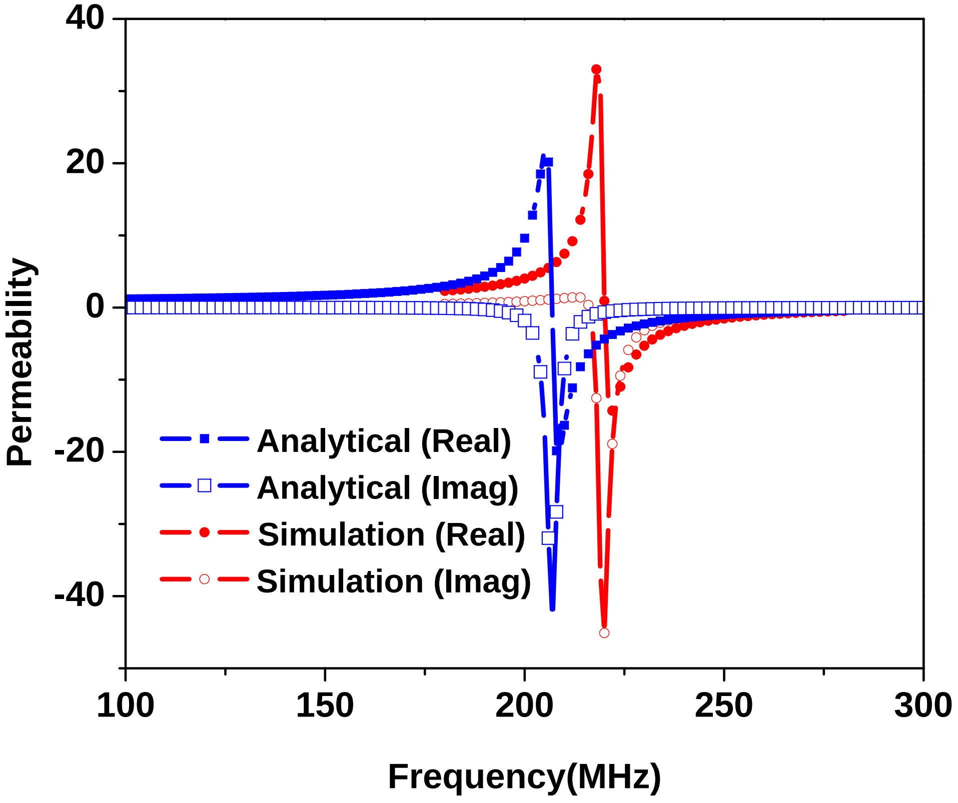

Figure 2.20: Calculated Permeability for the spiral inclusion shown in Fig. 2.19 is compared with simulation results.

2.6 Conclusion

It was shown that magneto-dielectric materials when used as a substrate of mushroom type EBGs can increase the in-phase reflection bandwidth of these structures. Using this fact, a compact wideband EBG structure was proposed and shown to have an in-phase reflection bandwidth of 70% while having a cell size less than 0.25 of a conventional EBG resonating at the same center frequency. To evaluate the efficiency of the designed EBG when working as the ground plane of wideband antennas, a spiral antenna was designed to radiate effectively over the frequency range of 8 to 18 GHz coinciding with the in-phase reflection bandwidth of the EBG structure. A low-profile spiral antenna was implemented by placing the spiral antenna at a distance of 0.2 mm above the proposed EBG. Simulation results show that the low-profile spiral antenna has a 2:1 VSWR over the frequency range of 9 to 19 GHz. The gain of the low-profile antenna at the center frequency of 14 GHz is 6.2 dB with a front to back ratio of 16 dB.

Natural magnetic materials do not operate efficiently at microwave frequencies. Therefore, artificial magnetic materials are developed to provide enhanced positive permeability at microwave frequencies. Operation principle of artificial magnetic materials was discussed and a general analytical model was proposed for calculating the effective permeability of metamaterial with arbitrary topology. To be able to predict the effective parameters of metamaterials with complex topology, an effective simulation tool was presented to numerically extract the effective permeability and permittivity of metamaterials. The simulation results were compared to both the analytical results achieved in this work and measurement results obtained in other works. This comparison showed the ability of the simulation tool for accurate extracting of the effective parameters of metamaterials . SRR, and spiral inclusions, two well known inclusions for realization of artificial magnetic materials, were studied both analytically, and numerically.

Chapter 3

New Inclusions based on Fractal Hilbert Curves

3.1 Introduction

One of the most important applications of artificial magnetic materials is in miniaturized planar structures, specially miniaturized microstrip antennas [1], [31], [64]–[68]. Although it was shown that by using these materials, significant miniaturization factors could be achieved in the planar sizes of the antennas, the height of the substrate is limited by the size of the unit cell of the artificial structures. The size of the developed artificial unit cells are typically much smaller than the wavelength (smaller than $\lambda/20$), yet they yield a large antenna profile (for example, for a microstrip antenna operating at 200 MHz, the smallest profile achieved is 2cm [1]). Furthermore, since the antenna is miniaturized to be much smaller than the wavelength, say $\lambda/20$, therefore, unit cells of the artificial structure should be small enough to provide homogeneity under the miniaturized patch antenna.

With the aim of further miniaturization, other sub-wavelength particles have been recently proposed such as spiral resonators [1], [30], capacitively loaded embedded-circuit particles [69]–[71], as well as lumped-element based metamaterials [72]. In [30], it was shown that using spiral resonators decreases the size of the inclusion by a factor of 2 when compared to SRRs . In [69]–[71], using parallel-plate capacitors, inclusions as small as $\lambda/27$ are developed.(Please note that in this comparison, by λ we mean the wavelength in the host dielectric at the resonance frequency. Since by using a high-k dielectric, for sure the size of inclusion decreases, it is not fair to compare different inclusions based on wavelength in the air)However; the structures in [69]–[71] are three dimensional and cannot be realized using printed circuit technology. Using lumped elements within the inclusions, unit cells as small as $\lambda/52$ were developed in [72]. The solution proposed in [72] is promising, however, lumped elements need to be soldered into place for each unit cell which makes the fabrication process difficult and time-consuming. In [1], using square spirals unit cells as small as $\lambda/46$ were developed and used for antenna miniaturization. The structure introduced in [30], can be realized by simple printed technology.

In this chapter, we introduce fractal curves as inclusions for artificial magnetic material to further increase the miniaturization potential.

Previous works on using fractal geometries in developing artificial structures includes frequency selective surfaces [73], high-impedance surfaces [74], left-handed metamaterials [75], and complementary split ring resonators [76]. An extended class of space-filling wire structures based on grid-graph Hamiltonian paths and cycles has also been investigated in [77].

The organization of this chapter is as follows: First in section 3.2, the new inclusions based on fractal Hilbert curves are introduced and discussed. Then in section, 3.3, analytical formulas are derived for design and analysis of the proposed structures. In section 3.4, using analytical formulas, the resultant permeability of the fractal structures are calculated, and compared with numerical results. Using the analytical model and numerical simulation results, the proposed inclusions are compared to spiral inclusions in terms of electromagnetic properties, and finally summary and conclusion are provided in section 3.5.

3.2 Proposed Structures

Fig. 3.1 shows the proposed structures for metamaterial inclusions based on Hilbert curves, along with the SRR and spiral structures. Using circuit models, it was shown in [30] that the effective capacitance of the spiral configuration is four times bigger than that of the SRR. Therefore, spirals can reduce the resonance frequency of the inclusion by a factor of 2. This claim was verified numerically and experimentally in [30]. The structures proposed here combine the idea of using spiral configuration (proposed in [30]) and fractal Hilbert curve to provide inclusions with smaller size.

The dimensions of the inclusions as a fraction of the wavelength in the dielectric at the resonance frequency are shown in Fig. 3.1. Clearly observed is that when using a fourth-order fractal Hilbert curve makes it possible to realize inclusion as small as 0.014λ. This size is 63% of the size of spiral inclusion and 32% of the size of SRR.

3.3 Analytical Model

Fig. 3.2 shows a unit cell of a third-order Hilbert inclusion.

In what follows, a general formulation, which can be used for any order of Hilbert inclusions, is derived for the effective permeability. The unit cell in Fig. 3.2 has dimensions of Δx, Δy, and Δz in the x, y, and z directions, respectively. Following the method explained in section 2.5.1 of chapter 2, the resultant permeability for fractal curves, μ_r is obtained as

$$\mu_r = 1 + K\frac{j\omega L_{eff}}{Z_{inc} + j\omega L_{eff}}, K = -\frac{S}{\Delta x \Delta z} \tag{3.1}$$

It should be noted that the substrate whose unit cell is shown in Fig. 3.2 can provide magnetic moment vectors only in the direction perpendicular to the inclusion surface (i.e. the effective permeability formulated in (3.1) represents the yy component of the permeability tensor). For x-directed and z-directed magnetic fields, the effective permeability will be equal to that of the host media which is unity for nonmagnetic substrates. Therefore, the artificial substrate will be anisotropic with permeability tensor of

$$\mu = \mu_0 \begin{pmatrix} 1 & 0 & 0 \\ 0 & \mu_r & 0 \\ 0 & 0 & 1 \end{pmatrix} \tag{3.2}$$

To achieve isotropic artificial substrates with the same effective permeability in all the three directions of x, y, and z, two inclusions with the surfaces perpendicular to the x, and z directions should be added to the unit cell shown in Fig. 3.2. If these two inclusions have the same structure as the inclusion perpendicular to the y direction, the same effective permeability formulated in (3.1) will be achieved in the x, and z directions.

The formula given in (3.1) is general and can be used for Hilbert inclusions of any order. The only difference between various orders would be in the value of the inclusion impedance, Z_{inc}, and the effective inductance, L_{eff}.

The effective inductance, L_{eff} given in (2.16) is a function of the area S, enclosed by the inclusion; and since this area varies by the order, n, of fractal

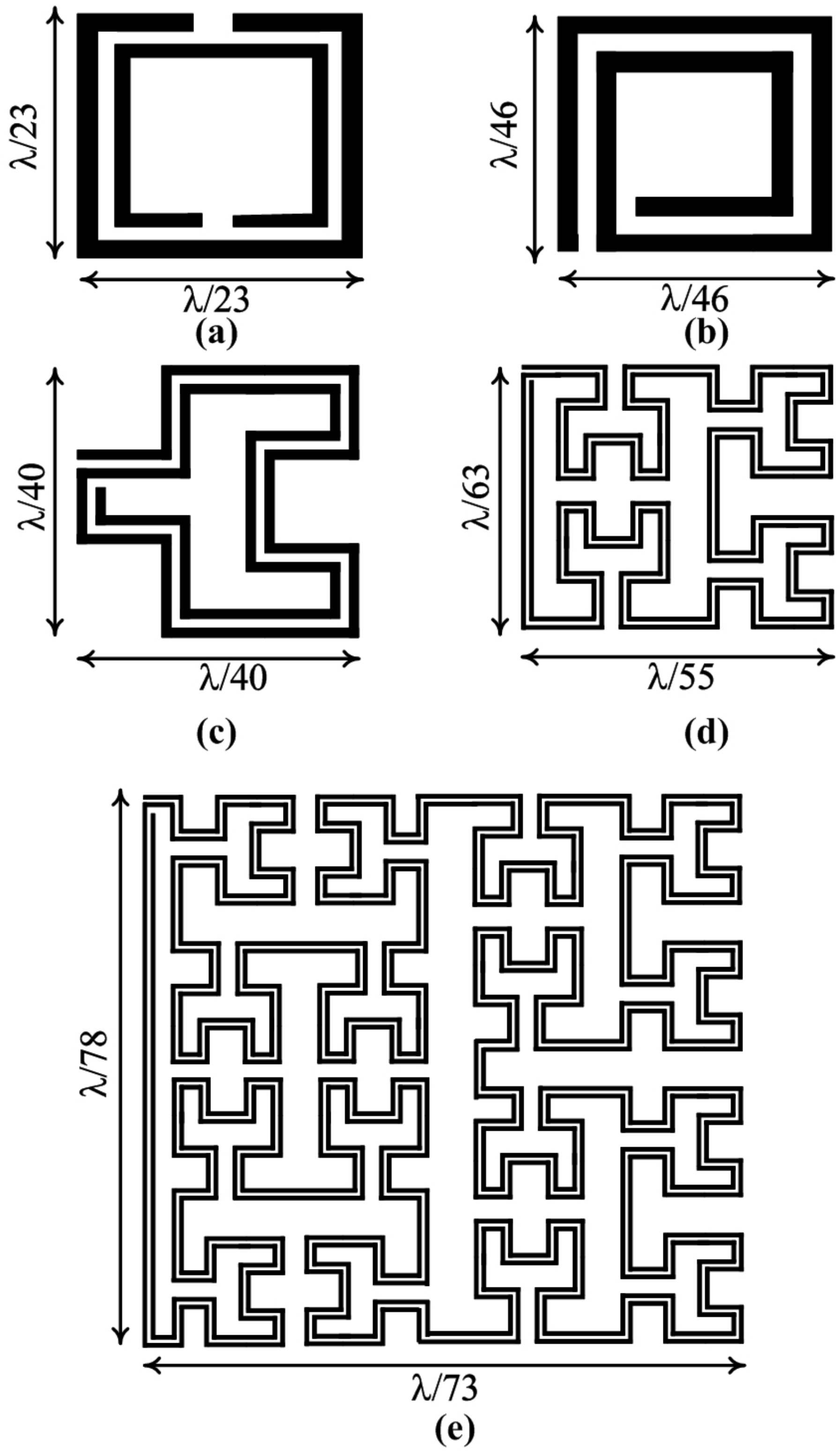

Figure 3.1: (a)SRR. (b) Square spiral. (c) Second-order fractal Hilbert inclusion. (d) Third-order fractal Hilbert inclusion. (e) Fourth-order fractal Hilbert inclusion. Note that as the order of Hilbert curve increases, the size of inclusion decreases

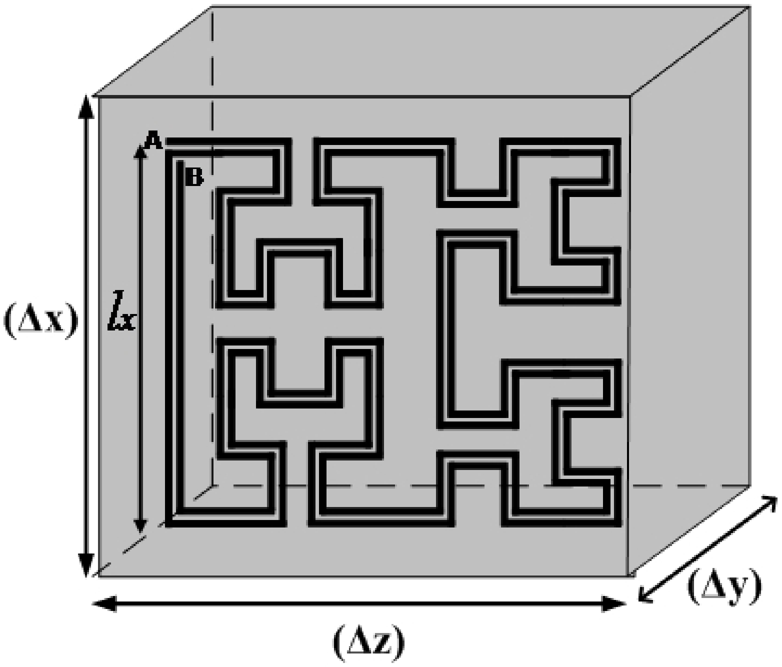

Figure 3.2: A unit cell of engineered magnetic substrate composed of inclusions with 3rd order Hilbert Curve.

Hilbert curve, the effective inductance would be dependent on n. L_{eff} is given as

$$L_{eff} = \frac{2\mu_0}{\Delta y} S = \frac{2\mu_0}{\Delta y} \begin{cases} 6(\frac{l_x}{2^n-1})^2 & n = 2 \\ \\ l_x^2 \frac{2^n - 2^{n-1} + 1}{2^n - 1} & n > 2 \end{cases} \tag{3.3}$$

where l_x is the dimension of the inclusion in the x direction (see Fig. 3.2). Equation (3.3) can be proved using mathematical induction principle [78].

The inclusion impedance, Z_{inc}, consists of two parts: R_{eff}, which models the ohmic loss of the metallic inclusions due to the finite conductivity of the strips, and the other part models the mutual impedance between external and internal loops, Z_{mut}. R_{eff}, can be calculated using the Ohm's law

$$R_{eff} = \frac{l_{total}}{\sigma(w\delta)}, \qquad \delta = \sqrt{\frac{2}{\omega\mu_0\sigma}} \tag{3.4}$$

where σ and δ are the conductivity and skin depth, respectively, w is the width of metallic strips and l_{total} is the total length of the metallic strips. l_{total} is given as

$$l_{total} = 2l_x \begin{cases} \frac{2^{2n}-2}{2^n-1} & n = 2 \\ \\ \frac{2^{2n}+2^n}{2^n-1} & n > 2 \end{cases} \tag{3.5}$$

Equation (3.5) can be proved using mathematical induction principle [78]. In the proposed inclusions, the internal loop follows the shape of the external loop, therefore the mutual impedance between external and internal loops Z_{mut} can be modeled as the per-unit-length mutual impedance of the strips, Z_{pul}, times the average length of the strips, l_{avg}.

$$Z_{mut} = Z_{pul} l_{avg} \tag{3.6}$$

where

$$l_{avg} = (l_x - 2w - g) \begin{cases} \frac{2^{2n}-2}{2^n-1} & n = 2 \\ \\ \frac{2^{2n}+2^n}{2^n-1} & n > 2 \end{cases} \tag{3.7}$$

and g is the gap between the metallic strips. The per-unit-length impedance, Z_{pul} is calculated using conformal mapping technique for the coplanar strip lines [60]

$$\begin{aligned} Z_{pul} &= \frac{1}{j\omega\epsilon_0\epsilon_r(1 - jtan\delta)} \frac{K(s)}{K(\sqrt{1-s^2})}, \\ s &= \frac{g}{g+2w}, \\ K(s) &= \int_0^{\frac{\pi}{2}} \frac{d\phi}{\sqrt{1 - s^2 \sin^2\phi}} \end{aligned} \tag{3.8}$$

where ϵ_r and $tan\delta$ are the relative permittivity and the loss tangent of the host substrate, respectively. The impedance given in (3.8) contains a parallel combination of a capacitance and a conductance to model the capacitance between the metallic strips and the loss due to the conductivity of the host substrate.

It should be noted that this model considers the capacitance between two adjacent strips while it neglects the capacitance between non-adjacent strips. Therefore, the accuracy of this model increases when the space between non-adjacent strips is much larger than the space between adjacent strips. However, for the compact structures or for high order fractal curves, where the space between non-adjacent strips is comparable to the space between adjacent strips, this model gives only an approximation of the relative permeability that can be used to initiate a design. To extract exact relative permeability, one needs to use the full wave simulation method explained in Section 2.5.2.

Using the above formulas, Table 3.1 compares the effective inductance, capacitance, resistance, and the resonance frequency of Hilbert inclusions with those parameters of the square spiral. For the spiral, the equations of section 2.5.4 are

Table 3.1: The ratio of the parameter of Hilbert inclusion to that of spiral

n	L_{eff}	C_{eff}	R_{eff}	Resonance Frequency
2	0.67	1.16	1.16	1.14
3	0.71	2.57	2.57	0.74
4	0.60	4.53	4.53	0.61
5	0.55	8.51	8.51	0.46
6	0.52	16.5	16.5	0.34

used. The electrical parameters of the host substrate and the geometrical parameters of the unit cell and metallic strips are assumed to be the same for all the Hilbert inclusions and spiral.

From Table 3.1, using fractal Hilbert inclusions instead of square spirals reduces the effective inductance while increasing the effective capacitance in such a way that the resonance frequency would be smaller for fractal Hilbert curves with $n > 2$. Therefore, using structures with Hilbert curves of order 3 or higher results in miniaturization of inclusions. We also observe that the miniaturization factor increases with the order of Hilbert curves.

Table 3.1 also gives higher value of effective resistance for Hilbert inclusions when compared to spirals. Increasing the effective resistance in the circuit model results in lower Q factor, which in turn results in lower rate of change in the resultant permeability with respect to frequency [79], [80]. Therefore, lower frequency dispersion can be achieved for the artificial medium. On the other hand, any increase in the effective resistance results in an increase in the magnetic loss of the artificial medium [79], [80]. Furthermore, since the effective inductance is reduced, it is expected that the maximum value of the relative permeability would be smaller for Hilbert inclusions when compared to spiral.

As a conclusion, the analytical models developed here predict that using fractal Hilbert curves with order 3 or higher results in miniaturization of the inclusions, and, furthermore, in a reduction of the frequency dispersion of the artificial medium. The drawbacks would be lower resultant permeability and higher magnetic loss. This conclusion will be verified in the next section using full wave numerical simulation.

3.4 Resultant Permeability

Using the aforementioned analytical and numerical methods, the relative permeability of the proposed structures in Fig. 3.1 was derived and the results are shown in Figs. 3.3 , 3.4. In these figures, the resultant permeability of Hilbert curve structures are compared to that of the square spiral. The parameters and dimensions of all the structures are the same and are given as: $s = w = 0.127$ mm, host dielectric of ($\epsilon_r = 3.38$, $tan\delta = 0.0027$), $l_x = 16$ mm, $\Delta y = 3.028$ mm, $\Delta x = \Delta z = 20$ mm, and the strips are assumed to be made copper to model the loss.

Figs. 3.3 and 3.4 show the real and imaginary parts of the resultant permeability, computed analytically and numerically. Good agreement was observed between the analytical and numerical results aside from a frequency shift reaching a maximum value of 8.8% for the case with 2nd order Hilbert curves.

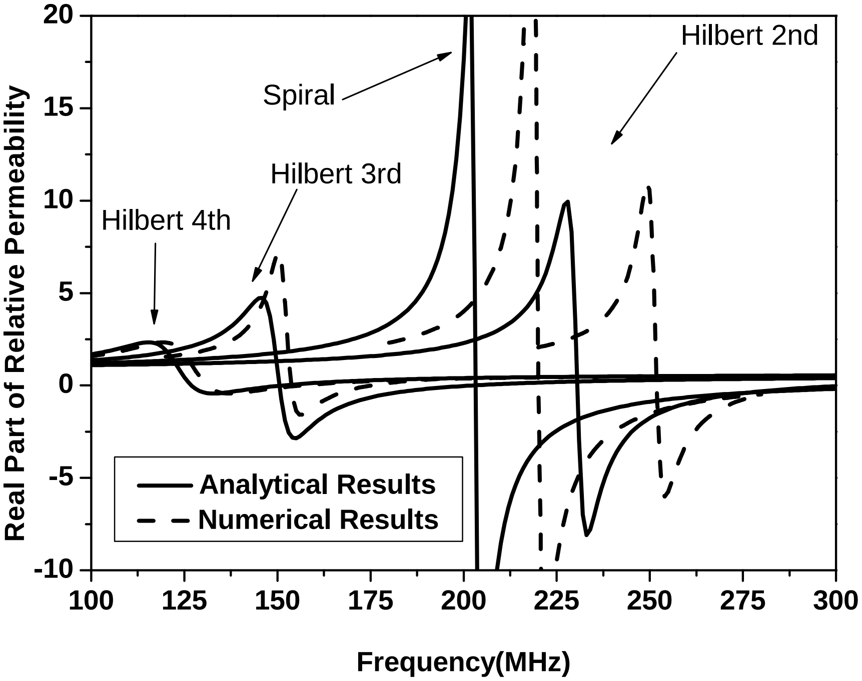

Figure 3.3: Real part of resultant permeability for engineered materials with inclusions shown in Fig. 3.1. Analytical results (solid line) are compared with numerical results (dash line).

As shown in Fig. 3.3, and Fig. 3.4, for $n > 2$, fractal structures exhibit lower resonance frequency compared to the spiral with the same size. Therefore, as predicted by the circuit model, for a given resonance frequency, using Hilbert inclusions

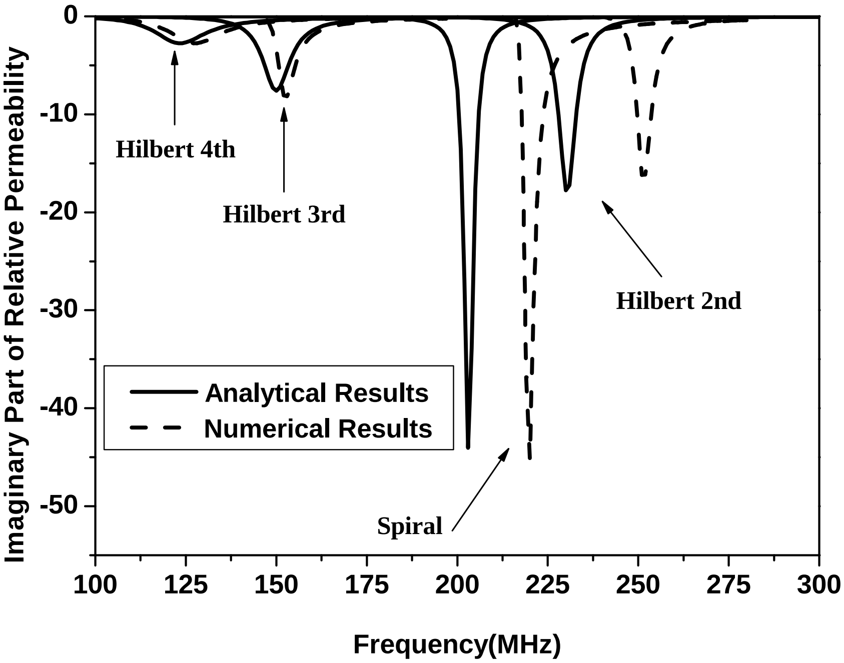

Figure 3.4: Imaginary part of resultant permeability for engineered materials with inclusions shown in Fig. 3.1. Analytical results (solid line) are compared with numerical results (dash line).

with order of 3 or higher results in a smaller size for the unit cell compared to the spiral. Furthermore, as shown in Fig. 3.3, when the order of the fractal Hilbert curve increases, the response of the permeability becomes smoother. Therefore, as predicted by the circuit model, using fractal structures decreases the rate of the permeability variation with respect to frequency leading to lower dispersion in the artificial substrate.

From Fig. 3.3, the maximum value achievable for the resultant permeability is smaller than that of the spiral, and this maximum value decreases as the order of Hilbert inclusions increases. This fact was also predicted by the circuit model as explained in the previous section. In terms of loss comparison, as shown in Fig. 3.4, at the resonance frequency Hilbert inclusions yield lower value for the imaginary part, so they provide lower loss at the resonant frequency. Notice that it is difficult to compare the imaginary parts at the other frequencies using the scale shown in Fig. 3.4. For this, we have presented the imaginary part of the permeability at the frequencies below the resonance in Fig. 3.5. In this figure, the numerical results are used, and for the sake of comparison, the frequency is normalized to the resonance frequency for all inclusions. As shown in Fig. 3.5, for frequencies below resonance, the imaginary part of the permeability is higher for Hilbert inclusions than that of the spiral inclusion, and as the order of Hilbert increases the imaginary part increases. Therefore, as predicted by the circuit model, at the frequencies below the resonance Hilbert inclusions provide higher loss when compared to spirals.

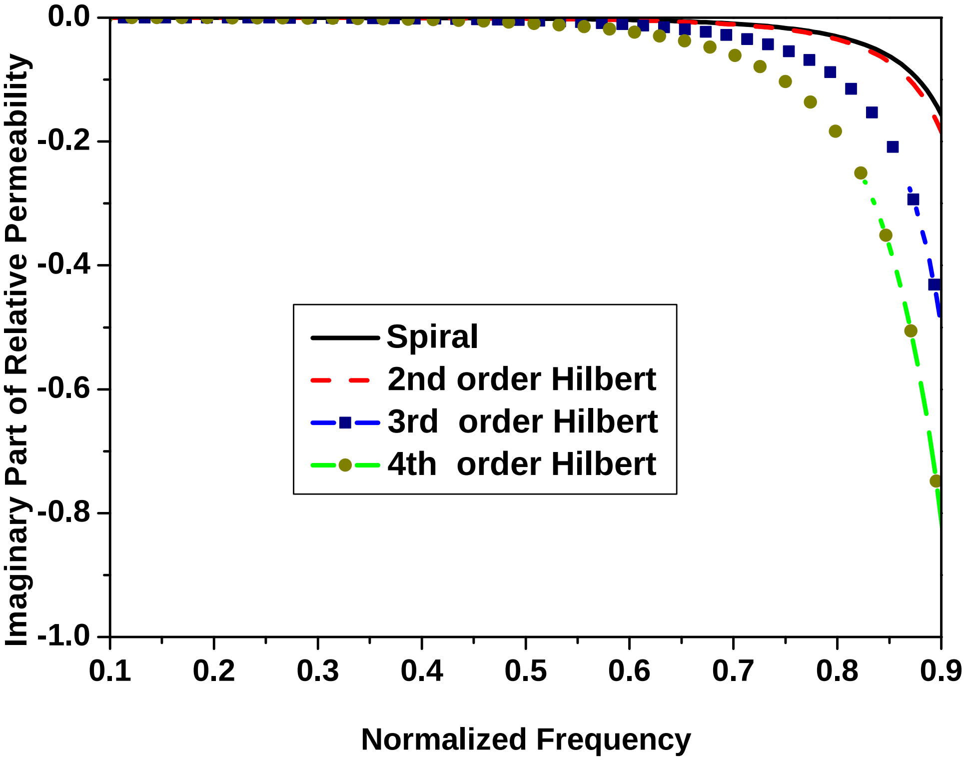

Figure 3.5: Imaginary part of the resultant permeability at frequencies below the resonance. The frequency is normalized to the resonance frequency.

We will verify the results archived here using measurement results in the chapters 4,5.

3.5 Conclusions

The use of fractal curves to miniaturize artificial magnetic materials was investigated. Novel configurations were proposed to realize artificial magnetic materials with smaller unit cells by combining the square spiral loop configuration with fractal Hilbert curves. The new designs are desirable when designing low profile miniaturized antennas in which the engineered magnetic materials are used as the substrate.

Analytical models were introduced to design and analyze the new structures. The analytical model was validated through full wave simulation characterization. It was shown that using forth order of fractal Hilbert curve, it is possible to realize inclusions as small as 0.014 of the wavelength in the dielectric. This size is 63% of the size of spiral inclusion and 32% of the size of SRR. Using higher order Hilbert curves results in even further miniaturization of the unit cell. In term of electromagnetic properties, the new structures provide lower frequency dispersion and lower magnetic loss at the resonance frequency in comparison to the square spiral inclusions. This advantage comes at the expense of lower permeability and higher magnetic loss at frequencies below resonance.

Chapter 4

New Experimental Method for Retrieval of Constitutive Parameters of Artificial Structures using a Microstrip Fixture

4.1 Introduction

The accurate retrieval of the constitutive parameters of artificial media is typically considered a challenging task due to the inherently highly resonant behavior of such media.

So far several experimental methods have been reported for retrieval of parameters of artificial structures such as the resonator method [42],[43], the free space method [44]–[46], and the waveguide method [47]-[48]. Each of these methods has its advantages and disadvantages. The resonator method provides high accuracy but it is inherently narrow band, and an individual measurement setup should be prepared for retrieval of the constitutive parameter at each single frequency; therefore, it is not a good candidate for measuring artificial magnetic materials which are dispersive in nature.

Acceptable accuracy was reported for the free space approach; however, an expensive setup of two horn antennas, combined with lens assemblies mounted on the horns, are required to generate plane waves [45]. Furthermore, Since standard horn antennas have limited operation bandwidth, to test artificial magnetic materials operating at different frequency bands, different setups are needed (for example, an antenna used for testing a structure which operates at 2 GHz cannot be used to test another structure which operates at 3 GHz).

In the waveguide method, the sample of artificial media is placed at the cross section of a waveguide and its constitutive parameters are calculated from reflected and transmitted waves [47]-[48]. The setup needed for this method is more affordable when compared to free space method, but again to test artificial magnetic materials operating at different frequency bands, different setups are needed. In addition, a large size sample of artificial magnetic materials is needed to fill the entire cross section of the waveguide. This would be a severe requirement when testing artificial materials operating at the lower band of microwave region, say few hundred MHz (for an artificial material operating at 500MHz, the sample size would be approximately 0.5m x 0.2m).

In this chapter, a broadband microstrip line-based method is proposed to measure the constitutive parameters of artificial magnetic materials. The advantage of this method over previously developed techniques is that the characterization can be performed using a simple inexpensive microstrip cell, and the same cell can be used for artificial magnetic materials operating at different frequency bands. Furthermore, in this method, there are fewer restrictions on the size of the sample under test.

Various microstrip line-based retrieval methods with different configurations were reported in the literature for characterization of natural materials [81]-[86], but no microstrip line-based method is reported for characterization of artificial magnetic materials which are in general biansotropic and dispersive.

The organization of this chapter is as follows: In section 4.2, the retrieval method is introduced and explained. In section 4.3, the proposed method is used to measure constitutive parameters of artificial magnetic materials with fractal Hilbert inclusions. Measurement results are presented and comparison is made to numerical simulation results.

4.2 Characterization Method

Artificial magnetic materials are in general anisotropic and dispersive; therefore a retrieval method should determine the permittivity and permeability tensors at different frequencies. The currently available artificial structures are realized by using planar inclusions with a specific topology in, say the x-y plane. These planar structures provide enhanced permeability only in the direction normal to the plane of the inclusion and enhanced permittivity in the directions tangent to the plane.

Here without any loss of generality, it is assumed that the inclusions lie in the x-z plane. In this case the permeability of the artificial structure is described by the following tensor:

$$\mu(\omega) = \mu_0 \begin{pmatrix} 1 & 0 & 0 \\ 0 & \mu_y(\omega) & 0 \\ 0 & 0 & 1 \end{pmatrix} \tag{4.1}$$

Fig. 4.1 shows the proposed setup for permeability retrieval consisting of a shorted microstrip line with the substrate of the line being the artificial media under test. By measuring the input impedance of the shorted microstrip line over the frequency range of interest, the permeability of the artificial media can be calculated. For the quasi-TEM dominant mode in the microstrip line (see Fig. 4.1,) the dominant magnetic field in the substrate will be in the y direction. Therefore this configuration can be used for the retrieval of μ_y. For the quasi-TEM mode, the dominant mode in the microstrip line, the input impedance of the shorted line is given by

$$Z_{in} = Z_{0M}\sqrt{\frac{\mu_{eff,y}}{\epsilon_{eff,x}}}\tanh(jl\beta_0\sqrt{\mu_{eff,y}\epsilon_{eff,x}}), \tag{4.2}$$

where l, and β_0 are the length of the shorted microstrip line and the propagation constant of the air, respectively. $\epsilon_{eff,x}$, and $\mu_{eff,y}$ are the x-directed effective permittivity, and y-directed effective permeability of the microstrip cell respectively. Z_{0M} is the characteristic impedance of the microstrip cell for $\mu_r = \epsilon_r = 1$, given by [87]

$$Z_{0M} = \frac{120\pi}{\frac{w}{h} + 1.393 + 0.677ln(1.444 + \frac{w}{h})} \tag{4.3}$$

where w is the width of the microstrip line and h is the height of the substrate. The $\epsilon_{eff,x}$ in Eq. (4.2)can be calculated as [88]

$$\epsilon_{eff,x} = \begin{cases} \frac{1+\epsilon_x}{2}(\frac{A}{A-B})^2 & \frac{w}{h} \leq 2 \\ \\ \epsilon_x(\frac{C-D}{C})^2 & \frac{w}{h} > 2 \end{cases} \tag{4.4}$$

where

$$\begin{aligned}
A &= \ln(\frac{8h}{w}) + \frac{1}{32}(\frac{w}{h})^2 \\
B &= \frac{1}{2}(\frac{\epsilon_x - 1}{\epsilon_x + 1})[\ln(\frac{\pi}{2}) + \frac{1}{\epsilon_x}\ln(\frac{4}{\pi})] \\
C &= \frac{w}{2h} + \frac{1}{\pi}\ln(2\pi e[\frac{w}{2h} + 0.94]) \\
D &= \frac{\epsilon_x - 1}{2\pi\epsilon_x}[\ln(\frac{\pi e}{2}(\frac{w}{2h} + 0.94)) - \frac{1}{\epsilon_x}\ln(\frac{e\pi^2}{16})],
\end{aligned}$$

and ϵ_x is the x-directed permittivity of the artificial media. ϵ_x will be measured using a parallel plate metamaterial capacitor as proposed in [1]. By measuring the capacitance, the permittivity can directly be calculated. According to the classical image theory, using only one period of the artificial unit cells in the area between the two metallic parallel plates can mimic the behavior of an infinite array of unit cells , which is the default assumption in the analysis and design of artificial structures. These aspects, therefore, makes the method presented in [1] highly robust and well-suited for metamaterial characterization. It is interesting to note, however, that the authors of [1] observed a rather large difference between the analytically estimated and measured permittivity values (a difference of more than 30%). The large discrepancy is in fact due to the approximations used in the derivation of the analytical formula. For the same artificial structure measured in [1], we have performed a full wave numerical simulation using the simulation setup discussed in Chapter 2, and [89] and obtained a difference between simulation and measurements of less than 7%.

Next, the input impedance of the shorted microstrip line is measured, and by solving (4.2), the unknown parameter, $\mu_{eff,y}$ is determined. The effective permeability, in general, is a complex number, and (4.2) should be solved for both the real part, $\mu^{'}_{eff,y}$, and the imaginary part, $\mu^{''}_{eff,y}$. Then, after finding the effective permeability, the relative permeability of the substrate, μ_y, is calculated by solving the following equations [88]:

$$\mu^{'}_{eff,y} = \begin{cases} \frac{2\mu^{'}_y}{1+\mu^{'}_y}(\frac{A-B^{'}}{A})^2 & w/h \leq 2 \\ \\ \mu^{'}_y(\frac{C}{C-D^{'}})^2 & w/h > 2 \end{cases} \tag{4.5}$$

$$\mu^{''}_{eff,y} = \mu^{''}_y \frac{\mu^{'}_{eff,y} - (\mu^{'}_{eff,y})^2}{\mu^{'}_y - (\mu^{'}_y)^2} \tag{4.6}$$

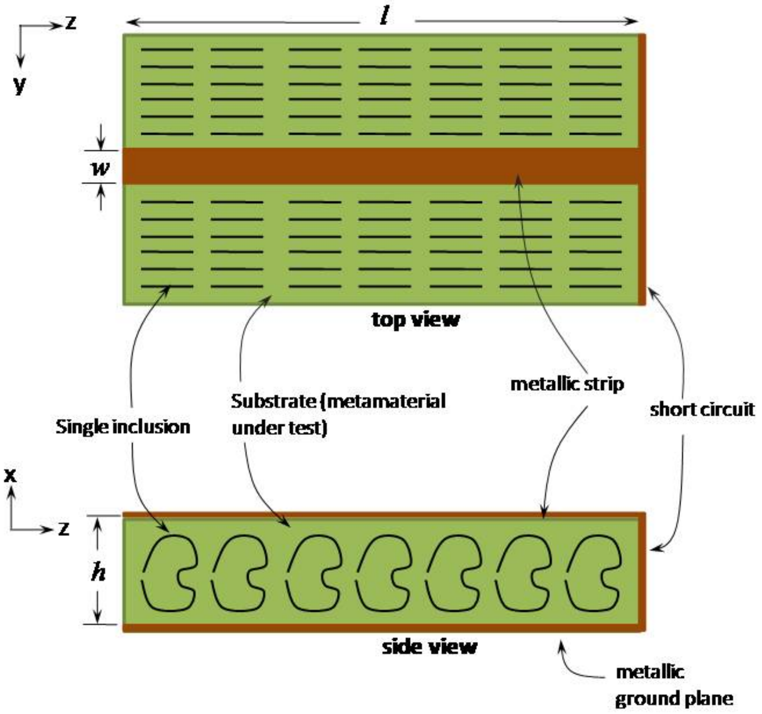

Figure 4.1: The setup configuration used for extraction of the permeability of the artificial media

where A and C were introduced before and $B^{'}$ and $D^{'}$ are given by:

$$\begin{aligned} B^{'} &= \frac{1}{2}\left(\frac{1-\mu_y^{'}}{1+\mu_y^{'}}\right)[\ln(\frac{\pi}{2}) + \mu_y^{'}\ln(\frac{4}{\pi})] \\ D^{'} &= \frac{1-\mu_y^{'}}{2\pi}[ln(\frac{e\pi}{2}(\frac{w}{2h}+0.94)) - \mu_y^{'}\ln(\frac{e\pi^2}{16})], \end{aligned}$$

where $\mu_y^{'}$ and $\mu_y^{"}$ are the real and imaginary parts of the permeability of the artificial media respectively.

(4.5), and (4.6) are derived in [87], [88] using conformal mapping technique where the permeability, $\mu_y^{'}$, was assumed positive. Therefore, these equations cannot be used over the frequency range where the permeability is negative. Therefore, this method can be used only for applications which artificial magnetic materials are designed to operate at frequencies over which the permeability is positive. In the next chapter, we propose a new method which can be used for both positive and negative permeability.

(4.5), and (4.6) are nonlinear equations and can be solved by several numerical methods such as the Gauss-Newton method, the Levenberg-Marquardt method, the Trust-Region Dogleg method, ... etc. [90]. In this work, the Trust-Region Dogleg method is used. The process of characterization is summarized in the chart shown in Fig. 4.2.

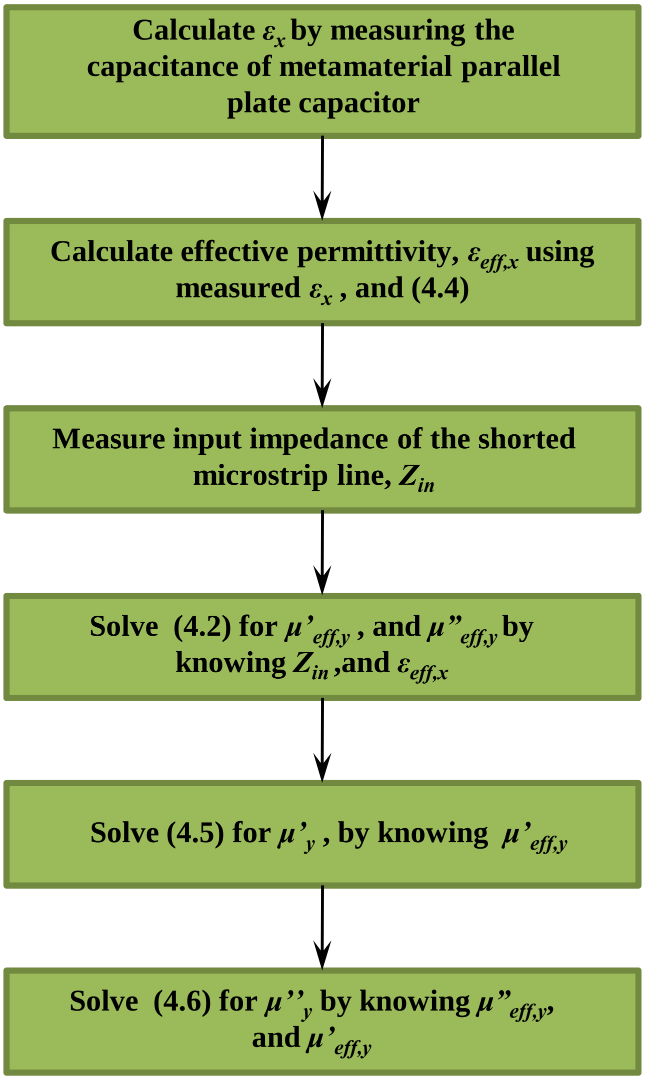

Figure 4.2: Characterization Process

4.3 Measurement Results

To test the accuracy of the proposed method for extracting the permeability of artificial magnetic materials, we consider the structure with fractal Hilbert2 inclusions introduced in the previous chapter. One unit cell of this structure is shown in Fig. 4.3. The inclusion consists of a conducting trace having a width of $w = 0.180$mm and separation between traces of $s = 0.180$mm. This artificial media was fabricated and measured, and in this section, we compare the measurement results with numerical simulation results.

The numerical results are obtained using Ansoft HFSS10, and the numerical setup explained in chapter 2. In the numerical setup, a unit cell of the artificial material combined with periodic boundary conditions are used to mimic an infinite slab of artificial materials. For numerically extraction of the constitutive parameters, plane wave analysis is used, and parameters are extracted from the reflected and transmitted waves from the unit cell [89].

Using printed circuit technology, a strip of 6 unit cells of fractal Hilbert2 inclusions were fabricated on an FR4 substrate with $\epsilon_r = 4.4$, and $tan\delta = 0.02$ (See Fig. 4.4). Forty of these strips were then stacked in the y direction to provide a three-dimensional substrate. Due to the thickness of the metal inclusions, an average air gap of 50 μm develops between the strips in the stacking process. The air space while unavoidable in the fabrication process is nevertheless measurable, so it can be easily included in the design. Using this substrate and conducting plates, a parallel-plate metamaterial capacitor was fabricated, and by measuring its capacitance, the permittivity was extracted. According to this measurement, the permittivity for this artificial magnetic substrate is calculated as $\epsilon_x = 9.6$. The numerical full-wave simulation results in $\epsilon_x = 9.58$, demonstrating strong agreement with measurements. The 50 μm air gap is included in the simulation.

The same substrate that is used for permittivity measurement is used as a substrate of the shorted microstrip line to extract the permeability. The fabricated fixture used for permeability measurement is shown in Fig. 4.5. The fabricated substrate has dimensions of 12, 8.2, and 1.1 cm in the y, z, and x directions, respectively. For the quasi-TEM dominant mode, the **H** and **E** fields in the substrate will be in the y and x directions, respectively. Therefore this configuration can be used for retrieval of μ_y.

Using a vector network analyzer, the complex input impedance of the shorted microstrip line shown in Fig. 4.5 is measured over the frequency range of 500-680 MHz (See Fig. 4.6). Then using the measured value of $\epsilon_x = 9.6$ and measured impedance, μ_y is extracted by the method explained in section 4.2. The real and imaginary parts of the measured y-directed permeability are shown in Fig. 4.7, and Fig. 4.8. In these figures, the measurement results are compared with the numerical simulation results. The 50 μm air gap was also included in the simulation.

The shaded area in Fig. 4.7, and Fig. 4.8 determines the frequencies over which the real part of the permeability is negative. Over this frequency range correspond-

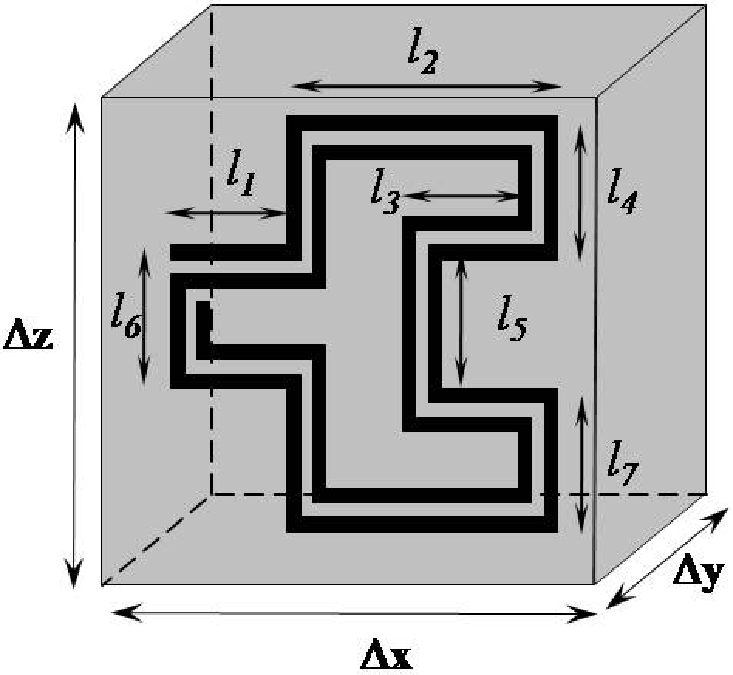

Figure 4.3: Fractal Hilbert2 inclusion used for constructing artificial magnetic material. $l_1 = l_3 = l_4 = l_5 = l_6 = l_7 = 3.03mm, l_2 = 6.06mm, \Delta y = 3.028mm, \Delta x = \Delta z = 11mm$

Figure 4.4: A single strip containing 6 unit cells of inclusions fabricated using printed circuit board technology.

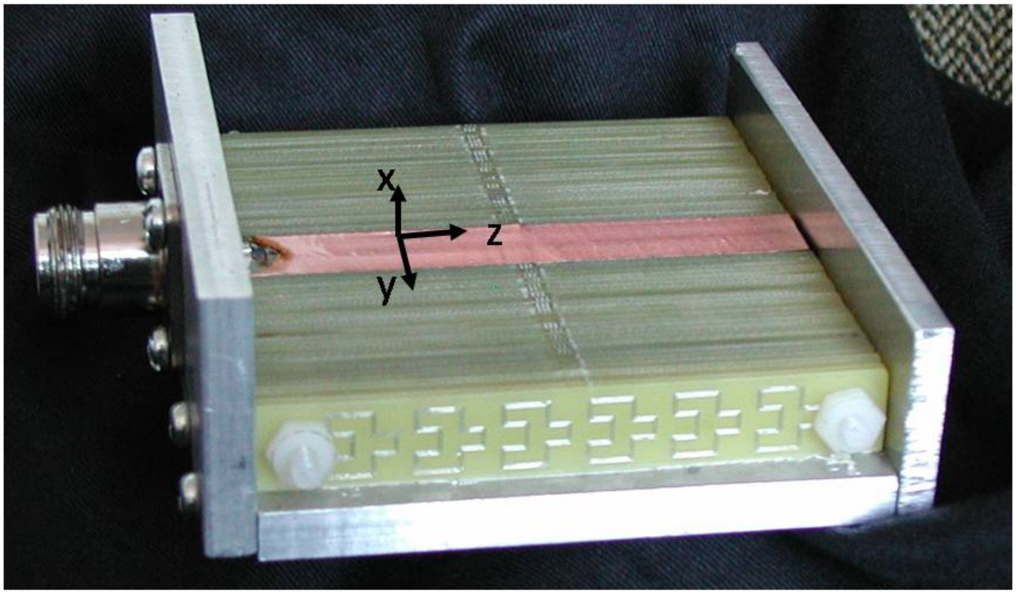

Figure 4.5: The fabricated fixture used for permeability measurement

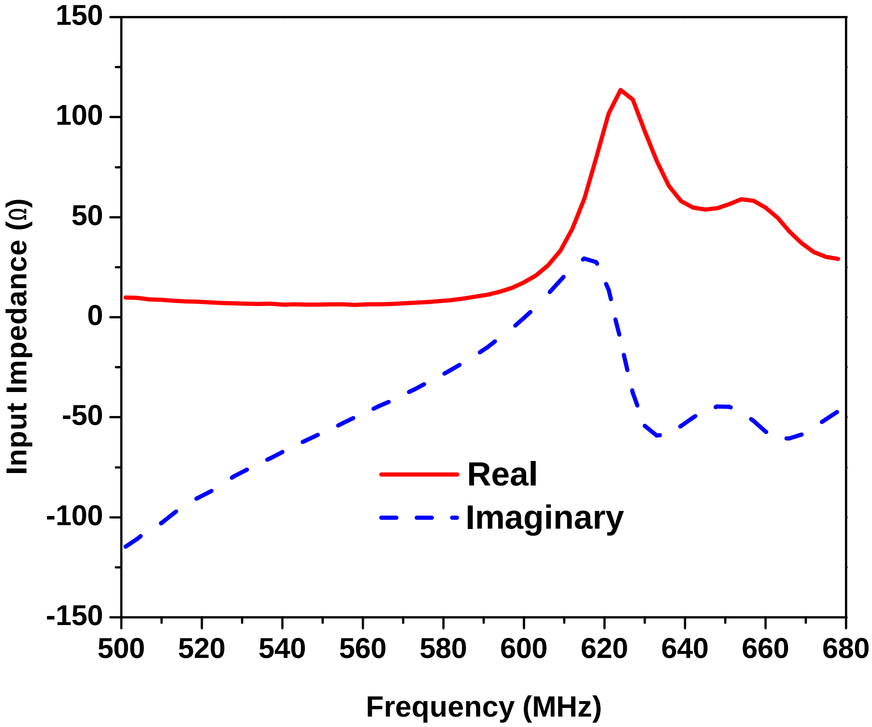

Figure 4.6: Measured Input Impedance

ing to frequencies higher than 638 MHz, as explained before, the measurement results are not valid. Over the frequency range where the real part of the permeability is positive, good agreement is observed between the simulation and measurement results.

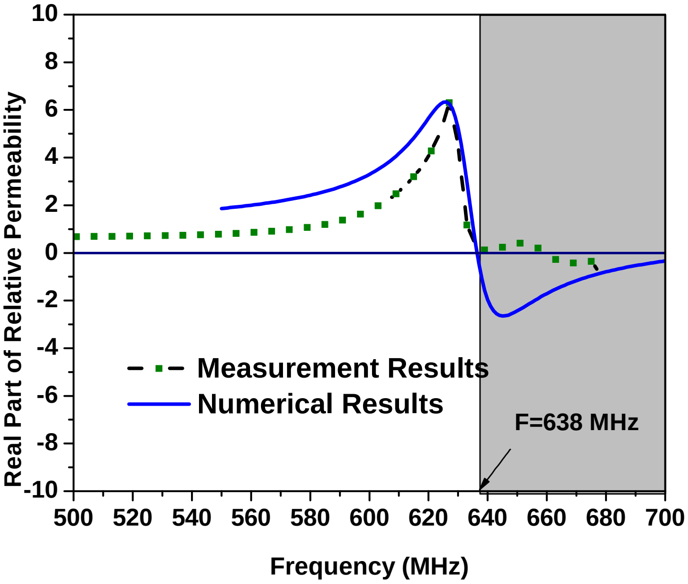

Figure 4.7: The measured and numerically simulated real part of the permeability for the artificial magnetic material shown in Fig. 4.5.

As briefly discussed above and more extensively in [89], in the numerical analysis used in [89], periodic boundary conditions are used to mimic an infinite number of unit cells. However, in practice we can realize only finite number of unit cells. For example in the setup used in this work (see Fig. 4.5), the fabricated substrate contains 6 unit cells of inclusions in the z direction, and only one unit cell in the x direction. It can be predicted that increasing the number of unit cells provide higher homogeneity in the fabricated substrate which will result in a better agreement between numerical and measurement results. On the other hand, in a wide class of applications such as antenna miniaturization, only one unit cell is used in the x direction to avoid high profile substrates [1],[31].

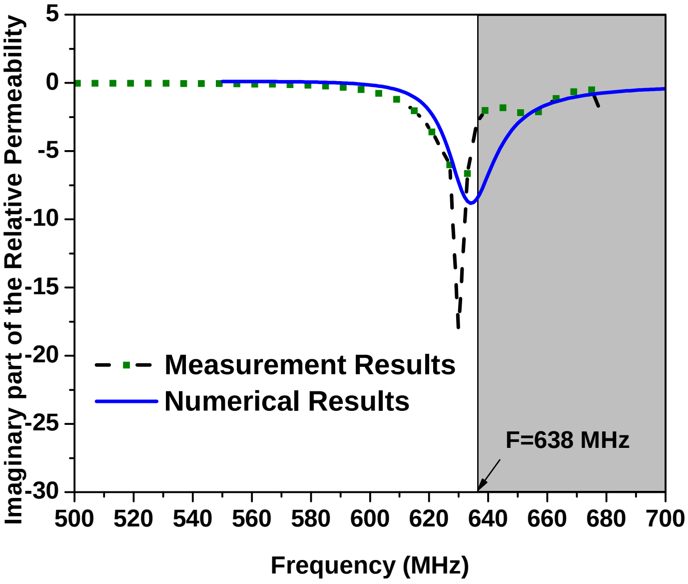

Figure 4.8: The measured and numerically simulated imaginary part of the permeability for the artificial magnetic material shown in Fig. 4.5.

4.4 Conclusion

A method based on the shorted microstrip line was proposed for characterization of artificial magnetic materials. The retrieval method for permeability extraction was introduced and explained. An artificial substrate based on fractal Hilbert inclusions was fabricated and characterized using the proposed method. Measurement results were presented and compared with numerical results of a full wave simulation. Numerical results were obtained from a plane wave analysis using a finite element simulation tool. A strong agreement was observed between measurement and numerical results.

The primary advantage of the method introduced here in comparison to previous methods, is its relatively low cost (in comparison to the free space or the waveguide methods) and its capability of extracting the permeability over a wide band of frequencies (in comparison to the resonator method).

Chapter 5

A New Retrieval Method for Characterization of Metamaterials Using a Strip Line Fixture

5.1 Introduction

As we saw in the previous chapter, the microstrip line method, has the advantage of low cost (in comparison to the free space or the waveguide methods) and its capability of extracting the permeability over a wide band of frequencies (in comparison to the resonator method) [91]. However, the microstrip line method dose not work properly for negative values of constitutive parameters [91],[27]. Furthermore, in the microstrip line method, two measurement setups are needed to extract permittivity, and permeability individually.

In this chapter, a new method based on strip line structures is presented for characterization of artificial structures. The proposed method is able to be used for characterization of all types of artificial structures including SNG (Single Negative), and DNG (Double Negative)metamaterials. The new method has the advantages of easy fabrication and low cost, when compared to free space or the waveguide methods. Furthermore, it has the advantage of being able to extract both permittivity, ϵ, and permeability, μ, with one measurement, when compared to microstrip line method. In addition, the new method works for both positive and negative values of μ, and ϵ, which is another advantage when compared to microstrip line method.

The organization of this chapter is as follows. First in the section 5.2, the retrieval method is explained. Then using numerical full wave analysis, the accuracy of the method has been verified for various type of metamaterials in section 5.3. In section 5.4, the method has been used for experimental characterization of artificial magnetic materials with unit cells of 3rd order fractal Hilbert configuration, and a comparison is made between measurement results, and numerical simulation results. Finally, a summery and conclusion is presented in 5.5.

5.2 Retrieval Method

The setup configuration is shown in Fig. 5.1. This setup is used to extract both permittivity and permeability. The setup consists of a two-port strip line fixture. The substrate of the strip line includes three parts: two double positive dielectric with known constitutive parameters at sides next to the excitation ports, and the under test metamaterial structure placed in the middle. By measuring the scattering parameters of this two-port strip line fixture, the permittivity and permeability of the under test metamaterial structure are extracted. For the quasi-TEM mode, the dominant mode in strip line structures, the y component of the magnetic field and the x component of the electric field are the dominant field components in the setup shown in Fig. 5.1. Therefore this configuration can be used for the retrieval of the μ_y, and ϵ_x.

The method used here is very similar to the the free space approach [44]–[46], in terms of the theoretical base. Both methods extract the unknown constitutive parameters from reflection and transmission of waves from the artificial sample. However, from fabrication and measurement point of view, in this method a simple inexpensive strip line fixture can be used, while in the free space approach, an expensive setup of two horn antennas, combined with lens assemblies mounted on the horns, are required to generate plane waves [44]. Furthermore, the size of the artificial sample required for the strip line method is much smaller when compared to the sample required for the free space approach.

For the dominant quasi-TEM mode, the transmission line model shown in Fig. 5.2 is used to analyze the behavior of the field in the substrate. According to this model, the voltage and current in all three regions are formulated by

$$RegionI : V_I = e^{-jk_d z} + \Gamma e^{+jk_d z}, I_I = \frac{1}{Z_d}(e^{-jk_d z} - \Gamma e^{+jk_d z}), \tag{5.1}$$

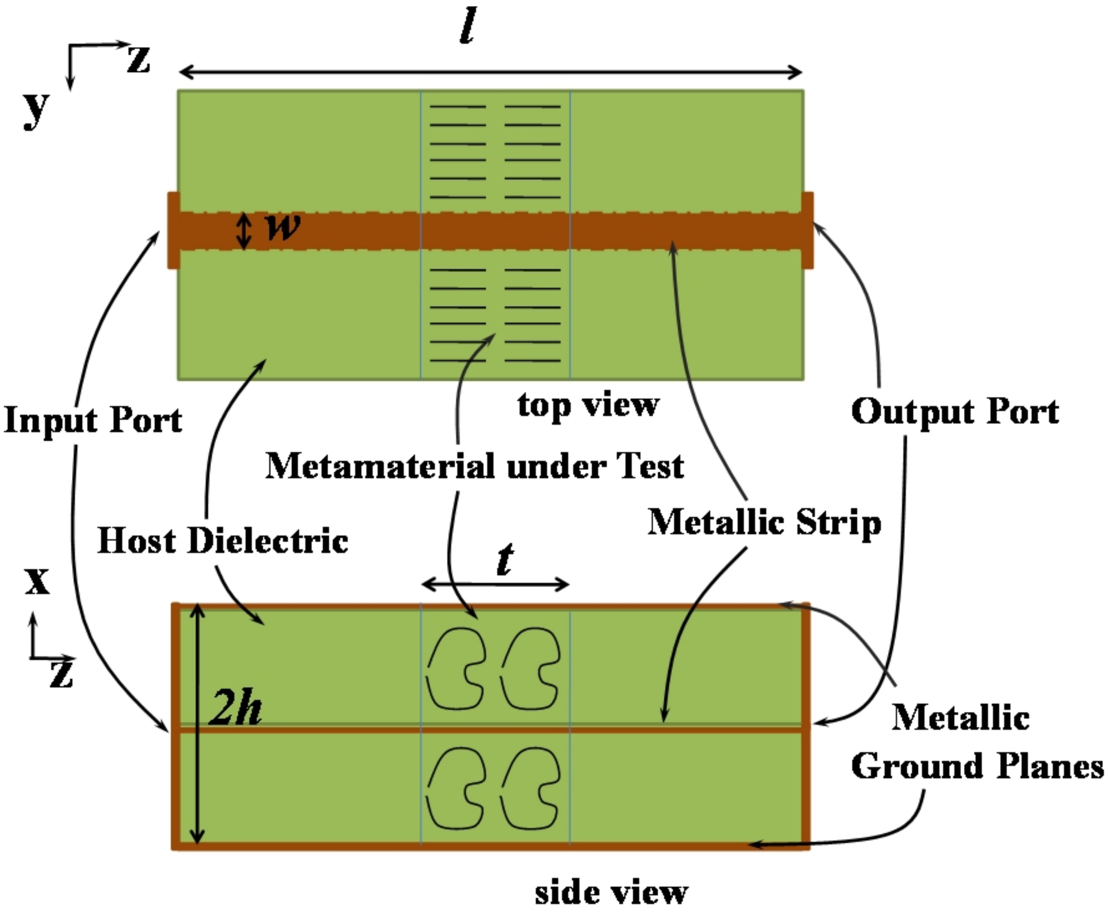

Figure 5.1: The setup configuration for the strip line fixture used for extraction of the permittivity and permeability of the artificial media

$$RegionII : V_{II} = Ce^{-jk_m z} + De^{+jk_m z}, I_{II} = \frac{1}{Z_m}(Ce^{-jk_z z} - De^{+jk_z z}), \tag{5.2}$$

$$RegionIII : V_{III} = Te^{-jk_d(z-t)}, I_{III} = \frac{T}{Z_d}e^{-jk_d(z-t)} \tag{5.3}$$

where k_d , and Z_d are the propagation constant and characteristic impedance in the known dielectric (Regions I, and III in Fig. 5.2) respectively. Since the known dielectric is nonmagnetic and isotropic, k_d , and Z_d can be written as [92].

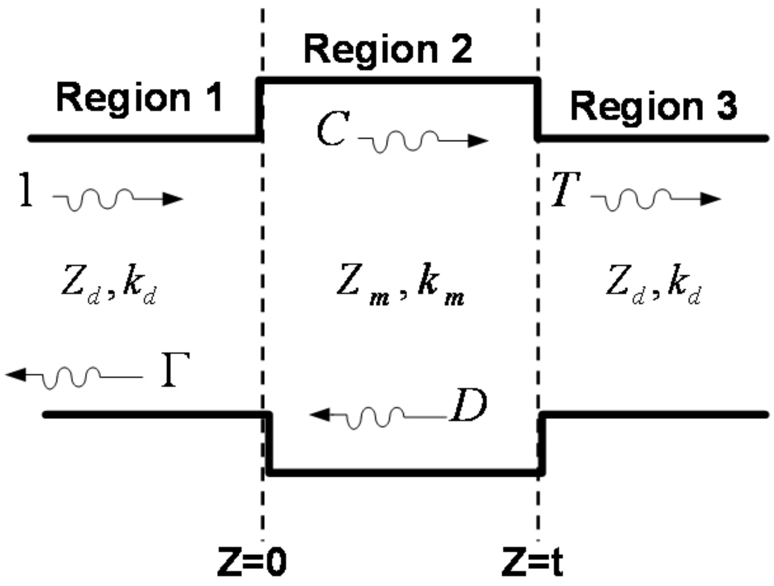

Figure 5.2: The transmission line model of the setup configuration in Fig. 5.1

$$\begin{aligned} k_d &= \omega\sqrt{\epsilon_0\epsilon_d\mu_0} \\ Z_d &= 30\pi\sqrt{\frac{\mu_0}{\epsilon_0\epsilon_d}}\frac{h}{W_e+0.441h}, \qquad W_e = \begin{cases} W & \frac{W}{h} > 0.35 \\ W - h(0.35-\frac{W}{h})^2 & \frac{W}{h} < 0.35 \end{cases} \end{aligned} \tag{5.4}$$

where W is the width of the strip line, h is the total height of the substrate, and ϵ_d is the relative permittivity of the known dielectric. In (5.2), k_m, and Z_m are the propagation constant and characteristic impedance in the unknown artificial sample, respectively. Since the artificial sample is in general anisotropic, the direction of **E** field and **H** field should be considered when deriving k_m, and Z_m. For the quasi-TEM mode, the dominant E field component is in the x direction, and the dominant H field component is in the y direction. Therefore k_m, and Z_m are formulated as

$$\begin{aligned} k_m &= \omega\sqrt{\epsilon_0\mu_0\epsilon_x\mu_y} \\ Z_m &= 30\pi\sqrt{\frac{\mu_0\mu_y}{\epsilon_0\epsilon_x}}\frac{h}{W_e+0.441h}, \qquad W_e = \begin{cases} W & \frac{W}{h} > 0.35 \\ W - h(0.35-\frac{W}{h})^2 & \frac{W}{h} < 0.35 \end{cases} \end{aligned} \tag{5.5}$$

where μ_y is the permeability in the y direction, and ϵ_x is the permittivity in the x direction. In order to express permittivity and permeability of the artificial material in terms of the measured S-parameters, (5.1) - (5.3) are solved by applying the boundary conditions at $z = 0$ and $z = t$. Permittivity and permeability of the artificial material can be calculated by using the following relations:

$$\begin{aligned}
\mu_y &= \frac{Z_m k_m}{Z_d k_d}, \qquad \epsilon_x = \frac{\epsilon_d k_m Z_d}{Z_m k_d} \\
Z_m &= \pm Z_d \sqrt{\frac{(1+\Gamma)^2 - T^2 e^{-j2k_d t}}{(1-\Gamma)^2 - T^2 e^{-j2k_d t}}}, \qquad \Gamma = S_{11} e^{-j2k_d d} \quad T = S_{21} e^{-j2k_d d} \\
e^{-jk_m t} &= X \pm j\sqrt{1 - X^2}, \qquad X = \frac{1 - \Gamma^2 + T^2 e^{-j2k_d t}}{2T e^{-jk_d t}} \qquad (5.6)
\end{aligned}$$

It should be noted that as shown in (5.6), the extracted parameters, μ_y, ϵ_x, are proportional to the ratio of Z_m, and Z_d, not their absolute values. Therefore, any approximation used in deriving the impedances ,Z_m, Z_d, dose not affect the accuracy of the extracted parameters μ_y, ϵ_x, since this approximation is the same for both Z_m, Z_d, and will be canceled in their ratio. In the above equations, only the dominant electric and magnetic fields are considered. However, in the strip line structure, the y component of $\mathbf{E}$ field as well as the x component of $\mathbf{H}$ field which are ignored in (5.5) and (5.6) are present in the field distribution. In the case of isotropic sample, since the permittivity and permeability is the same in all the directions, this fact does not affect the accuracy of the results. However, in the case of anisotropic artificial materials, neglecting the non-dominant field components is expected to affect the accuracy of the extracted permittivity and permeability. In Section 5.3, using full wave numerical analysis, this phenomena is investigated, and a solution is proposed to address it.

5.3 Full Wave Numerical Analysis

To investigate the accuracy of the method, a full wave numerical simulation is done for both isotropic and anisotropic samples. The commercial software, HFSS is used for full wave numerical simulation.

5.3.1 Results for Isotropic Samples

First we assume the sample under test be isotropic, so it has the same permittivity and permeability at all the directions. To test the method for artificial samples with frequency-dependent constitutive parameters, a metamaterial with constitutive parameters shown in Fig. 5.3 is used as the sample under test. The data shown in Fig. 5.3 is generated using the well known lorentz model [93] for both permittivity and permeability:

$$\begin{aligned} \epsilon_r &= 1 + \frac{f_{pe}^2}{f_{0e}^2 - f^2 + jG_e f} && (5.7) \\ \mu_r &= 1 + \frac{f_{pm}^2}{f_{0m}^2 - f^2 + jG_m f} && (5.8) \\ & && (5.9) \end{aligned}$$

where the parameters in the above equations are selected as: $f_{pe} = 350MHz$, $f_{pm} = 380MHz$, $f_{0e} = 520MHz$, $f_{0m} = 550MHz$,and $G_e = G_m = 25e6$ The data

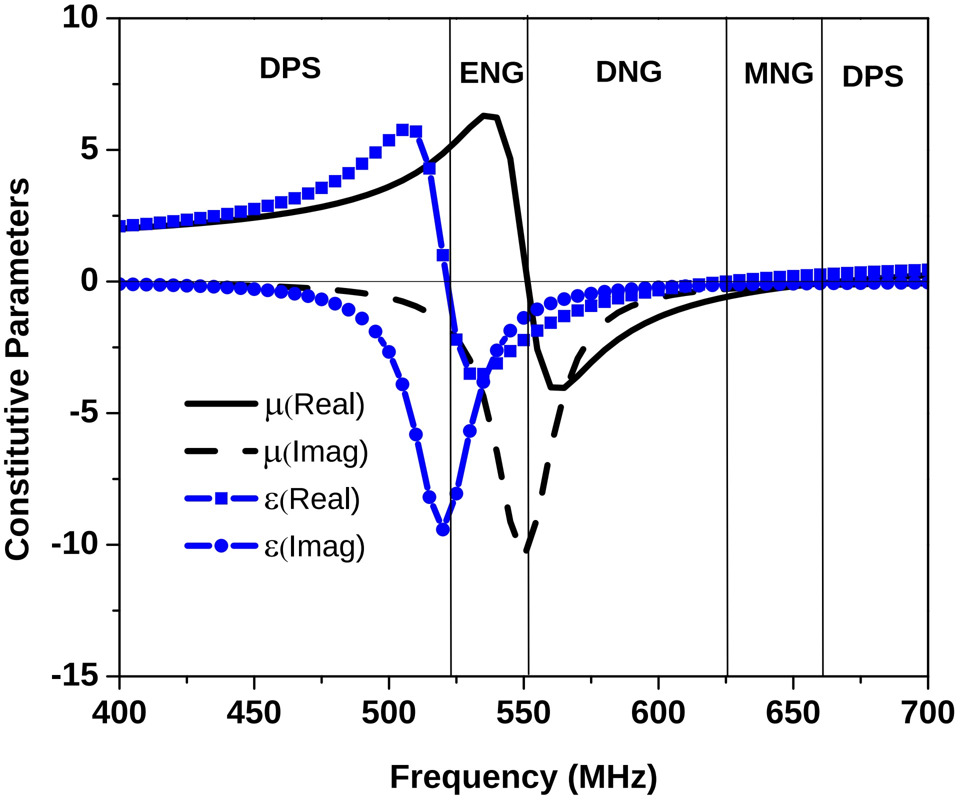

Figure 5.3: The constitutive parameters of the sample under test (Frequency-dependent case)

shown in Fig. 5.3 includes all the possible cases for constitutive parameters : DP (double positive), ENG(Epsilon negative), MNG(Mu Negative), and DNG (double

Negative). Therefore, by simulating these parameters, the accuracy of the method will be verified for all types of metamaterials. The extracted parameters using full wave simulation for the the data shown in Fig. 5.3 are shown in Figs. 5.4, 5.5, and compared with the actual data. As shown in these figures, there is a strong agreement between the extracted parameters and the actual data such that it is hard to distinguish between them. In this simulation, the physical, and electrical parameters of the strip line fixture (See Fig. 5.1) are chosen as follows: l=23 cm, t=2 cm, h=11 mm, W=18 mm, the host dielectric is Rogers RT/duroid 5880 with ϵ_d=2.2, and $tan\delta$=0.0009.

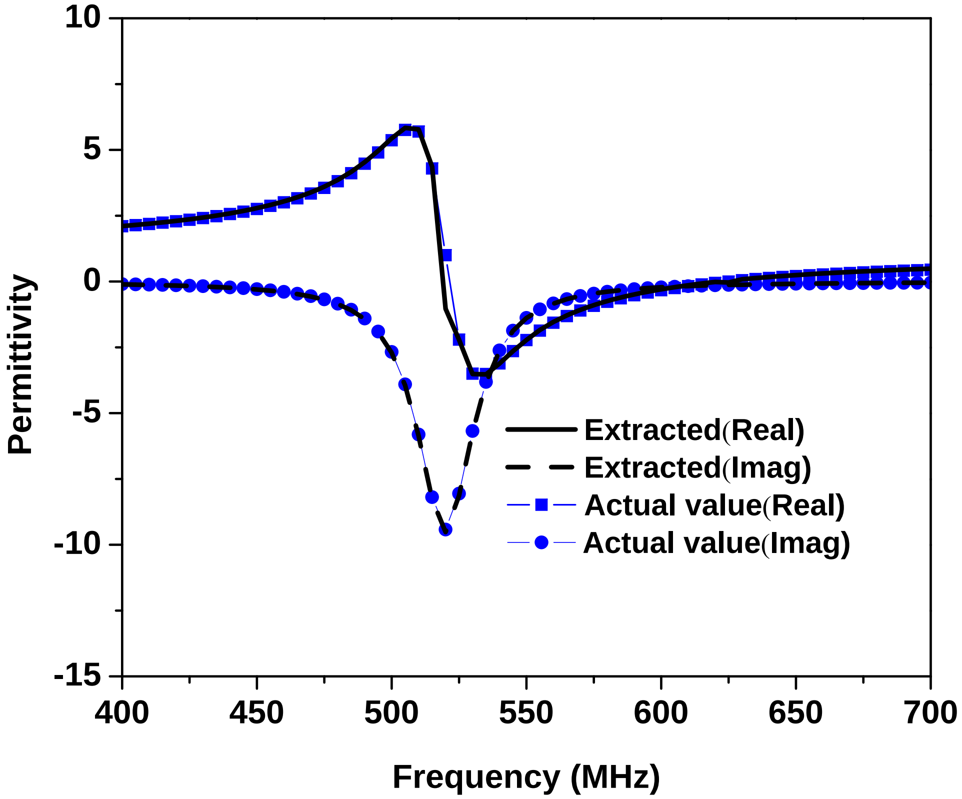

Figure 5.4: Extracted permittivity for the data shown in Fig. 5.3.

5.3.2 Results for Anisotropic Metamaterial and Fitting Solution

Usually metamaterial designs and applications involve anisotropy in the structure. Therefore characterization of the anisotropic samples using the proposed method

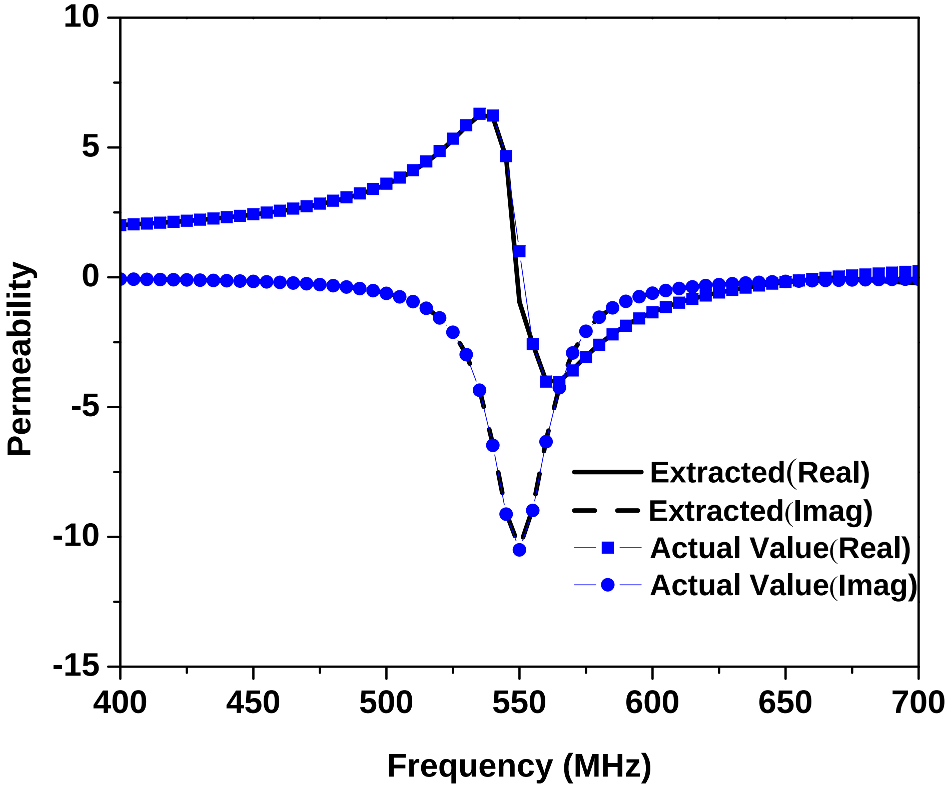

Figure 5.5: Extracted permeability for the data shown in Fig. 5.3.

has a practical importance. The equations used for extraction of permittivity and permeability from S_{21} and S_{11} are derived by neglecting the effect of non-dominant field components on the characteristic impedance and propagation constant. Therefore, we expect some deviation between the extracted parameters and the actual value of parameters when the sample is anisotropic. To present a quantitative study on this deviation, we assume a sample with following tensors as the permittivity and permeability:

$$\epsilon = \epsilon_0 \begin{pmatrix} \epsilon_x & 0 & 0 \\ 0 & 2.2 & 0 \\ 0 & 0 & \epsilon_z \end{pmatrix} \tag{5.10}$$

$$\mu = \mu_0 \begin{pmatrix} 1 & 0 & 0 \\ 0 & \mu_y & 0 \\ 0 & 0 & 1 \end{pmatrix} \tag{5.11}$$

First we assume a frequency-independent sample with constant values for $\epsilon_x = \epsilon_z$, and μ_y. Figs. 5.6, and 5.7 illustrate the results of this simulation. In these figures, extracted values of constitutive parameters are plotted versus actual values of these parameters. Fig. 5.6 shows the results for extracted permittivity ϵ_x, and Fig. 5.7 shows the results of extracted permeability μ_y. In this simulation, the physical, and electrical parameters of the strip line fixture are the same as parameters used in the simulation of section 5.3.1.

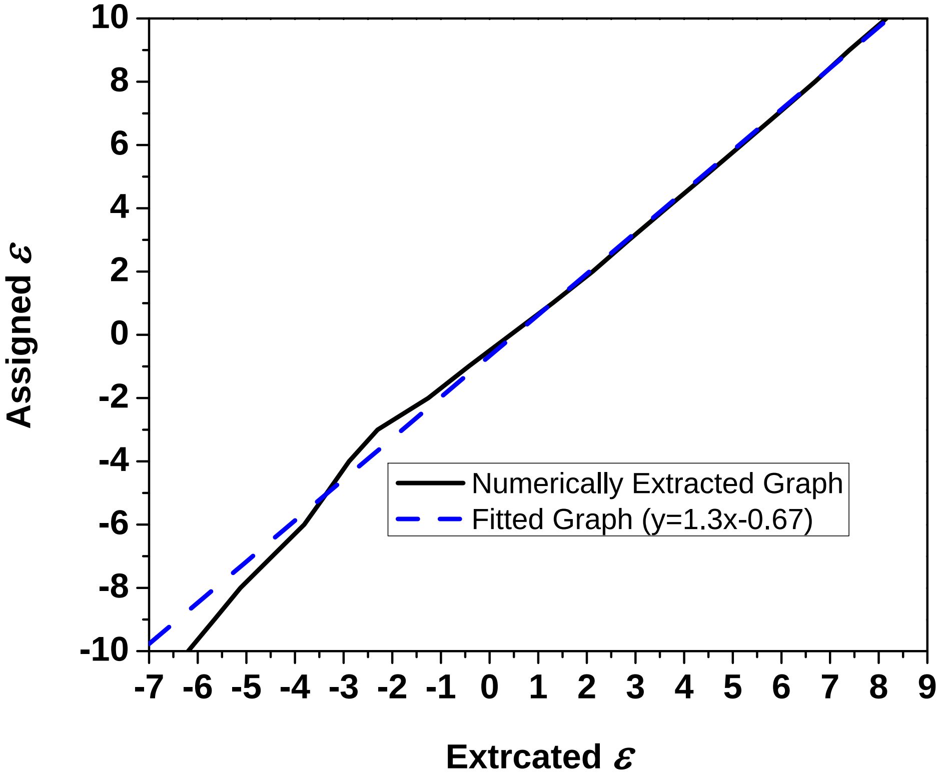

Figure 5.6: Results of simulation for anisotropic sample. Extracted permittivity is plotted versus actual value of permittivity.

Using fitting curve tool in Matlab, we approximated the graphs of Fig. 5.6, and 5.7 with polynomials. The fitted polynomials are shown in the same figures. The formulas of the resultant polynomials are illustrated in (5.12), and (5.13).

$$\mu_y = -0.0371\mu_{extracted}^2 + 1.8\mu_{extracted} - 0.51, \tag{5.12}$$

$$\epsilon_x = 1.3\epsilon_{extracted} - 0.67, \tag{5.13}$$

We have performed a comprehensive numerical study to investigate the dependence of the extracted parameters on different geometrical and electrical specifications of the designed strip line fixture. Our study shows that the results of the extracted μ and ϵ are independent of each other. In other words for a specific value of permeability, by changing the permittivity the extracted value of μ dose not change and vise versa. In addition our study shows that the results of the extracted μ and ϵ are independent of the value of the consecutive parameters in the propagation direction, μ_z, and ϵz. On the other hand they are dependent to the value of the consecutive parameters of the cross section of the strip line fixture, μ_x, and ϵy, and geometrical parameters of the strip line W, h,and t. However since W, h, and t are designed properties, and $\mu_x = 1$, and $\epsilon y = \epsilon d$, all of these parameters are known and can be included in the numerical simulation to extract fitting formulas (5.12), and (5.13).

To verify the accuracy of the proposed fitting solution, we consider an anisotropic sample with the consecutive parameters shown in Fig. 5.3. The parameters shown in Fig. 5.3 are selected as μ_y, and $\epsilon x = \epsilon z$. The extracted results before and after applying the fitting formulas are shown in Figs. 5.8- 5.11, and compared with the actual data. As shown in these figures, after applying the fitting solution, the extracted parameters have acceptable agreement with the actual data.

5.4 Measurement Results

To test the accuracy of the proposed method for extracting the permeability of artificial magnetic materials, we consider the structure with fractal Hilbert3 inclusions proposed and discussed in chapter 3. One unit cell of this structure is shown in Fig. 5.12. The inclusion consists of a conducting trace having a width of $w =$ 0.11 mm and separation between traces of $s = 0.11$ mm. This artificial media was fabricated and measured using the strip line fixture method , and in this section, we compare the measurement results with numerical simulation results.

Using printed circuit technology, a strip of 2 unit cells of the fractal Hilbert3 inclusions were fabricated on an Rogers RT/duroid 5880 substrate with $\epsilon_r = 2.2$, and $tan\delta = 0.0009$ (See Fig. 5.13). A three-dimensional artificial substrate then was fabricated by stacking 33 of these strips in the y direction. Due to the thickness of the metal inclusions, and imperfection in the compressing procedure, an average air gap of 50 μm develops between the strips in the stacking process. The air space while unavoidable in the fabrication process is nevertheless measurable, so it can be easily included in the design. The fabricated artificial substrate has dimensions of 5.5, 4, and 1.1 cm in the y, z, and x directions, respectively. The strip line fixture has the dimension of l=22 cm, t=4 cm, h=11 mm, W=18 mm.

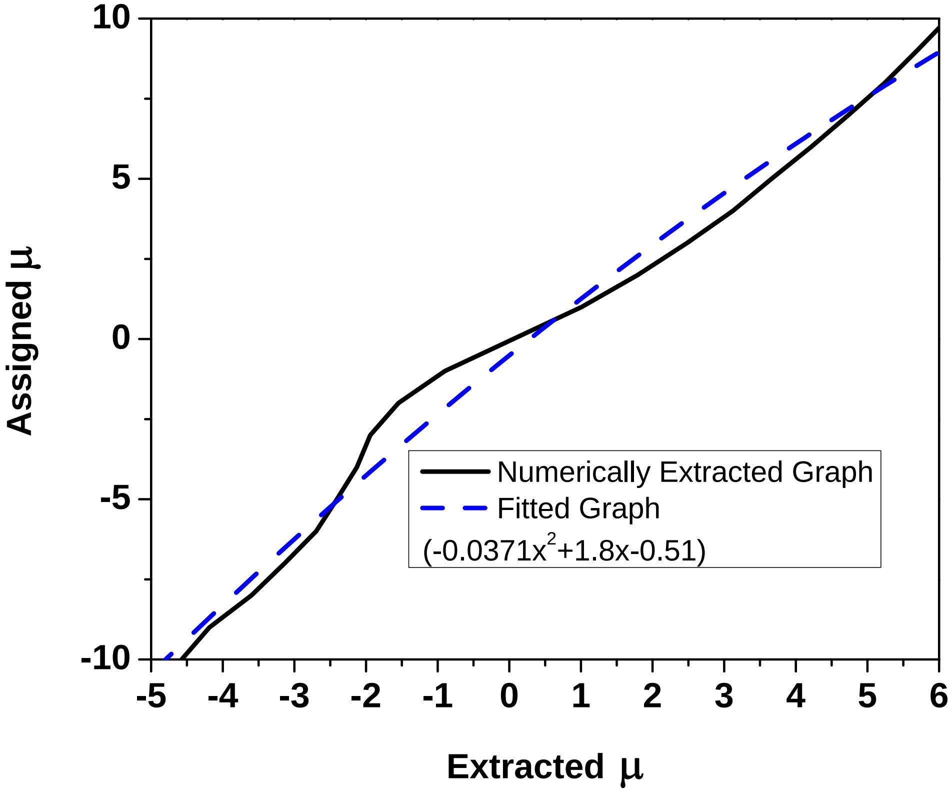

Figure 5.7: Results of simulation for anisotropic sample. Extracted permeability is plotted versus actual value of permeability.

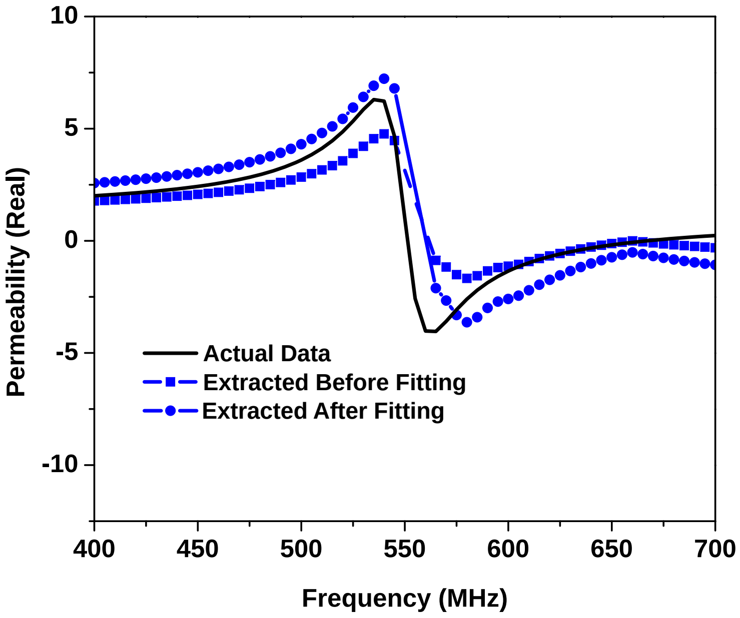

Figure 5.8: Results of simulation for anisotropic sample. Real part of extracted permeability before and after fitting is plotted and compared with the actual data.

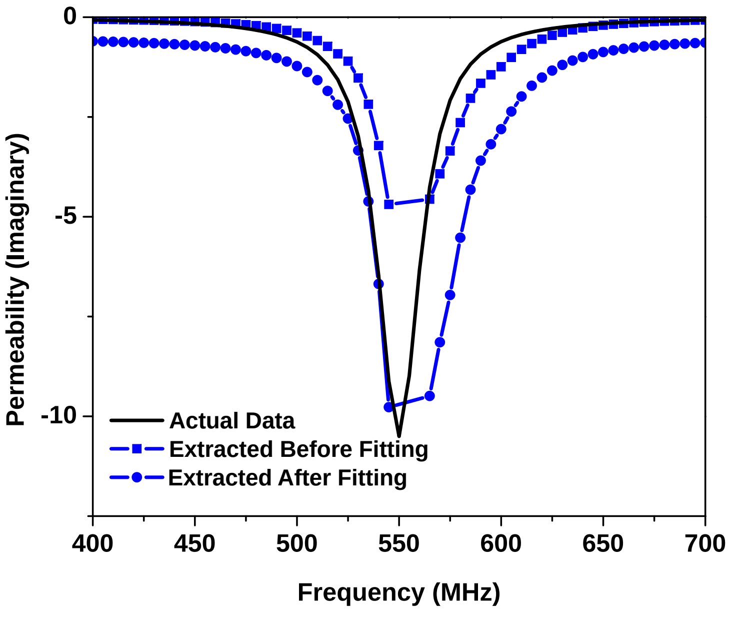

Figure 5.9: Results of simulation for anisotropic sample. Imaginary part of extracted permeability before and after fitting is plotted and compared with the actual data.

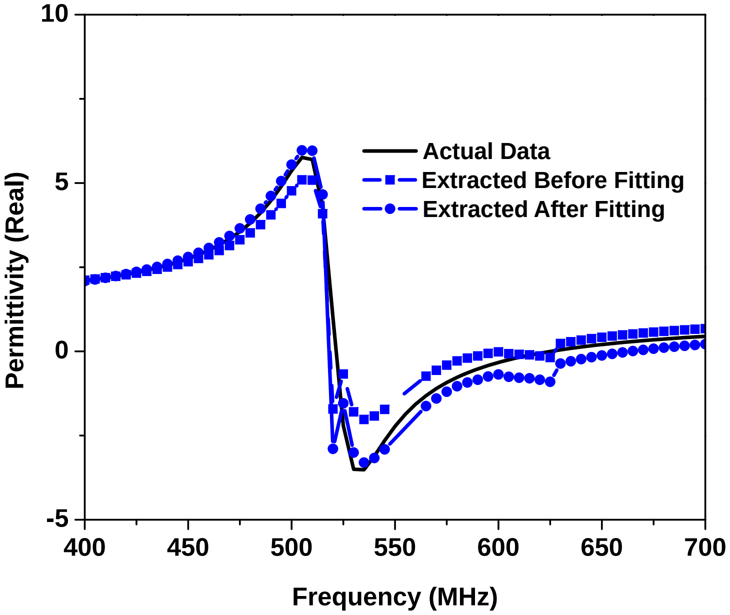

Figure 5.10: Results of simulation for anisotropic sample. Real part of extracted permittivity before and after fitting is plotted and compared with the actual data.

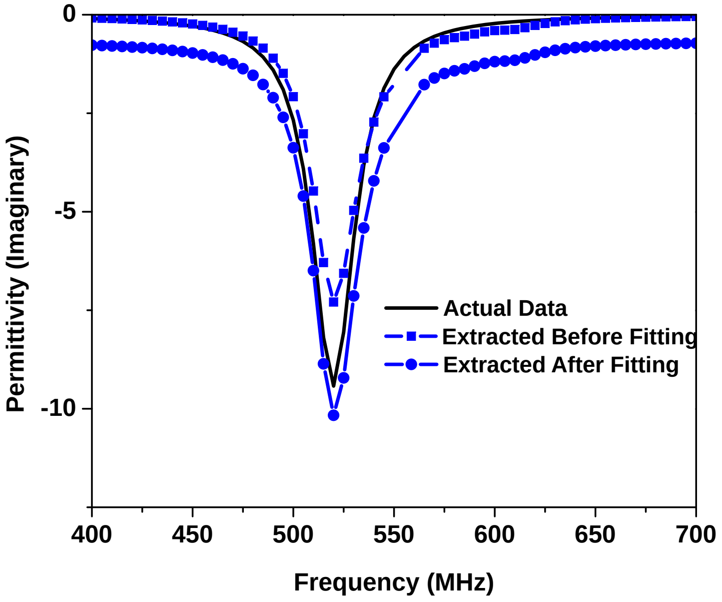

Figure 5.11: Results of simulation for anisotropic sample. Imaginary part of extracted permittivity before and after fitting is plotted and compared with the actual data.

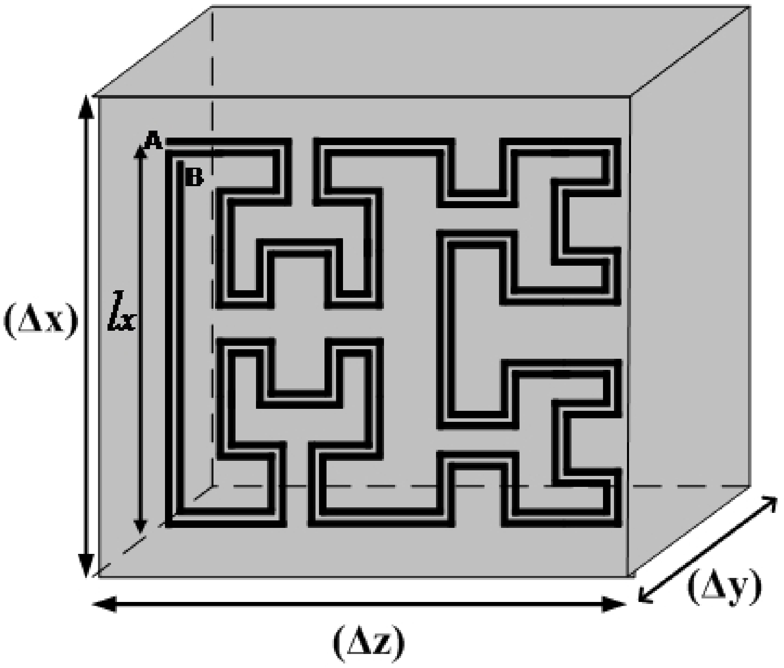

Figure 5.12: Fractal Hilbert3 inclusion used for constructing artificial magnetic material. $l_x = 8mm, \Delta y = 1.5mm, \Delta x = \Delta z = 11mm$

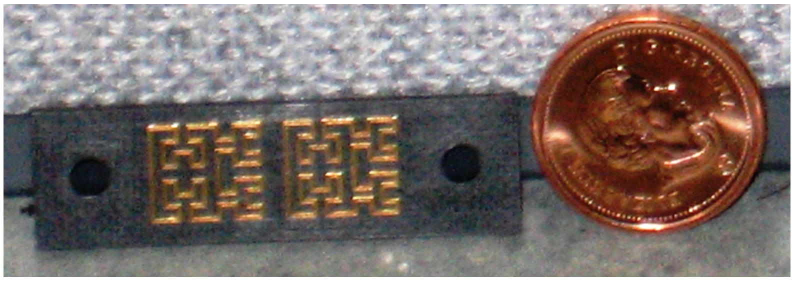

Figure 5.13: A single strip containing 2 unit cells of inclusions fabricated using printed circuit board technology.

The fabricated fixtures used for characterization of the artificial substrate are shown in Fig. 5.14 (a),(b). The fixture shown in Fig. 5.14 (a) is used to measure the properties of the strip line without the artificial sample in between. These measurements are used to determine the phase reference plane for the measurement results of the fixture with artificial sample in between. For the quasi-TEM dominant mode, the **H** and **E** fields in the substrate will be in the y and x directions, respectively. Therefore this configuration can be used for retrieval of μ_y, and ϵ_x.

Using a vector network analyzer, the S-parameters of the fixture shown in Fig. 5.14 (a), were measured. These parameters are shown in Figs. 5.15, 5.16.

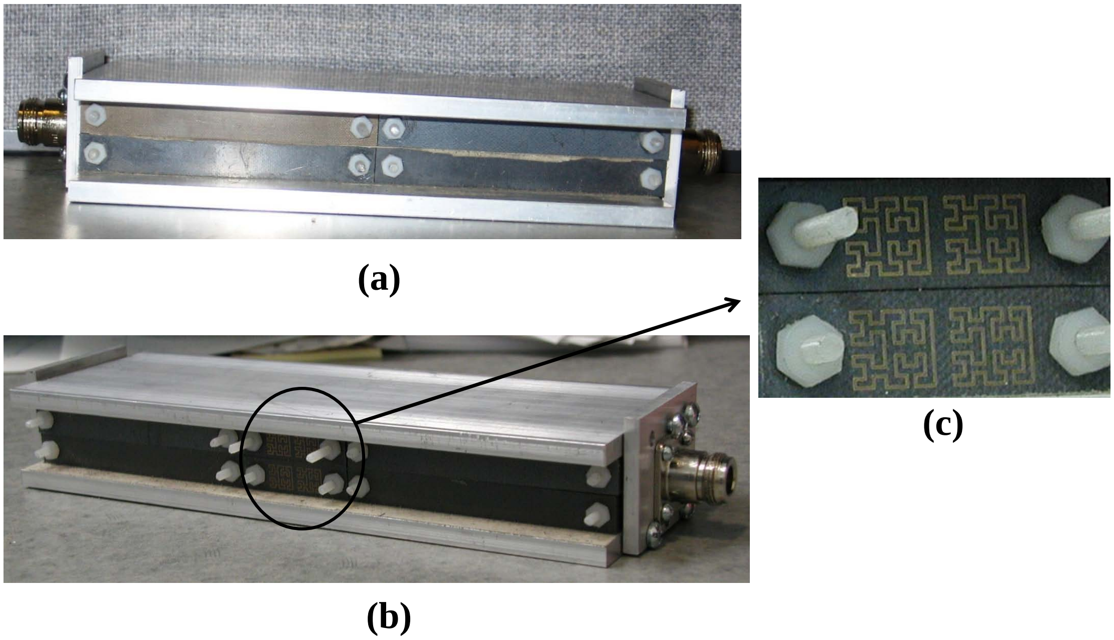

Figure 5.14: The fabricated strip line fixtures. a) without artificial sample. This fixture is measured to be used as a reference b) with artificial sample in between.

As shown in Fig. 5.15, the fabricated strip line fixture has the insertion loss of less than 0.1 dB, and return loss better than 20 dB when the artificial sample dose not exist in between. Therefore the fabricated fixture should have the accuracy needed to extract constitutive parameters of the artificial substrate. Fig. 5.16 shows the phase of the measured S21, along with the phase of a transmission line with length 20 cm. These results show that the strip line without the sample can be modeled as a transmission line with physical length of 20 cm. The actual length of the strip line fixture without sample is 18 cm. The extra phase delay could be provided by the coaxial N connectors. The phase shown in Fig. 5.16, will be used as a reference to determine the phase reference plane for the measurement results when the artificial sample exists.

Then, we have measured the S parameters of the fixture with the artificial sample in between (see Fig. 5.14 (b)). The magnitude, and phase of the measured S parameters are shown in Fig. 5.17, and Fig. 5.18 respectively.

Using the measured S parameters and the extraction method explained in section 5.2, the constitutive parameters of the artificial sample is extracted and shown in Fig. 5.19. The parameters shown in this figure, are the direct parameters extracted from measurement data without performing any fitting. In this extraction,

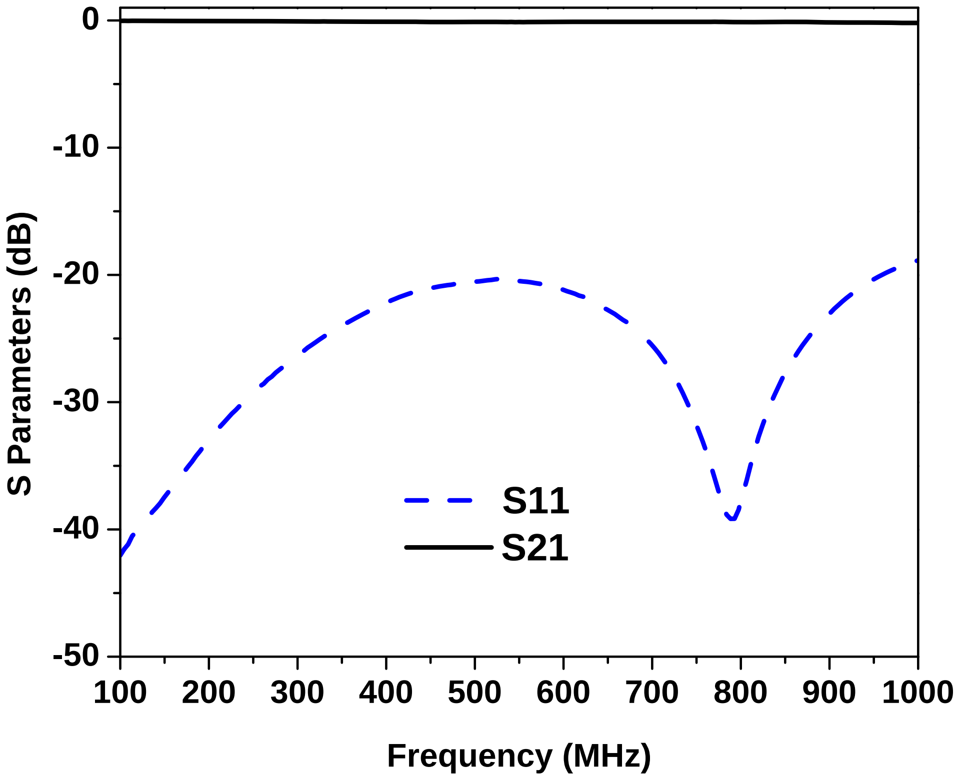

Figure 5.15: Magnitude of the measured S parameters of the reference fixture (see Fig. 5.14 (a))

the phase of the measured S21 of the reference fixture, (shown in Fig. 5.16) is deducted from the phase of the measured S11, and S21 after inserting the artificial sample(shown in Fig. 5.18). This deduction is done to eliminate the phase delay due to the two transmission lines before and after the sample.

Then we have applied the fitting formulas shown in (5.12), and (5.13) to the extracted parameters shown in Fig. 5.19, to compensate the effect of anisotropy. The results are shown in Fig. 5.20, and Fig. 5.21.

In these figures, the measurement results are compared with the numerical simulation results. The numerical results are obtained using Ansoft HFSS10, and the numerical setup explained in chapter 2. In the numerical setup, a unit cell of the artificial material combined with periodic boundary conditions are used to mimic an infinite slab of artificial materials. For numerically extraction of constitutive parameters, plane wave analysis is used, and parameters are extracted from the reflected and transmitted waves from the unit cell.The 50 μm air gap was also included in the simulation.

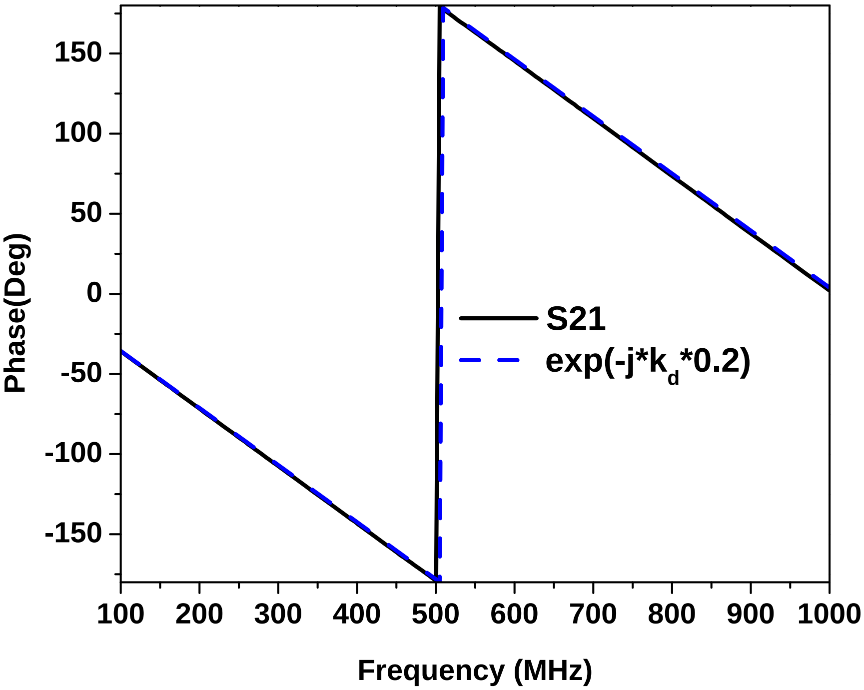

Figure 5.16: Phase of the measured S21 of the reference fixture (see Fig. 5.14 (a))

As shown in these figures, a good agreement is observed between the simulation and measurement results. It should be noted that in the numerical analysis periodic boundary conditions are used to mimic an infinite number of unit cells. However, in practice we can realize only finite number of unit cells. For example in the setup used here (see Fig. 5.13), the fabricated substrate contains 2 unit cells of inclusions in the z direction, and only one unit cell in the x direction. It can be predicted that increasing the number of unit cells provide higher homogeneity in the fabricated substrate which will result in a better agreement between numerical and measurement results.

Table 5.1 compares the accuracy of this method with several measurement methods reported in literature. As shown in this table, the method proposed here has the highest accuracy among the methods investigated in this table. In this table, the percentile difference between the measurement results and the simulation results are shown. Δf is the percentile difference in the resonance frequency, and Δa is the percentile difference in the magnitude of the extracted permeability at the resonance frequency.

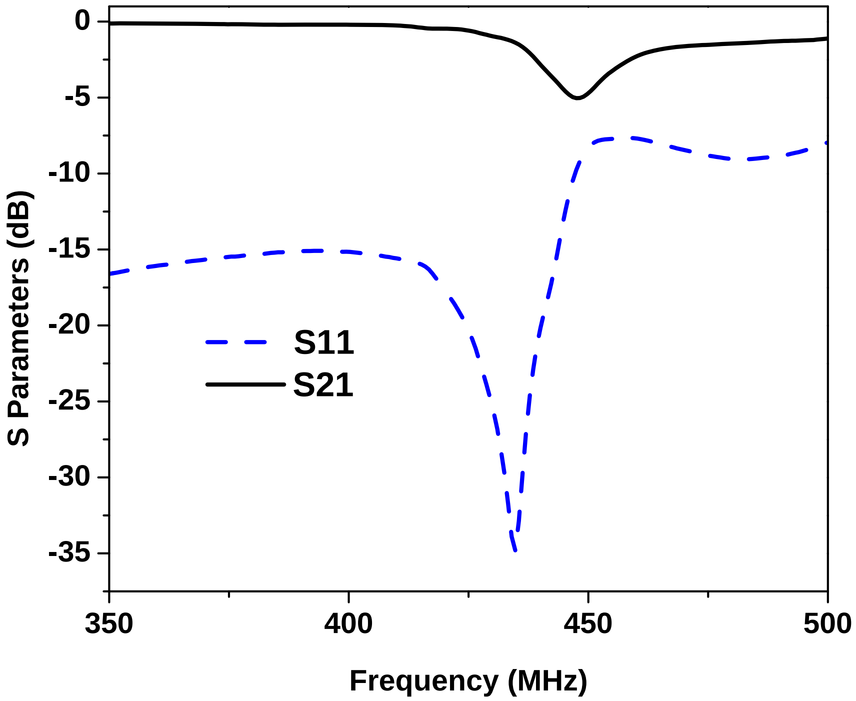

Figure 5.17: Magnitude of the measured S parameters of the fixture with artificial sample in between(see Fig. 5.14 (b))

5.5 Conclusion

A new method for metamaterial characterization was presented. The sample under test is used as the substrate of a strip line structure and the permittivity and permeability of the sample is extracted from the measured S-parameters. The method is cheap, easy to build and does not need too many samples for the operation. The method and the extraction theory was verified numerically for isotropic single and double negative materials.

The method was also applied to the anisotropic materials by employing a fitting function generated by the numerical analysis. The fitting function compensates for the anisotropy of the material. To validate the method experimentally, an anisotropic sample is designed and fabricated. The strip line structure successfully extracted the permittivity and permeability of the fabricated sample with a less then 3% shift in the resonance frequency.

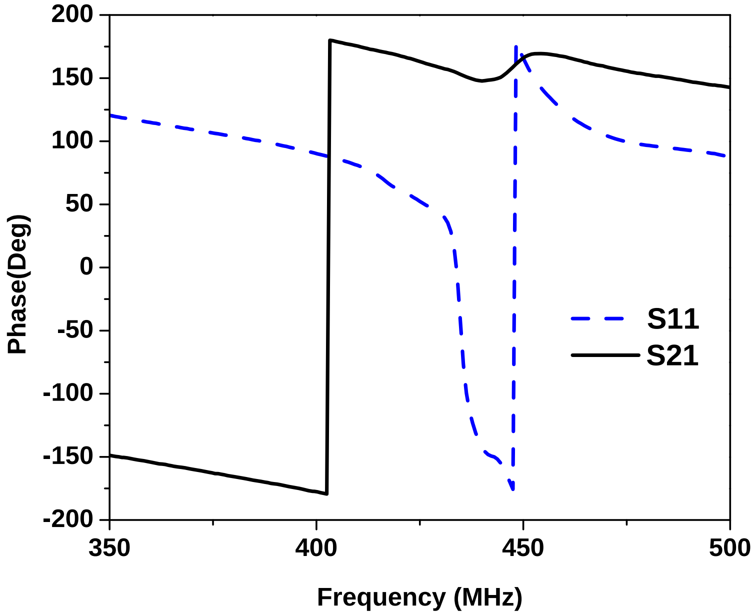

Figure 5.18: Phase of the measured S parameters of the fixture with artificial sample in between(see Fig. 5.14 (b))

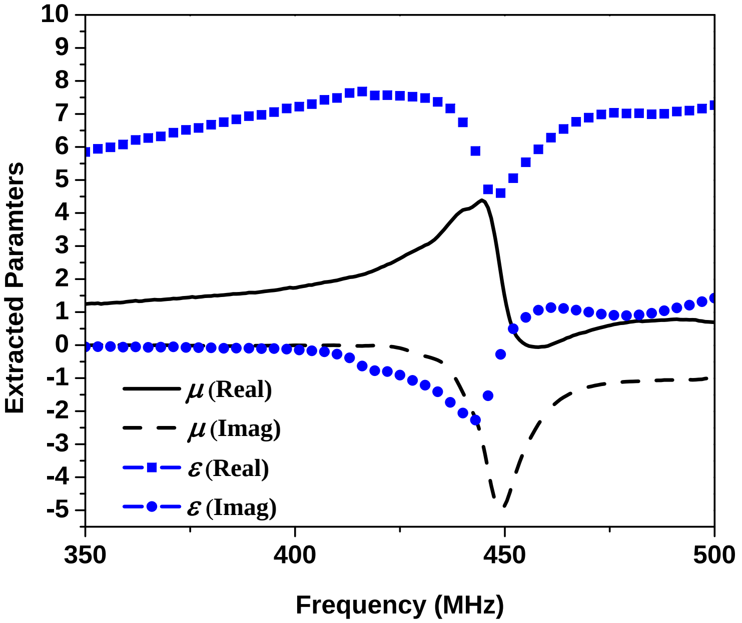

Figure 5.19: The Extracted constitutive parameters from measured S parameters. No fitting is done in this figure.

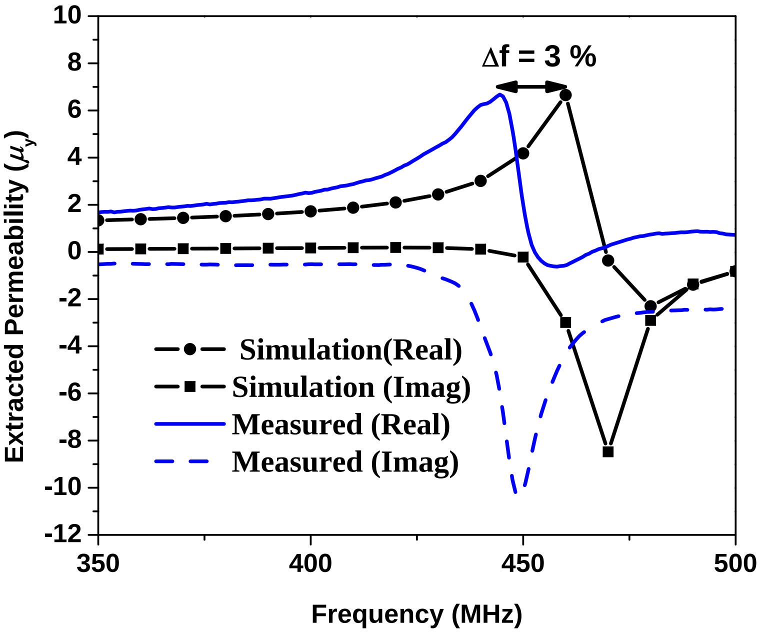

Figure 5.20: The Extracted measured permeability after fitting, using (5.12), is compared with numerical simulation results.

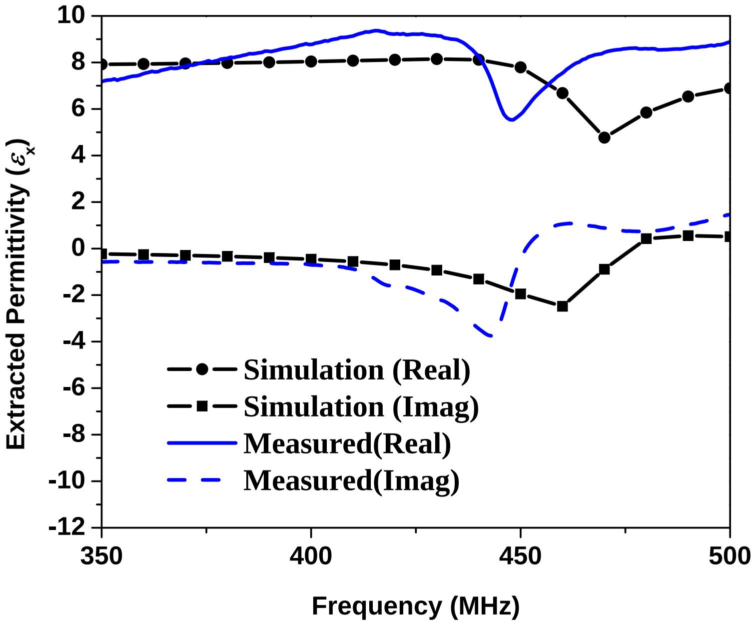

Figure 5.21: The Extracted measured permittivity after fitting, using (5.13), is compared with numerical simulation results.

Table 5.1: Comparison of the accuracy of the different measurement methods.

Measurement Method	Δf	Δa	Explanaition
This method	3%	1.49%	——
Free space Method [94]	$10\% < \Delta f < 20\%$	16%	No quantitative comparison is made in the paper. These values are approximated from Figs.
Resonance Method [95]	7.4%	measure~~ment~~ values are not reported	
[96]			No comparison is made with simulation
Wave Guide Method [97]			No quantitative comparison is made in the paper. It is hard to tell from Figs.
Free Space Method [98]			Just S11 and S21 are compared with simulation results. Effective parameters are not compared

Chapter 6

Miniaturized Antennas using Artificial Magnetic Materials

6.1 Introduction

One of the most important applications of artificial magnetic materials is implementing miniaturized planar structures, specially miniaturized microstrip antennas [1], [31], [64]—[68]. In this chapter, we investigate the performance of artificial magnets for this application.

The organization of this chapter is as follows: First in section 6.2, the advantages of using magneto-dielectric materials for miniaturization over substrates with high dielectric constant is explained through both analytical formulas and numerical simulation. Then in section 6.3, a fast numerical setup is discussed to use for simulation of miniaturized antennas with artificial magnetic materials as substrate. In section 6.4, measurement results of a fabricated miniaturized patch antenna using fractal Hilbert inclusions are reported, and compared with numerical simulation results. In section 6.5, a parametric study is done on the effect of constitutive parameters of the artificial substrate on the specifications of the resultant miniaturized antenna. In that section, the effect of the loss and dispersion of the artificial substrate on the antenna parameters such as bandwidth, gain, and efficiency is investigated. Finally, a summery and conclusion is presented in 6.6.

6.2 Miniaturized Enhanced Bandwidth Antennas

Smaller physical size, wider bandwidth, and higher efficiency are the desirable parameters for antennas in wireless communications. Considering a patch antenna as an example, the size of the patch, the same as most planar circuits, is proportional to the wavelength in the substrate which is inversely related to the wave propagation constant K:

$$K = \omega\sqrt{\mu\epsilon} = \sqrt{\mu_r\epsilon_r}K_0 \tag{6.1}$$

where ϵ_r, and μ_r are the relative permittivity and permeability of the substrate and K_0 is the free space propagation constant. Therefore, by using high dielectric material (a material with high permittivity, ϵ_r) miniaturization can simply achieved by the factor of $\sqrt{\epsilon_r}$. However, since the wave impedance, Z is proportional to the ratio of μ_r and ϵ_r:

$$Z = \sqrt{\frac{\mu}{\epsilon}} = \sqrt{\frac{\mu_r}{\epsilon_r}}Z_0 \tag{6.2}$$

In this case there will be a high impedance mismatch between the air and the substrate. Due to this mismatch, as shown in [29], [99], [100], most of the energy will be trapped in the substrate leading to narrow bandwidth and low efficiency. To solve this problem, instead of using high dielectric material (only $\epsilon_r > 1$), one can use a substrate with magneto-dielectric material (both $\epsilon_r > 1$, and $\mu_r > 1$). In this case, by choosing moderate values for ϵ_r, and μ_r , a high miniaturization factor ($\sqrt{\epsilon_r\mu_r}$) can be achieved while keeping the wave impedance close to that of air leading to the less mismatch. In [32], for the first time, a probe fed patch antenna placed over a magneto-dielectric material was investigated and using a transmission line model, the parameters of the antenna were analytically calculated. It was shown in [32] that the impedance bandwidth of a probe fed patch antenna over a magneto-dielectric with thickness h is expressed as:

$$BW = \frac{96\sqrt{\frac{\mu_r}{\epsilon_r}}h}{\sqrt{2}(4 + 17\sqrt{\epsilon_r\mu_r})\lambda_0} \tag{6.3}$$

Therefore for a specific miniaturization factor, $\sqrt{\epsilon_r\mu_r}$, as the μ_r increases, the bandwidth increases as well. To verify this idea numerically, we have designed a miniaturized patch antenna using magneto-dielectric materials and compared with another miniaturized antenna using high dielectric substrate. The structure of the antenna is shown in Fig. 6.1. To achieve an antenna with the size of $\lambda/14$, a miniaturization factor equal to $\sqrt{\epsilon_r \mu_r} = 7$, is needed. For magneto-dielectric case, a substrate with $\epsilon_r = \mu_r = 7$ is chosen, and for high permittivity dielectric case a material with $\mu_r = 1$ and $\epsilon_r = 49$ is selected. The loss of the material is chosen to be the same for both cases and is equal to $tan\delta e = tan\delta m = 0.01$. The other parameters of the antenna shown in Fig. 6.1 are the same for both cases and are equal to: $a = b = 59.4mm$, $h = 5mm$, $X_0 = 0$, and $Y_0 = 23.7mm$ for magnetic material case and $Y_0 = 21.7mm$ for high dielectric case. Different values for parameter Y_0 is chosen for two cases to achieve well-matched probe feeding for both cases. The simulation results of these two antennas are illustrated and compared in Fig. 6.2. This simulation is performed by using Ansoft HFSS.

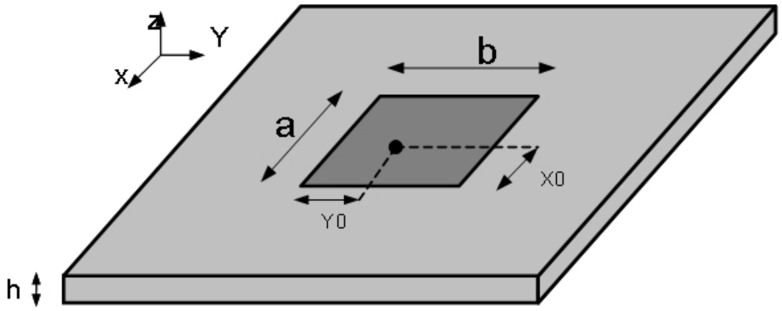

Figure 6.1: The structure of the probe-fed patch antenna.

The simulation results in Fig. 6.2 shows that the antenna on magneto-dielectric substrate has a bandwidth ($S11 < -10dB$) of 2.5%, while this value for the antenna on high dielectric is only 0.28%. Therefore by using magneto-dielectric material, for the same miniaturization factor, the bandwidth is increased by approximately one order of magnitude. The numerical simulation results show an efficiency of 75% for the antenna on magneto-dielectric substrate and 40% for the antenna on high dielectric substrate. Since all the dielectric and ohmic losses are assumed to be the same for both cases, the difference in efficiency is related to wave impedance mismatch in high dielectric substrate which does not exist in the magneto-dielectric substrate. Therefore, based on the preliminary numerical analysis conducted here, we conclude that using magneto-dielectric materials as substrate results in wider bandwidth and higher efficiency.

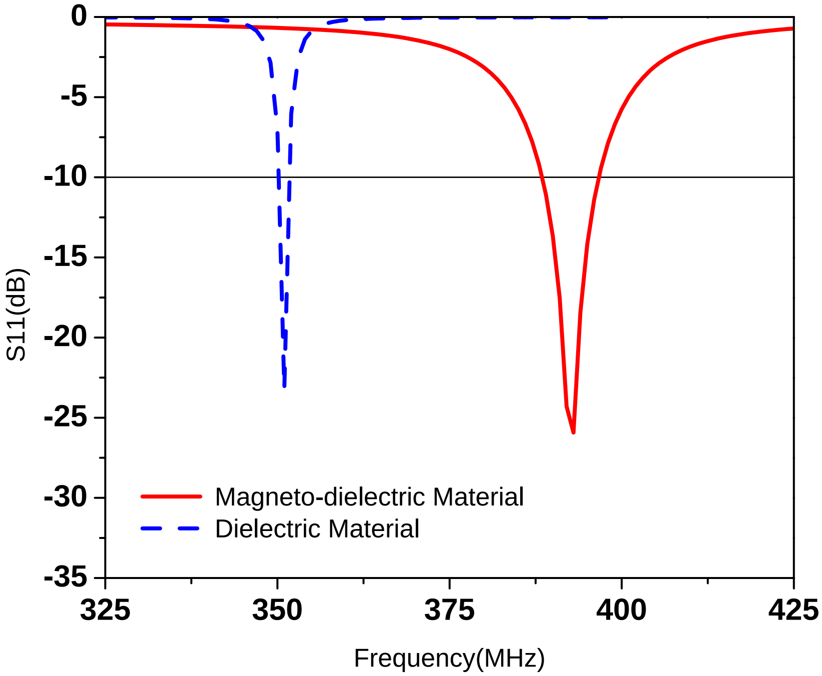

Figure 6.2: The return loss of the miniaturized antenna using magneto-dielectric material ($\epsilon_r = \mu_r = 7$) is compared with the case of using dielectric with high permittivity ($\epsilon_r = 49$).

6.3 Numerical Analysis

Fig. 6.3, shows a patch antenna constructed over an artificial substrate. To numerically simulate the structure of Fig. 6.3, due to the high aspect ratio between the antenna and inclusion dimensions, huge numbers of meshes is needed leading to a time consuming and practically inefficient simulation. Therefore, we have done an alternative simulation in which the engineered substrate is substituted by a homogeneous but anisotropic material with effective permittivity and permeability extracted for engineered substrate using plane wave analysis. The alternative structure is shown in Fig. 6.4.

In the next section, measurement results are used to investigate the accuracy level of this simulation.

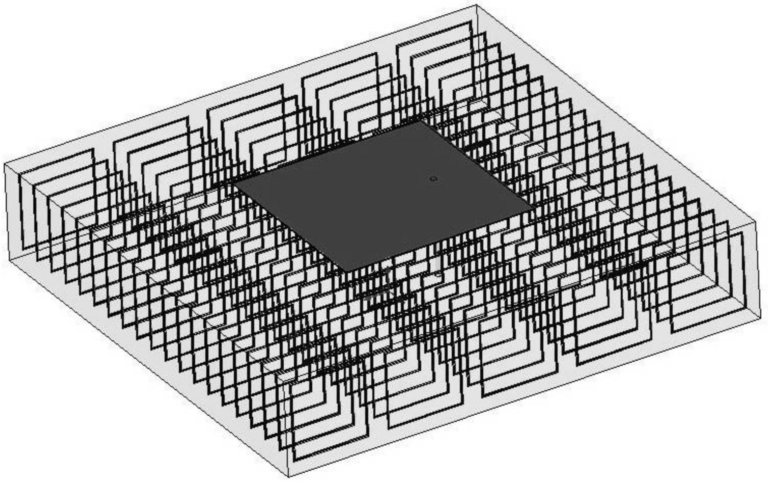

Figure 6.3: Coaxial probe feed Patch Antenna radiating over an engineered substrate.

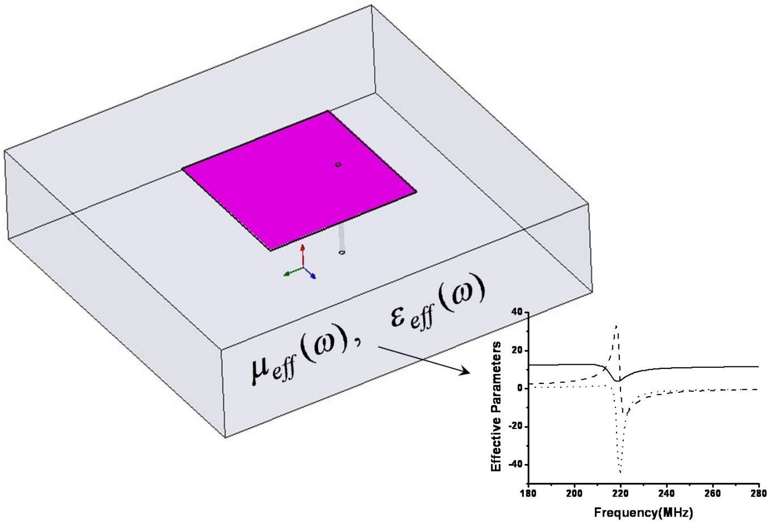

Figure 6.4: The alternative choice for structure of Fig. 6.3, which is used for simulation. The engineered material is modeled as a homogenous substrate with effective parameters

6.4 Measurement Results

In this section a miniaturized patch antenna is designed, and fabricated to radiate over the artificial structures containing 2nd order fractal Hilbert inclusions. The same substrate fabricated for permeability extraction in chapter 4 (see Fig. 4.5), is used for antenna implementation as well (see Fig. 6.5). This is one of the most important advantages of the extraction method explained in chapter 4, in which no sample preparation is required, and the same substrate used for implementation of planar structures can be used for permeability extraction as well.

The miniaturized antenna is designed to operate at the frequency of 615 MHz. According to the measurement results reported in section 4.3 (see Fig. 4.7), the fabricated artificial substrate results in an effective permeability of $\mu_r = 3.2$, and effective permittivity of $\epsilon_r = 9.58$ at the frequency of 615 MHz. According to these values for permittivity, and permeability a coaxial-fed square patch antenna is designed, and fabricated to radiate over the artificial substrate. The fabricated antenna, and its dimensions are shown in 6.5. According to these dimensions, the size of antenna in the y direction is equal to $b = 4.2cm$ which is 1/11.6 of the wavelength at the resonance frequency of 615 MHz. Therefore a miniaturization factor of 5.8 is achieved using artificial magnetic substrate. The ground plane is designed to be big enough to avoid restriction of the gain due to the finite size of the ground plane.

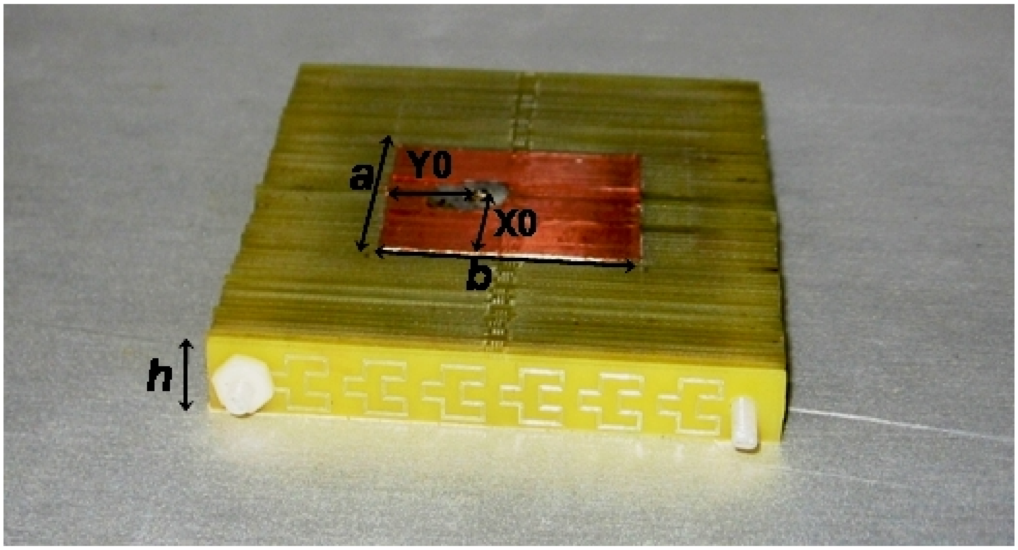

Figure 6.5: The fabricated miniaturized antenna, a=3.3 cm , b=4.2 cm , X0 =1.7 cm , Y0 =1.4 cm.

The measured return loss is shown in Fig. 6.6, and compared with the simulation results using the method explained in section 6.3. As shown in this figure, a strong agreement is observed between simulation and measurement results. Therefore using a substrate with effective parameters instead of using the actual artificial substrate in the numerical simulation is accurate enough for design purposes.

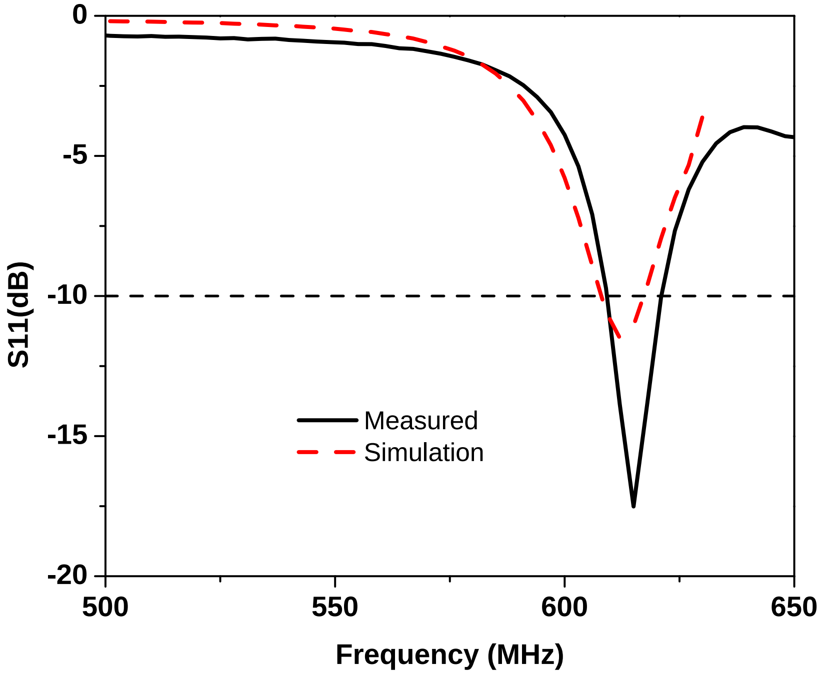

Figure 6.6: The measured return loss of the miniaturized antenna.

According to the measurement results shown in Fig. 6.6, the miniaturized antenna has a bandwidth ($S11 < -10dB$) of 2.11%, which is much wider when compared to the pervious works [1],[64]–[68] done on miniaturized antennas using artificial magnetic materials, e.g. reported bandwidth in [1] is 0.83 %.

The measured pattern is shown in Fig. 6.7. According to these results, the miniaturized antenna has a gain of -3.4 dBi at the boresight with the front-to-back ratio of 12.5 dB. The measured gain is comparable with the similar miniaturized antennas in the pervious works [1],[64]–[68], e.g. reported boresight gain in [1] is -3.9 dBi

6.5 Parametric Study

In this section, we perform a numerical study to investigate the effect of different parameters of the artificial substrate on the antenna specifications. First the effect of the loss of substrate on the gain and efficiency of the antenna, and then the effect of the dispersion of the substrate on the bandwidth of the antenna are investigated.

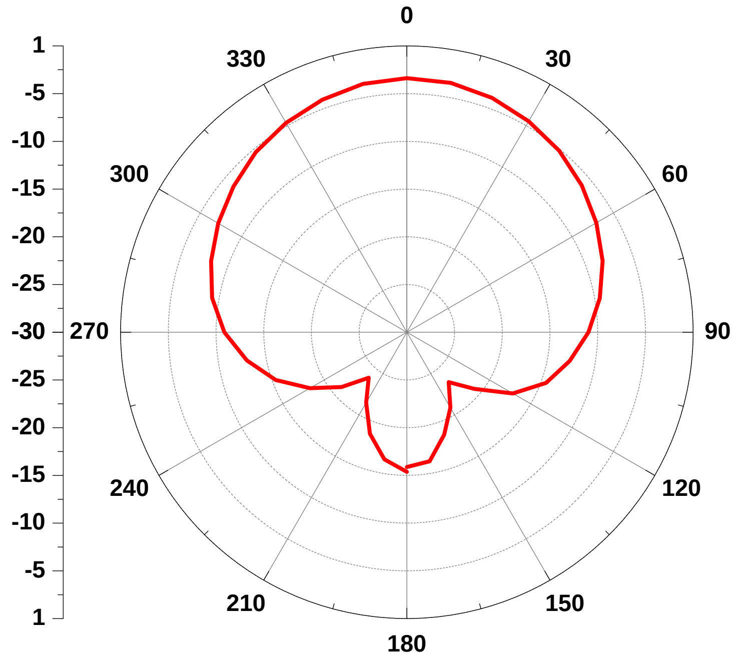

Figure 6.7: The measured Pattern of the miniaturized antenna is compared with simulation results.

6.5.1 Lossy Substrate

When artificial magnetic substrates are designed to provide effective permeability higher than one, the resultant permeability would be a complex number with both real and imaginary parts. The imaginary part of the effective permeability will results in magnetic loss tangent. In this section, we investigate how this magnetic loss affects the gain and efficiency of the miniaturized antenna designed to radiate over the artificial substrate.

Figs. 6.8, 6.9 show the gain, and efficiency of a coaxial-fed patch antenna versus magnetic loss tangent of the artificial substrate. The results illustrated in these figures are numerical results achieved from simulation of a patch antenna radiating over a magnetic substrate with $\epsilon_r = 9.6$, $\mu_r = 3.3$, and thickness of $h = 11mm$(see Fig. 6.4). Dielectric loss tangent of the substrate is assumed to be zero to avoid the interference of both losses in the resultant gain and efficiency. The size of the patch antenna in this simulation is 4.7 x 3.3 cm. The results are generated using Ansoft HFSS 10 software.

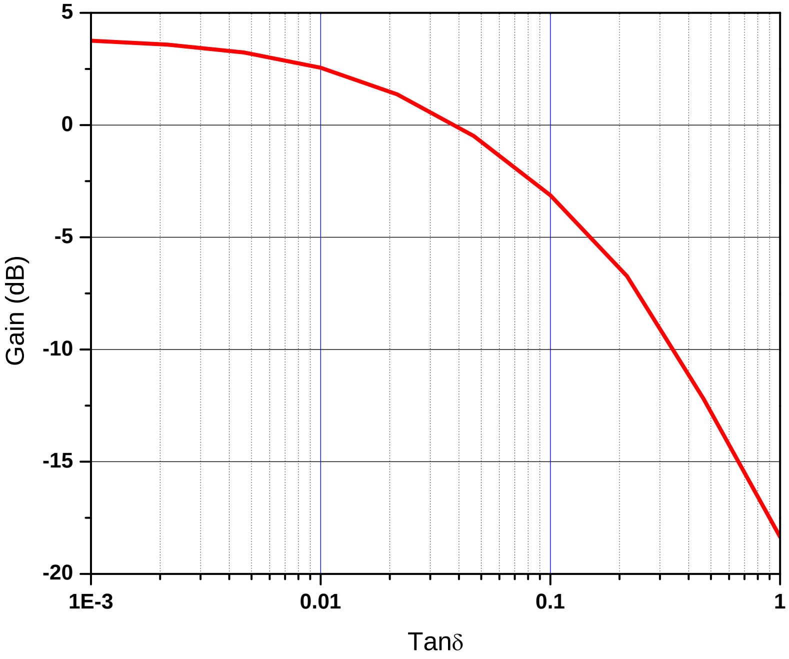

Figure 6.8: The Gain of the miniaturized antenna versus magnetic loss tangent (numerical results).

According to the results shown in Figs. 6.8, and 6.9, if $tan\delta < 0.04$, the gain will be more than 0dB, and efficiency will be more than 40%.

6.5.2 Dispersive Substrate

As observed in previous chapters, the resultant permeability of artificial structures varies by frequency thus resulting in a dispersive medium. This variations can affect the frequency bandwidth of the planar antennas radiating over these substrate. In this section, we investigate the effect of dispersion over the antenna bandwidth.

To get a feeling that how this dispersion affects the bandwidth, we compare the response of an antenna radiating over an artificial substrate containing spiral inclusions with the case of using a magnetic material with frequency independent parameters as the substrate. The result of this simulation is shown in Fig. 6.10 . The artificial substrate in this simulation, has the response shown in Fig. 2.20, and the frequency-independent material is chosen to have permeability and permittivity equal to that of the engineered material at the frequency of 200MHz: $\mu_r = 3.1$,

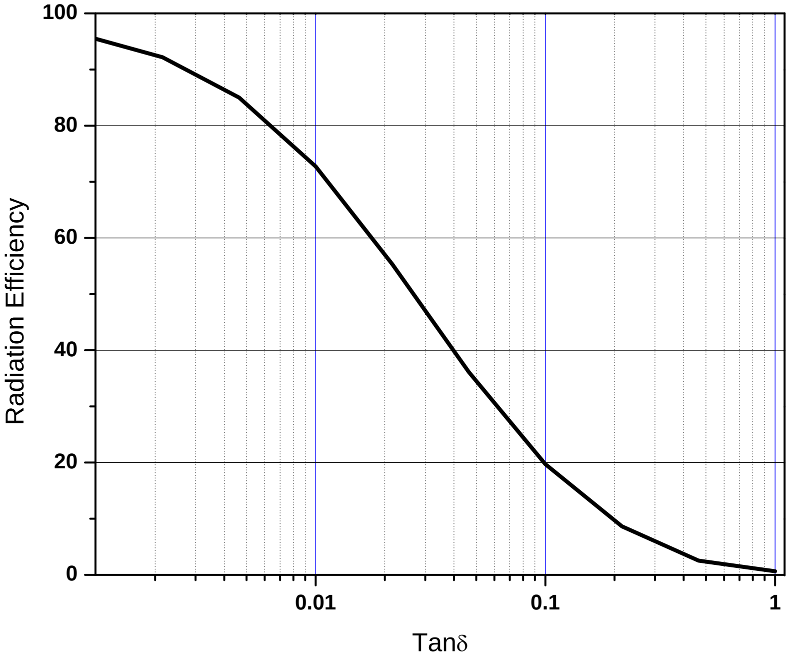

Figure 6.9: The Efficiency of the miniaturized antenna versus magnetic loss tangent (numerical results).

$\epsilon_r = 12.4$, $magnetictan\delta = 0.014$. The miniaturized antenna is a square patch with width of 12.7cm ($\lambda/12$ at the resonance frequency) for both cases of dispersion free material and artificial magnetic material.

As shown in Fig. 6.10, the miniaturized antenna over the dispersion-free magnetic material has a bandwidth ($S11 < -10dB$) of 7.5% , while the bandwidth of the miniaturized antenna over the artificial magnetic materials is limited to 1%. The same bandwidth limitation is reported in [1] for the same artificial magnetic material using measurement results. Therefore, highly dispersive artificial magnetic materials can reduce the antenna bandwidth dramatically.

To investigate more about the effect of dispersion on the antenna bandwidth, we simulate an antenna with the permeability of substrate as lines show in Fig. 6.11. The other physical, and electrical properties of the antenna is as the same as properties used for simulation of Fig. 6.10. The slope of the lines in Fig. 6.11 illustrates the dispersion of the substrate. As the line slope increases, the dispersion of the substrate increases. The results of these simulations is shown in Fig. 6.12.

According to these results, the bandwidth of the antenna ($S11 < -10dB$) de-

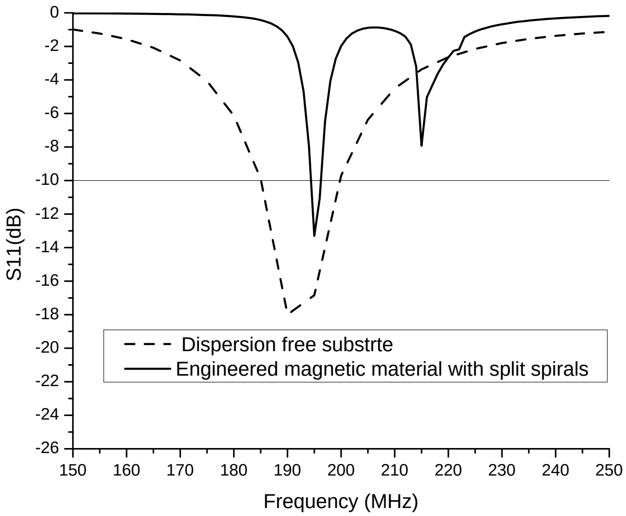

Figure 6.10: The simulation results of an antenna with dispersive substrate is compared with the case of using dispersion-free substrate.

creases as the dispersion of the substrate increases. The results of Fig. 6.12 shows that bandwidth reduces from 7.5% for the non-dispersive substrate (Disp1 in Fig. 6.12)to 1.05% for the substrate with dispersion of 0.24 per MHz (Disp6 in Fig. 6.12).

6.6 Conclusion

The performance of the artificial magnetic materials for the application of the miniaturized antenna was investigated. In this investigation, a fast numerical setup was used in which the artificial substrate was substituted with a homogenous substrate with effective constitutive parameters of the artificial structure. The accuracy of the simulation setup was validated through comparison with measurement results.

In the measurement results, a miniaturized patch antenna was fabricated to radiate over the artificial substrate of the 2nd order fractal Hilbert inclusions. It was shown that using Hilbert inclusions, a miniaturized factor of 5.8 can be achieved for patch antennas. The return loss, and the radiation pattern of the miniaturized antenna were measured, and reported. Measurement results exhibit 2.11 % bandwidth and -3.4 dBi gain for the miniaturized antenna. Using the mentioned simulation setup, a parametric study was done on the effect of constitutive param-

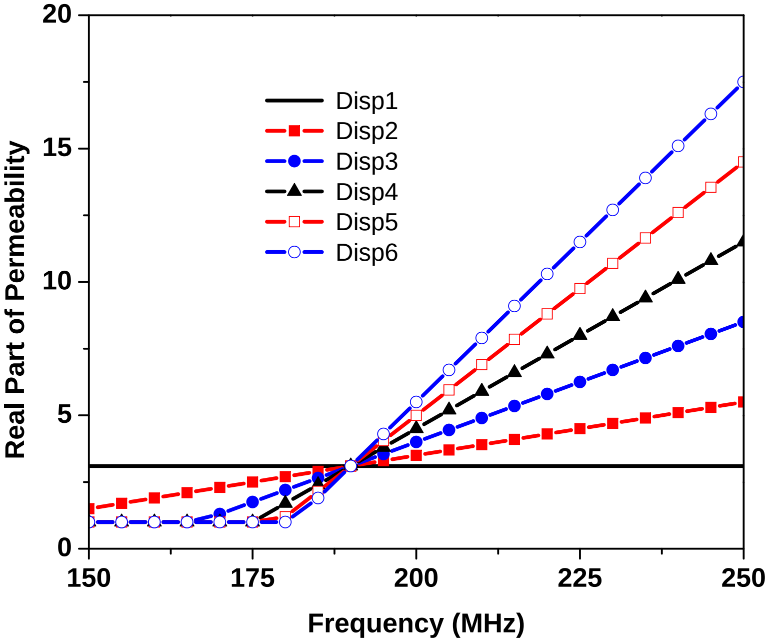

Figure 6.11: Real part of permeability with different dispersion. The dispersion varies as the slope of the line varies.

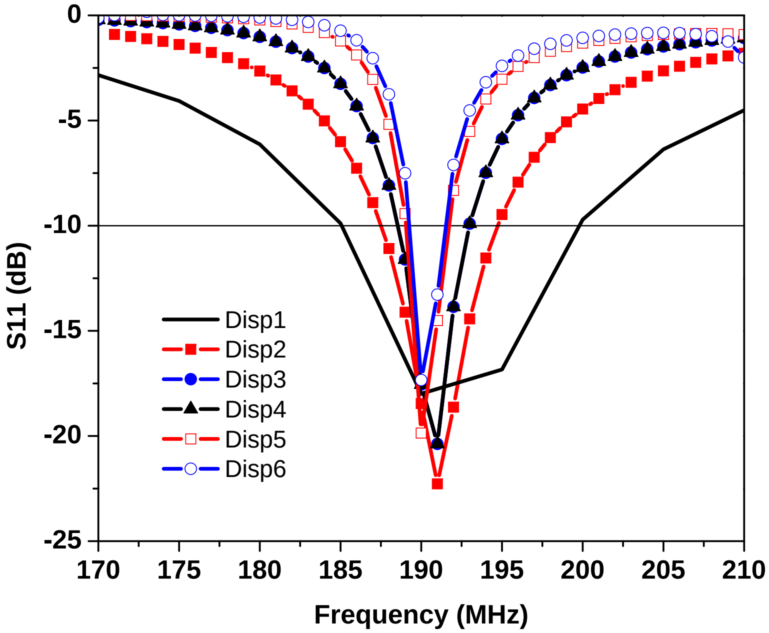

Figure 6.12: The return loss of the miniaturized antenna on substrates with permeability shown in Fig. 6.11.

eters of the artificial substrate on the specifications of the resultant miniaturized antenna. In that study, the effect of the magnetic loss tangent on the gain and efficiency of the antenna, and also the effect of the dispersion of the substrate on the bandwidth of the antenna were investigated. The results of this study shows that to achieve a miniaturized antenna with the gain more than 0dB, and efficiency more than 40%, magnetic loss tangent of the substrate should be less than $tan\delta < 0.04$. Furthermore, this study shows that the bandwidth of antenna is reduced from 7.5% for the non-dispersive substrate to 1.05% for the substrate with dispersion of 0.24 per MHz.

Chapter 7

Artificial Magnetic Materials with Multi-Resonator Unit Cells

7.1 Introduction

In this chapter,the multi-resonator structures are proposed as building blocks for artificial magnetic materials. The idea of multi-resonator structures is to use several metallic inclusions with different dimensions in a unit cell. The metallic inclusions are designed to have different resonance frequencies. These resonances can be adjusted either far away from each other, to provide multi-band artificial structures, or very close to each other to provide wide band artificial materials.

The organization of this chapter is as follows: First in section 7.2, the idea of multi-resonator structures are introduced, and investigated through numerical full wave simulation. Then in section 7.3, circuit models are proposed to model multi-resonator structures. Section 7.4, optimizes the multi-resonator to increase the frequency bandwidth in which the artificial structure illustrates magnetic properties. This optimization is done using first circuit models, and then space mapping technique [101]–[108]which connects circuit models to numerical full wave results. Finally, a summery and conclusion is presented in 7.6.

7.2 Unit Cells with Multiple Inclusions

Fig. 7.1 illustrates a unit cell with two inclusions. Inclusions are circular SRRs with different dimensions resulting in two distinguished resonance frequencies. In this section, using full wave simulation, we investigate the resultant permeability of this unit cell, and compare the results with the resultant permeability of each inclusions. Using full wave simulation, and setup explained in chapter 2, the resultant

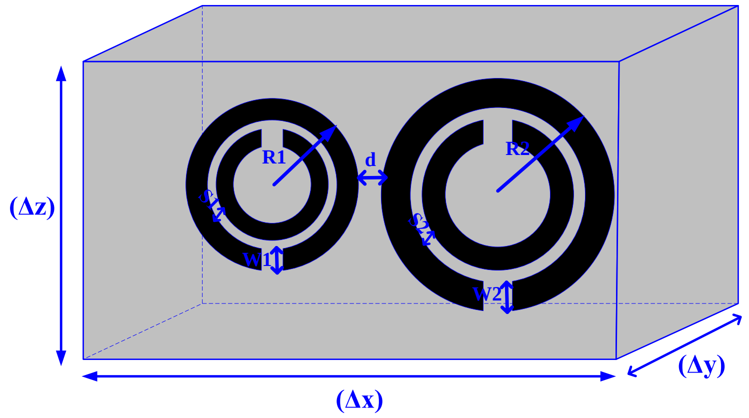

Figure 7.1: A unit cell with two inclusions.

permeability of the configuration shown in Fig. 7.1 is extracted, and illustrated in Figs. 7.2, 7.3. In this Figures, the resultant permeability of multiple inclusions, is compared with the resultant permeability of each inclusion when another one dose not exist. The geometric, and electrical specifications used in this simulation are as follows:$R_1 = R_2 = 2.6mm, S_1 = S_2 = 0.2mm, W_1 = 0.3mm, W_2 = 0.7mm, tan\delta = 0.01, \epsilon_r = 2.43, \Delta_y = 4mm, \Delta_x = 14mm, \Delta_z = 7mm$

As shown in Figs. 7.2, 7.3 , when two inclusions are used in the unit cell, two resonance frequencies are observed in the resultant permeability. Furthermore, the results of these figures show that the resonance frequencies of combination of two inclusions are very close to resonance frequencies of each resonator. The small shift between resonance frequencies can be due to the electric coupling between resonators, which is caused by finite value of d. It is expected that by incensement of d, this coupling effect, and the resultant frequency shift will be decreased. According to these results, by using multiple inclusions in one unit cell, the electromagnetic properties of the structure can be extended to multiple frequency bands. This can extend the use of these materials for multi-band applications.

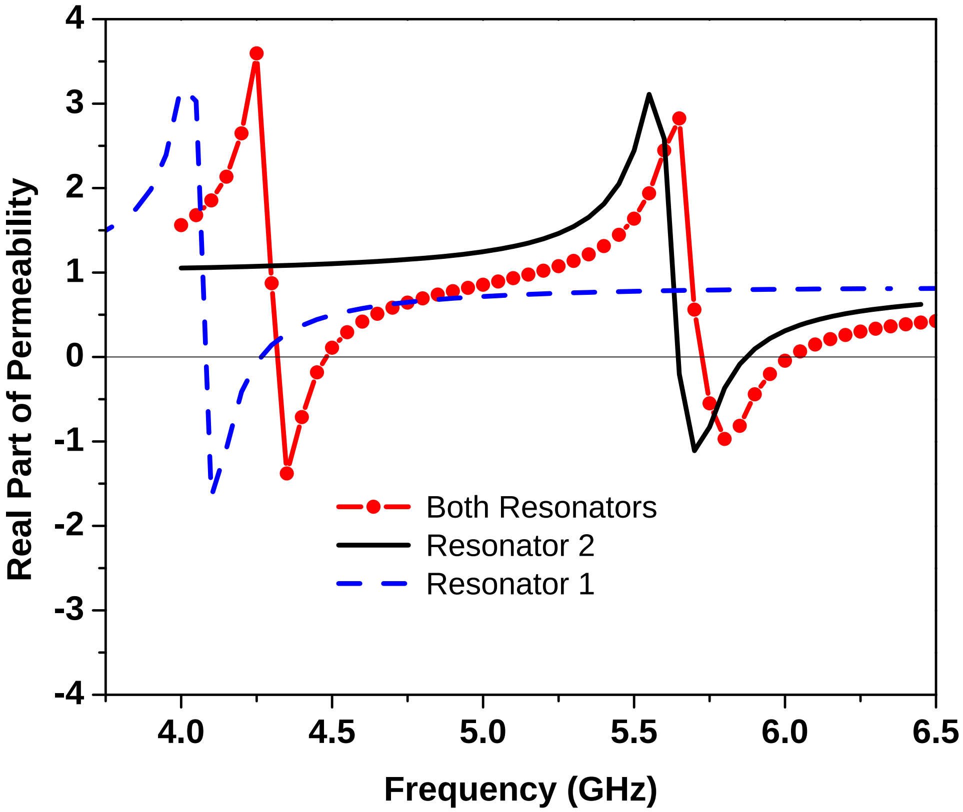

Figure 7.2: Real part of resultant permeability of configuration of Fig. 7.1 is compared with that of each resonator when the other one dose not exist.

7.3 Developing Analytical Formulas for Multi-Resonator Configurations

Considering the configuration of Fig. 7.1, the magnetic flux produced by one resonator dose not cross another one, so they don't have magnetic coupling, and the space between resonators d can be designed such that the electric coupling will be negligible. Since the resonators have small coupling with each other, their induced currents can be formulated independently using the relationship in (2.15) for each one:

$$I_1 = \frac{-j\omega\mu_0 S_1}{(R_1 + \frac{1}{G_1+jwC_1} + j\omega L_1)} H_{ext} \tag{7.1}$$

$$I_2 = \frac{-j\omega\mu_0 S_2}{(R_2 + \frac{1}{G_2+jwC_2} + j\omega L_2)} H_{ext} \tag{7.2}$$

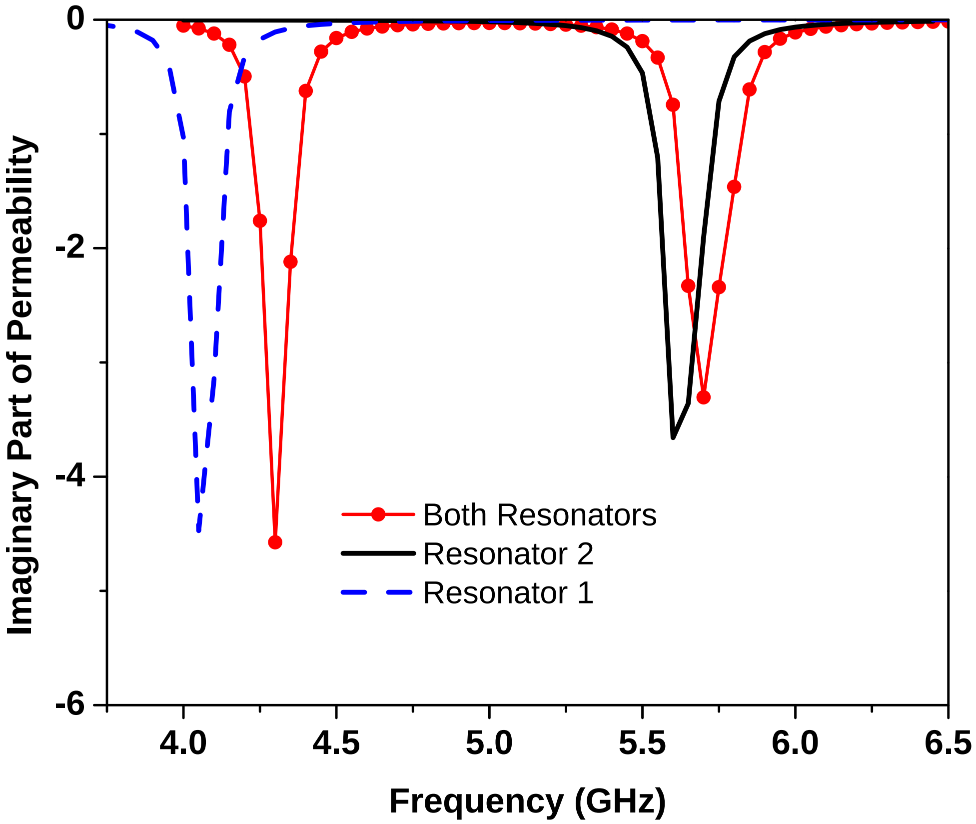

Figure 7.3: Imaginary part of resultant permeability of configuration of Fig. 7.1 is compared with that of each resonator when the other one dose not exist.

In (7.1) and (7.2), effective indexes are omitted for brevity. Magnetic polarization M, and relative permeability, μ_r would be:

$$M = \frac{S_1 I_1 + S_2 I_2}{\Delta x \Delta y \Delta z} \tag{7.3}$$

$$\mu_r = 1 + K_1 \frac{j\omega L_1}{R_1 + \frac{1}{G_1 + jwC_1} + j\omega L_1} + K_2 \frac{j\omega L_2}{R_2 + \frac{1}{G_2 + jwC_2} + j\omega L_2} \tag{7.4}$$

where:

$$K_i = \frac{-S_i}{\Delta x \Delta z}, i = 1, 2 \tag{7.5}$$

The results in (7.4) can be easily extended to the case of multi-resonator structures with more than two resonators:

$$\mu_r = 1 + \sum_{i=1}^{n} K_i \frac{j\omega L_i}{R_i + \frac{1}{G_i + jwC_i} + j\omega L_i} \tag{7.6}$$

Where n is the number of resonators in the unit cell. The results in (7.6), can be illustrated as the output of a circuit model. Fig. 7.4 illustrates this circuit for a unit cell with four resonators.

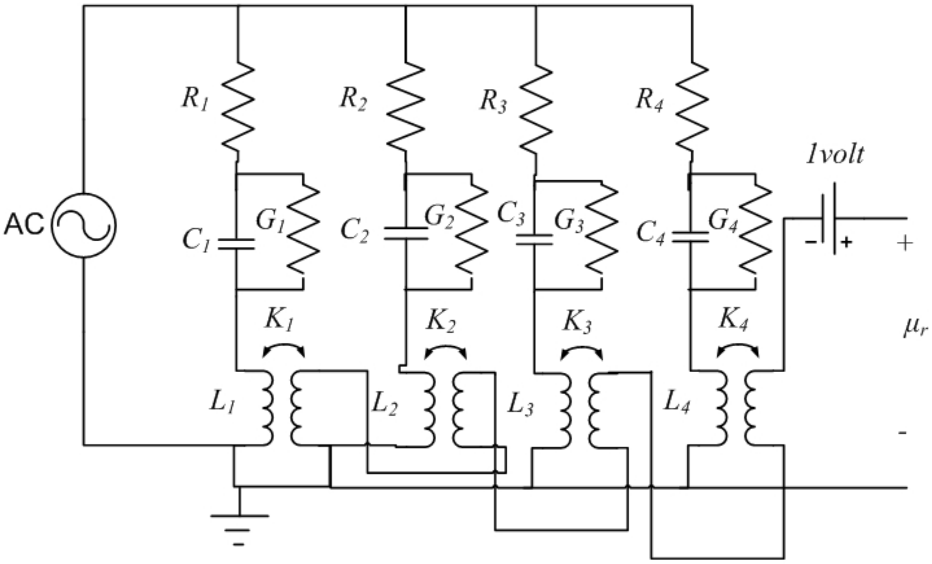

Figure 7.4: Circuit model for a unit cell with four resonators.

Fig. 7.5 shows analytical, and simulation results for the structure of Fig. 7.1. The considerable difference between analytical and simulation results, can be due to the coupling effect between two resonators which is not modeled in the circuit model.

7.4 Optimized Multi-Resonator Configurations

In this section, we try to optimize multi-resonator configurations for a desirable permeability response. In this optimization, by adjusting the resonance frequencies very close to each other, we try to provide wide band artificial materials. This idea is similar to combining narrow band filters to develop a filter with wider bandwidth in filter design [109]. In the following subsections, we investigate this idea first analytically and then numerically. The idea is applied to both fractal inclusions, and SRR inclusions.

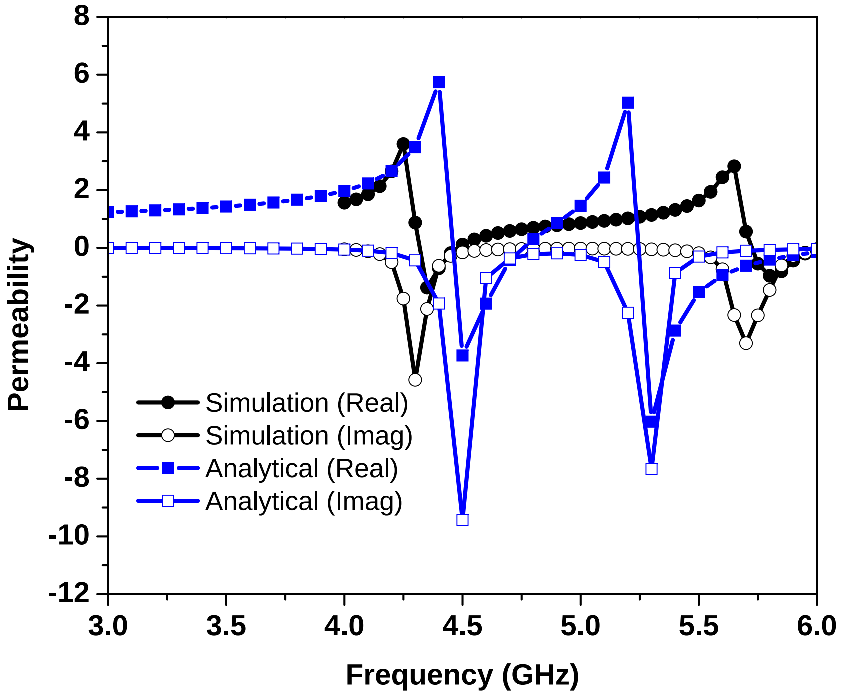

Figure 7.5: Numerical, and analytical results for the structure of Fig. 7.1.

7.4.1 Analytically Optimized Unit Cell with 4 Fractal Inclusions

In this optimization, the configuration of 3rd order Hilbert is chosen for each resonator (see Fig. 7.6). The l_z ,W,and s, (the dimension of the inclusion in the z direction, width of metal strips, and space between them) for each resonator are selected as optimization variables. In this optimization, we use the circuit model shown in Fig. 7.4, and genetic algorithm. The circuit parameters , R_i, C_i, L_i, G_i are calculated using equations presented in chapter 3 for fractal inclusions (3.3)-(3.8). The goal is defined to have permeability with real part equal to $4 \pm 2.5\%$ over frequency range of 410 - 470 MHz.

The optimal value for optimization variables are shown in Table 7.1, and the other parameters in this design are as follows: $\Delta y = 3.028mm, \Delta x = \Delta z = 20mm, \epsilon_r = 3.38, tan\delta = 0.0027$. The optimization process took 50,000 iterations. The resulted permeability for optimized inclusion is shown in Fig. 7.7. As shown in this figure, a permeability of $3.8 \pm 5\%$ for the frequency range of 430 - 470 MHz is achieved for the optimized multi-resonator configuration, which is highly flat comparing to single resonator structures.

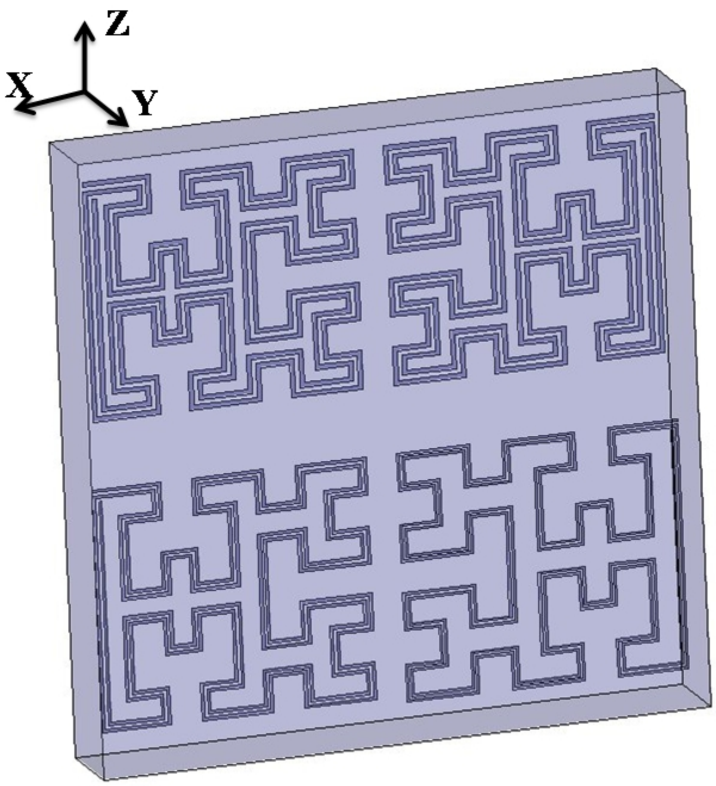

Figure 7.6: A unit cell with 4, 3rd order fractal Hilbert inclusions.

7.4.2 Analytically Optimized Unit Cell with 4 SRR Inclusions

To verify the idea for different type of inclusions, and different frequency band , here we do optimization for SRR inclusions operating at the frequency of 4 GHz. Fig. 7.8 illustrates the configuration. The R ,W,and S, (the radius of the SRR circle, width of metal strips, and space between them) for each resonator are selected as optimization variables. In this optimization, we again use the circuit model shown in Fig. 7.4, and genetic algorithm. The circuit parameters , R_i, C_i, L_i, G_i are calculated using equations presented in section 2.5.3. The goal is defined to have permeability with real part equal to $4 \pm 2.5\%$ over frequency range of 3.8 - 4.2 GHz.

The optimal values for optimization variables are shown in Table 7.1, and the other parameters in this design are as follows: $\Delta y = 4.7mm, \Delta x = \Delta z = 14.84mm, \epsilon_r = 2.43, tan\delta = 0.01$. The optimization process took 100,000 iterations. The resulted permeability for optimized inclusion is shown in Fig. 7.9. In this figure, analytical results are compared with numerical full wave results. In the full

Table 7.1: Optimal value for optimization variables.

Optimization Variable	Optimal Value
$l_{z_1}(mm)$	7.9
$W_1 = S_1(\mu m)$	200
$l_{z_2}(mm)$	7.9
$W_2 = S_2(\mu m)$	200
l_{z_3}	8.2
$W_3 = S_3(\mu m)$	76
$l_{z_4}(mm)$	8
$W_4 = S_4(\mu m)$	110

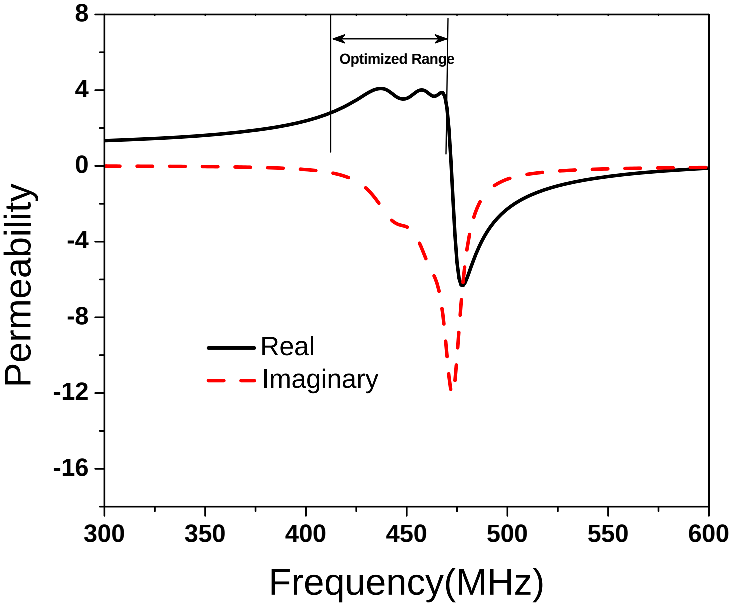

Figure 7.7: Resultant permeability of the optimized inclusion containing 4 inclusions with 3rd order fractal Hilbert configuration.

wave numerical analysis, the setup explained in chapter 2, and Ansoft HFSS 10, are used.

According to the analytical results shown in Fig. 7.9, a permeability of 4.2±7% for the frequency range of 3.9 - 4.08 GHz is achievable for the optimized multi-resonator configuration. However, the full wave numerical response of the analytically optimized designs have considerable deviation from desirable response. This can be due to the sensitivity of the optimized design, in which a little bit deviation

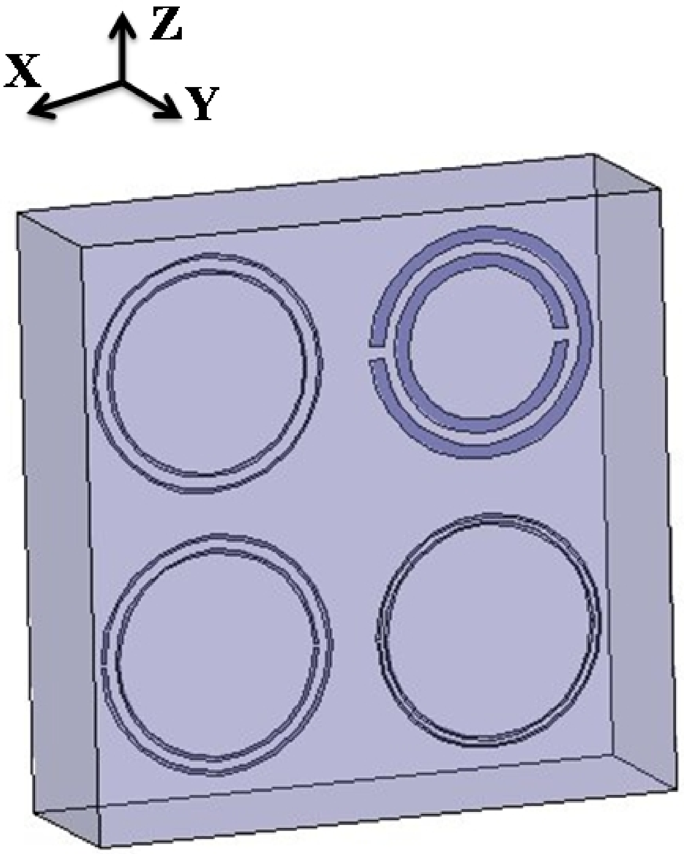

Figure 7.8: Circuit model for a unit cell with four resonators.

between the simulation and analytical results of one resonator distort the total response of the 4 resonators. In the next section, we try to address this challenge using Space mapping techniques [101]–[108].

7.5 Full Wave Optimization using Implicit Space Mapping

As observed in the previous section, the full wave numerical response of the analytically optimized designs have a considerable deviation from desirable response. However; it is impractical to do optimization directly in full wave analysis, because the full wave numerical analysis takes more than 5 hours for just one analysis, and more than 50,000 iterations are needed to get the final optimized results. Therefore, we use Space mapping technique to relate between analytical and numerical results.

Table 7.2: Optimal value for optimization variables for the design of Fig. 7.8.

Optimization Variable	Optimal Value
$R_1(mm)$	2.94
$W_1(\mu m)$	80
$S_1(\mu m)$	310
$R_2(mm)$	2.86
$W_2(\mu m)$	341
$S_2(\mu m)$	298
$R_3(mm)$	2.96
$W_3(\mu m)$	97
$S_3(\mu m)$	263
$R_4(mm)$	2.88
$W_4(\mu m)$	66
$S_4(\mu m)$	128

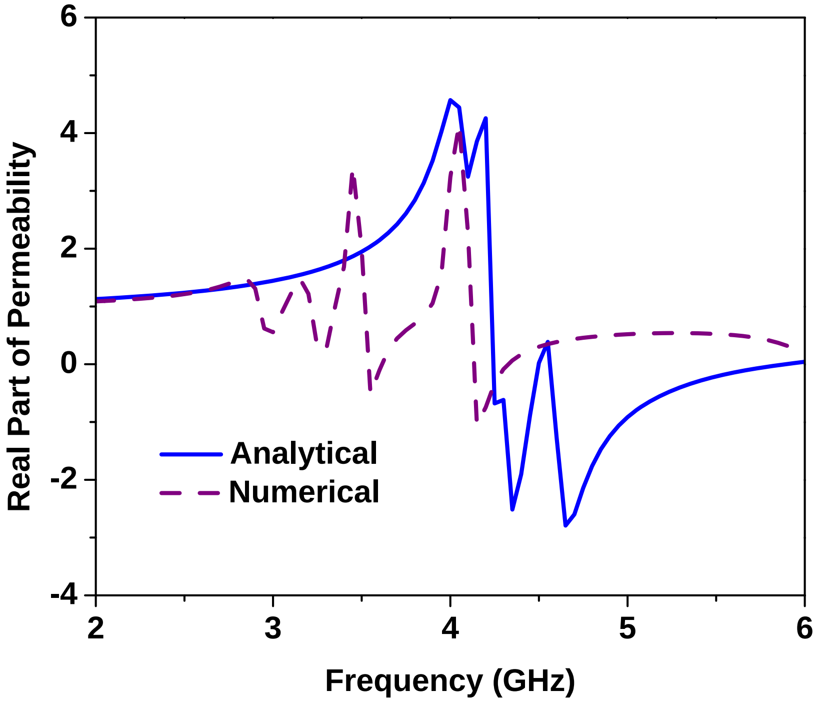

Figure 7.9: Permeability of the optimized inclusion containing 4 SRR. The analytical result is compared with numerical result.

Space Mapping (SM) is a optimization technique, in which a mapping is generated between two spaces [101]–[108]. One space is the optimization parameters in the analytical model, and another is optimization parameters in the full wave numerical analysis. The mapping corresponds a set of optimization parameters in analytical model, to another set of parameters in full wave analysis, such that the analytical results of the former set, will be equal to the numerical results of the later one.

Following the original concept of Space mapping introduced in 1993 by Bandler [101], lots of developments and updates are generated and reported in literature to accelerate the efficiency of the method such as: linear space mapping, aggressive space mapping [102],[103], trust regions method [108], utilization of artificial neural networks in space mapping [106], surrogate model [107], and implicit space mapping using preassigned parameters [104].

For the problem of optimization of multi-resonator structure, we tried linear space mapping, and aggressive space mapping [102],[103], without getting a desirable response. After investigating about different methods, and useful discussions with Dr. Bakr, and Dr. Bandler (the founder of Space Mapping method), we decided to use the implicit space mapping using preassigned parameters [104]. According to the nature of our problem, and the level of difference between analytical, and full wave results for one resonator, it seems that the implicit space mapping is the most promising technique among the all space mapping approaches. The details of this method is explained in [104]. In the following, we present the process, and results of applying implicit space mapping technique for our problem.

7.5.1 Problem Definition

A unit cell of the structure used for optimization is shown in Fig. 7.10. As shown in this figure, the unit cell contains 4 square SRR. The optimization variables are selected to be $l_i, W_i, and S_i, i = 1:4$, which are the length, width of strip, and space between the strips for each resonator. Therefore, 12 optimization variables are defined in this problem. The unit cell dimensions are selected as fixed parameters, as follows: $\Delta_y = 4mm, \Delta_x = 14mm, \Delta_z = 14mm$.

As explained in [104], in the implicit space mapping, some of the electrical and/or geometrical parameters are selected as preassigned parameters. These parameters are defined as tunable variables in the coarse model, while they are fixed in the fine model. The preassigned parameters are used to adjust the coarse model

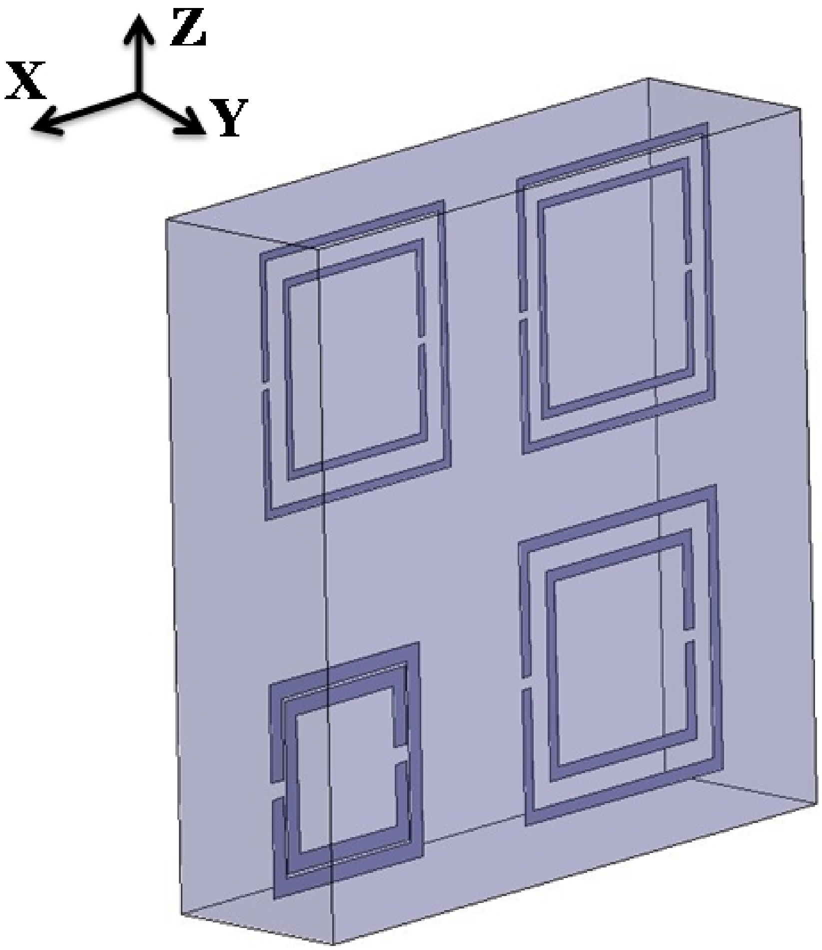

Figure 7.10: A unit cell of the structure used for implicit space mapping optimization.

response to the fine model response, and are updated in each iteration. Please see [104], for more details on preassigned parameters. In this problem, the relative permittivity and the loss tangent of the host substrate are selected as preassigned parameters. In the fine model, these parameters are fixed as $\epsilon_r = 2.2$, $tan\delta = 0.009$ which are the specifications of the Rogers RT/duroid 5880, material. However, in the coarse model, we assume that these parameters have different values for each resonator. Therefore, we have 8 preassigned parameters as follows: ϵ_{r_i}, $tan\delta_i, i = 1:4$. The relative permittivity, ϵ_{r_i}, is used to adjust the resonance frequency, and $tan\delta_i$ is used to adjust the magnitude of the resultant permeability. The goal of optimization is defined to have the permeability of $4 \pm 2.5\%$ over the frequency range of 3.2 - 3.6 GHz.

7.5.2 Optimization Results

Following the steps of optimization process as explained in [104], here the optimization results are presented. In the optimization process, for the coarse model, we use the circuit model shown in Fig. 7.4, and full wave numerical analysis as explained in chapter 2 is used as the fine model. In the full wave analysis, Ansoft HFSS 10, is used. In each iteration, as explained in [104], first the coarse model is optimized using genetic algorithm, and Agillent ADS software, then the optimal values are applied to full wave numerical analysis. The results of full wave analysis, and preassigned parameters are then used to adjust the circuit model, to have the same response as the full wave analysis. The updated circuit model is then optimized in the next iteration.

The results of this optimization, are presented in the following tables, and figures. Table 7.3, illustrates the optimal values of the optimization variables in each iteration, and Table 7.4 illustrates the values of the preassigned parameters in each iteration.

Table 7.3: Table of optimization variables in each iteration.

Iteration	l_1 mm	W_1 μm	S_1 μm	l_2 mm	W_2 μm	S_2 μm	l_3 mm	W_3 μm	S_3 μm	l_4 mm	W_4 μm	S_4 μm
1	5.82	413	525	5.32	59	173	5.14	59	103	5.62	173	462
2	6.14	83	472	5.04	98	410	4.64	168	205	5.78	163	537
3	5.8	579	366	5.18	177	490	5.32	77	298	5.20	209	498
...	...	...	...	...	...	...	...	...	...	...	...	...
6	5.54	180	396	5.36	175	482	4.32	345	69	5.72	256	490

Table 7.4: Table of preassigned parameters in each iteration.

Iteration	ϵ_{r_1}	$tan\delta_1$	ϵ_{r_2}	$tan\delta_2$	ϵ_{r_3}	$tan\delta_3$	ϵ_{r_4}	$tan\delta_4$
1	2.39	0.013	2.39	0.013	2.39	0.013	2.39	0.013
2	2.15	0.012	3.61	0.001	3.67	0.1	2.74	0.072
3	2.39	0.057	3.51	0.001	4.76	0.038	3.33	0.038
...	...	...	...	...	...	...	...	...
6	2.44	0.016	3.11	0.014	3.66	0.053	2.61	0.046

Figs. 7.11- 7.14 illustrate the optimized analytical (coarse model) and numerical

(fine model) responses at each iteration. The results of iterations 1-3, and iteration 6 which has the best achieved numerical response is shown in these figures. As shown in these figures, even the best achieved response has a considerable deviation from the desirable response. This deviation illustrates the limitation of the implicit space mapping method to work for this problem. Recently a new method has been reported in [105] that use tolerant Cauchy approximations to do space mapping-based optimization. Since in the mentioned method, Cauchy approximations are used to model the behavior of the numerical results, that method seems more promising for this problem. Applying Cauchy method to get better results can be considered as future work.

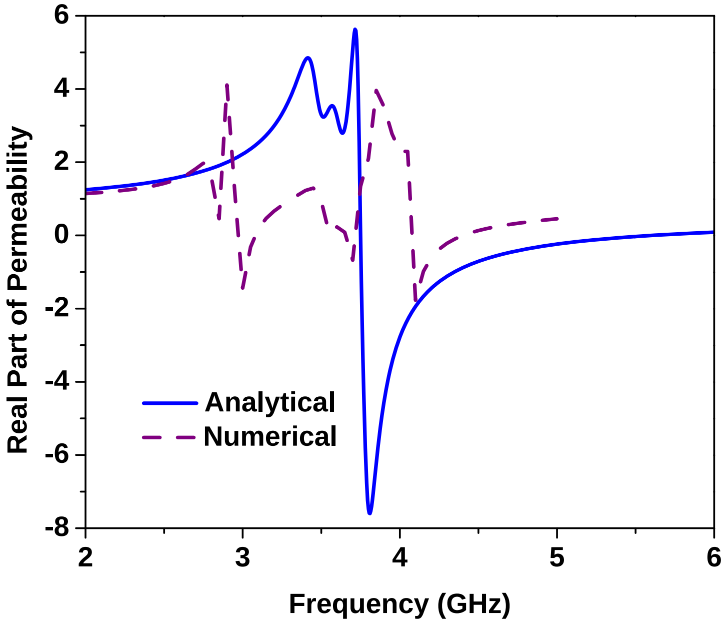

Figure 7.11: The optimization results at the iteration 1.

7.6 Conclusion

The idea of using multi-resonator structures as building blocks for artificial magnetic materials was introduced and investigated both analytically, and numerically. Numerical results show that by combining multiple inclusions with differen sizes in a unit cell, the magnetic properties of metamaterals can be extended to multiple frequency bands. circuit models were proposed to model multi-resonator structures, and verified through numerical full wave analysis. Using the circuit models,

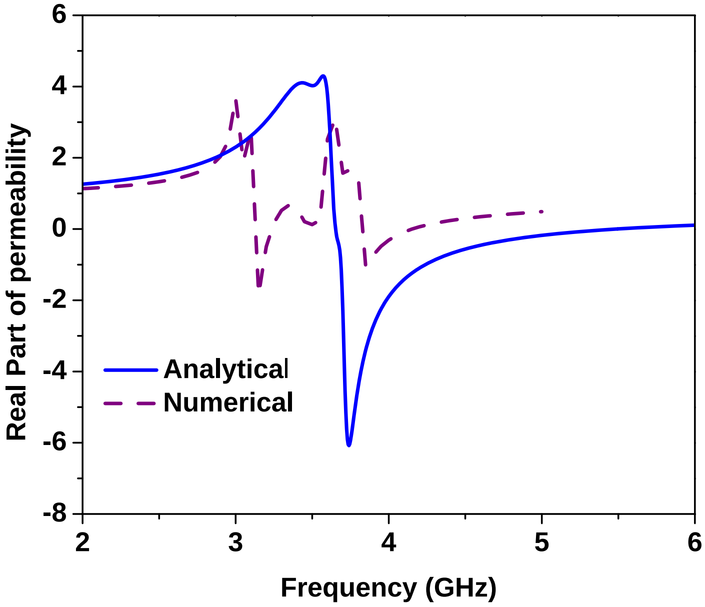

Figure 7.12: The optimization results at the iteration 2.

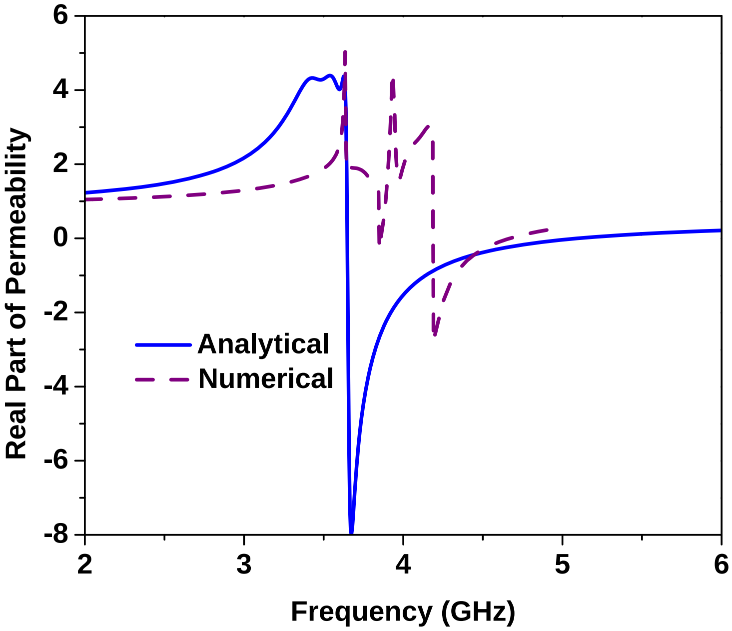

Figure 7.13: The optimization results at the iteration 3.

and implicit space mapping technique, multi-resonator structures were optimized to have a desirable response over a wide range of frequencies.

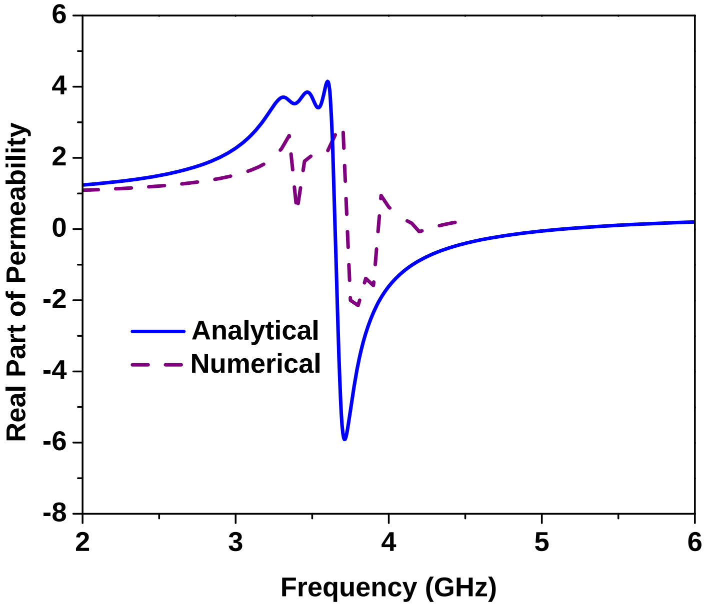

Figure 7.14: The optimization results at the iteration 6.

Chapter 8

Concluding Remarks

8.1 Summary and Thesis Contribution

In this thesis, several advances to the existing knowledge on the artificial magnetic materials have been developed, and presented including introducing of a new application, developing new structures for realization of these materials, developing two new methods for experimentally characterization, and parametric study of the performance of the miniaturized antenna using these materials as substrate.

As a new promising application, wide band artificial magnetic ground planes for the application of ultra-wide band low profile antennas, were introduced and investigated. Using a simple circuit model for mushroom-type EBG structures, it was shown that using magneto-dielectric materials as substrate can increase the in-phase reflection bandwidth of electromagnetic band gap (EBG) structures. To show this, a compact wideband EBG structure was designed and simulated. The numerical results show that this EBG has an in-phase reflection bandwidth of 70% which is several times greater than a conventional EBG resonating at the same frequency. Additionally, the new EBG surface has a smaller cell size, an important feature in the design of small antennas. As a demonstration of the effectiveness of the new structure, a low-profile unidirectional spiral antenna was designed to operate from 8 to 18 GHz. The improvement in the voltage standing wave ratio (VSWR) and gain of this antenna was presented while comparison was made to the case when using conventional EBG surface.

Novel configurations based on fractal Hilbert curves were proposed for realizing artificial magnetic materials. It was shown that the proposed configuration gives significant rise to miniaturization of artificial unit cells which in turn results in higher homogeneity in the material, and reduction in the profile of the artificial substrate. Analytical formulas were proposed for design and optimization of the presented structures, and were verified through full wave numerical characterization. The electromagnetic properties of the proposed structures were studied in detail and compared to the square spiral from the point of view of size reduction, maximum value of the resultant permeability, magnetic loss, and frequency dispersion. To validate the analytical model and the numerical simulation results, an artificial substrate containing second-order fractal Hilbert curve was fabricated and experimentally characterized. The fabricated artificial substrate was used as the substrate of a miniaturized antenna. The miniaturized antenna was measured, and reported. A miniaturization factor of 5.8 was achieved using the artificial substrate with fractal Hilbert inclusions. Measurement results of the miniaturized antenna, show a impedance bandwidth ($S11 < -10dB$) of 2.11%, the gain of -3.4 dBi at the boresight with the front-to-back ratio of 12.5 dB.

A New method was proposed to measure the effective constitutive parameters of artificial magnetic materials. The method was based on the microstrip line topology, thus making it easy to retrieve the constitutive parameters over a wide band of frequencies. The primary advantage of this method, when compared with previous methods, is its lower cost (in comparison to the free space or the waveguide methods) and its capability of extracting the permeability over a wide band of frequencies (in comparison to the resonator method). However, the method works only over the frequency range in which the permeability is positive. To demonstrate the effectiveness of this method, artificial magnetic materials with 2nd order fractal Hilbert inclusions were fabricated and characterized. Good agreement between the experimental and numerical simulation results validates the accuracy of the proposed method.

Another new experimental method based on strip line topology, was proposed for characterization of the effective constitutive parameters of metamaterials. This method has the same advantages of the microstrip line method over pervious methods, and also it works for all values of permittivity, and permeability. Therefore; this method is able to characterize all the 4 groups of metamaterials. Numerical simulation was done to express the effectiveness of the method for different types of metamaterials. Using numerical results, the effect of anisotropy on the accuracy of the results was investigated, and a fitting solution was proposed, and verified. The method was used to characterize artificial magnetic materials with 3rd order fractal Hilbert inclusions. Good agreement was obtained between the experimental results and numerical simulation results.

The use of artificial magnetic materials in the application of miniaturized antennas, was studied. A fast numerical simulation setup was proposed, and verified through measurement results. Using the numerical simulation, a parametric study was performed on the effect of constitutive parameters of the artificial material on the antenna specifications. In this study, the effect of the loss of the substrate over the gain, and efficiency of the antenna, and also the effect of the dispersion in the substrate over the antenna bandwidth were investigated.

The concept of using multiple inclusions in one unit cell was introduced, and investigated numerically. A circuit model was proposed for design, and optimization of a unit cell with multiple inclusions. Unit cells with four fractal inclusions, as well as four SRR inclusions were designed, and optimized to express a wide band flat permeability response. The analytically optimized unit cells, were analyzed numerically. Implicit Space mapping was used to make a link between optimal values in analytical optimization, and designs suitable for full wave analysis.

In summary, in this thesis the following contributions were achieved in the area of developing artificial magnetic materials:

- Introduced new application for magnetic materials: Low Profile Ultra Wide Band Antennas using EBG Structures with Magneto-Dielectric Materials.
- Introduced new structures for realization of artificial magnetic materials using fractal Hilbert curves, to provide miniaturization for these materials.
- Introduced new measurement method based on microstrip line fixture for characterization of artificial magnetic materials, which is less expensive, easier to fabricate, and needs smaller sample when compared to the previous measurement methods.
- Introduced new measurement method based on strip line line fixture for characterization of all kind of metamaterials, which has all the advantages of the microstrip method over the pervious methods, and furthermore it can be used for characterization of all four groups of metamaterials.
- Presented parametric study on the effect of the constitutive parameters of the artificial substrate on the specification of the miniaturized antennas.
- Introduced new unit cells with multiple inclusions for realization of multiband metamaterials, and applying optimization techniques to develop wide band artificial structures.

8.2 Future Work

Followings are some possible directions for the further research work:

- **Parametric study on the application of developing wide band artificial ground planes:**
  In this work, the magnetic material used in the application of developing wide band EBG was assumed to have a constant permeability. A possible research could be to study how dispersion and loss of the substrate could affect the in-phase reflection bandwidth of the resulted artificial magnetic ground plane.

- **Developing accurate analytical models for predication of the resultant permittivity of artificial magnetic materials:**
  Since artificial magnetic materials are designed to provide desirable permeability results, all the pervious works including this work are focused on the analysis, and modeling of the resultant permeability. However, it was shown in the literature, and also in this work that the metallic inclusions change the resultant permittivity of the medium as well. The resultant permittivity can be extracted using the simulation setup, and measurement methods explained in this work. However, it can't be calculated using analytical models. It looks interesting, to derive accurate formulas or circuit models to calculate the resultant permittivity.

- **Developing general formulas in terms of geometric properties to compensate for the anisotropy effect in the proposed measurement method using strip line fixture:**
  In Chapter 5, where a new measurement method was proposed to characterize metamaterials, two formulas were derived to compensate the affect of anisotropy. The compensating formulas were derived for specific geometrical properties such as the height of the substrate, and the width of the strip line, used in this work. The process for derivation of these formulas are explained in the thesis clearly, and can be repeated for any other strip line fixture with different geometrical parameters. However, it can be considered as a future research work, to repeat this process for different values of geometrical parameters, and derive analytical formulas in terms of these geometrical parameters.

- **Applying space mapping-based optimization exploiting Cauchy approximations technique for optimization of the unit cell with mul-**

tiple inclusions:

In Chapter 7, implicit space mapping technique was used for optimization of multi-resonator unit cells to achieve a flat response for permeability over a specific frequency band. However the results of optimization had a considerable deviation from the optimization goal. As a future research work, the recently proposed method, space mapping-based optimization exploiting tolerant Cauchy approximations [105], can be used to optimize the multi-resonator structures. Since Cauchy approximations are used in this method to model the behavior of the numerical results, the method tends to be promising for the problem of multi-resonator unit cells.

References

[1] K. Buell, H. Mosallaei, and K. Sarabandi, “A substrate for small patch antennas providing tunable miniaturization factors,” *IEEE Trans. Microwave Theory Tech.*, vol. 54, pp. 135–146, Jan. 2006. xi, 2, 10, 18, 32, 33, 46, 52, 75, 81, 84

[2] M. A. Saville, *M.S. Thesis on investigation of conformal high-impedance ground planes.* Air force institute of technology Wright Patterson AFB, 2000. xi, 14, 15

[3] S. Maslovski, P. Ikonen, I. Kolmakov, and S. Tretyakov, “Artificial magnetic materials based on the new magnetic particle: Metasolenoid,” *Progress In Electromagnetics Research(PIER)*, vol. 54, no. 9, pp. 61–81, Sep. 2005. xii, 2, 3, 26

[4] V. G. Veselago, “The electrodynamics of substances with simultaneously negative values of ϵ and μ,” *Soviet Phys. Usp.*, vol. 10, pp. 509–514, 1968. 1

[5] N. Engheta and R. W. Ziolkowski, *Metamaterials: Physics and Engineering Explorations.* Wiley-IEEE Press, 2006. 1

[6] G. V. Eleftheriades, *Negative-Refraction Metamaterials.* John Wiley and Sons, 2006.

[7] J. B. Pendry, “Negative refraction makes perfect lens,” *Phys. Rev. Lett.*, vol. 85, pp. 3966–3969, Oct. 2000. 1

[8] N. Engheta, “An idea for thin subwavelength cavity resonators using metamaterials with negative permittivity and permeability,” *IEEE Antenna Wireless Propagat. Lett.*, vol. 1, no. 1, pp. 10–13, Jun. 2002. 1

[9] A. Alu and N. Engheta, “Guided modes in a waveguide filled with a pair of singlenegative (sng), double-negative (dng), and/or double-positive (dps)

layers," *IEEE Trans. Microwave Theory Tech.*, vol. 52, no. 1, pp. 199–210, Jan. 2004.

[10] S. Hrabar, J. Bartolic, and Z. Sipus, "Experimental investigation of subwavelength resonator based on backward metamaterials," in *the Proceeding of IEEE AP-S Int. Symp. Antennas Propagat.*, vol. 3, Jun. 2004, pp. 2568 – 2571. 1

[11] A. Alu and N. Engheta, "Polarizabilities and effective parameters for collections of spherical nano-particles formed by pairs of concentric double-negative (dng), singlenegative (sng)and/or double-positive (dps) metamaterial layers," *J. Appl. Phys.*, vol. 97, no. 1, p. 094310, May 2005. 1

[12] R. W. Ziolkowski and A. Kipple, "Application of double negative metamaterials to increase the power radiated by electrically small antennas," *IEEE Trans. Antennas Propagat.*, vol. 51, no. 10, p. 2626 2640, Oct. 2003. 1

[13] M. S. Boybay and O. M. Ramahi, "Near-field probes using double and single negative media," *Phys. Rev. E*, vol. 79, p. 016602, Jan. 2009. 1

[14] M. Boybay and O. M. Ramahi, "Evanescent field detection using negative refractive index lenses," in *the Proceeding of IEEE AP-S Int. Symp. Antennas Propagat.*, vol. 1B, Jun. 2007, pp. 5507–5510.

[15] ——, "Near-field probes using double and single negative media," in *the proceeding of NATO Advanced Research Workshop: Metamaterials for Secure Information and Communication Technologies*, vol. 1B, May 2008, pp. 725–731. 1

[16] K. Buell, H. Mosallaei, and K. Sarabandi, "Electromagnetic metamaterial insulator to eliminate substrate surface waves," in *the Proceeding of IEEE AP-S Int. Symp. Antennas Propagat.*, vol. 2A, Jul. 2005, pp. 574–577. 1

[17] M. M. Bait-Suwailam, M. S. Boybay, and O. Ramahi, "Mutual coupling reduction in mimo antennas using artificial magnetic materials," in *International symposium on antenna technology and applied electromagnetics (antem/ursi)*, vol. 1B, 2009.

[18] ——, "Single-negative (SNG) metamaterials for mutual coupling reduction in high-profile antennas," in *the Proceeding of IEEE AP-S Int. Symp. Antennas Propagat.*, vol. 1B, Jun. 2009. 1

[19] K. N. Rozanova, Z. W. Li, L. F. Chen, and M. Y. Koledintseva, "Microwave permeability of co2z composites," *J. Appl. Phys.*, vol. 97, pp. 013 905–1–013 905–7, Dec. 2004. 1

[20] A. L. Adenot, O. Acher, T. Taffary, and L. Longuet, "Sum rules on the dynamic permeability of hexagonal ferrites," *J. Appl. Phys.*, vol. 91, pp. 7601–7603, May 2002.

[21] O. Acher and A. L. Adenot, "Bounds on the dynamic properties of magnetic materials," *Phys. Rev. B*, vol. 62, no. 17, pp. 11 324–11 327, Nov. 2000.

[22] W. D. Callister, *Materials science and engineering,an introduction.* John Wiley and Sons Inc, 2000. 1, 9

[23] M. V. Kostin and V. V. Shevchenko, "Artificial magnetics based on double circular elements," in *the proceeding of bian-isotropics'94, perigueux*, May 1994, pp. 49–56. 2, 13, 18

[24] J. B. Pendry, A. J. Holden, D. J. Robbins, and W. J. Stewart, "Magnetism from conductors and enhanced nonlinear phenomena," *IEEE Trans. Microwave Theory Tech.*, vol. 47, no. 11, pp. 2075–2084, Nov. 1999. 2

[25] R. Marques, F. Medina, and R. Rafii-El-Idrissi, "Role of bianisotropy in negative permeability and left-handed metamaterials," *Phys. Rev. B*, vol. 65, no. 14, pp. 44 401–44 405, Apr. 2002. 2, 13, 18

[26] L. Yousefi and O. Ramahi, "Engineered magnetic materials with improved dispersion using multi-resonator structures," in *Electrical and Computer Engineering, 2007. CCECE 2007. Canadian Conference on*, Apr 2007, pp. 966–969.

[27] ——, "Experimental retrieval of the effective parameters of artificial magnetic materials based on a the microstrip line method," in *Antennas and Propagation Society International Symposium, 2008. AP-S 2008. IEEE*, Jul 2008, pp. 1–4. 54

[28] L. Yousefi, B. Mohajer-Iravani, and O. Ramahi, "Low profile wide band antennas using electromagnetic bandgap structures with magneto-dielectric materials," in *Antenna Technology: Small and Smart Antennas Metamaterials and Applications, 2007. IWAT '07. International Workshop on*, Mar 2007, pp. 431–434. 2

[29] K. Buell, *PhD Theis on development of engineered magnetic materials for antenna applications.* ECE Department of University of Michigan, 2005. 76

[30] J. D. Baena, R. Marques, F. Medina, and J. Martel, “Artificial magnetic metamaterial design by using spiral resonators,” *Phys. Rev. B*, vol. 69, pp. 144 021–144 025, Jan. 2004. 2, 28, 32, 33

[31] P. M. T. Ikonen, S. I. Maslovski, C. R. Simovski, and S. A. Tretyakov, “On artificial magnetodielectric loading for improving the impedance bandwidth properties of microstrip antennas,” *IEEE Trans. Antennas Propagat.*, vol. 54, no. 6, pp. 1654–1662, Jun. 2006. 2, 32, 52, 75

[32] R. C. Hansen, and M. Burke, “Antennas with magneto-dielectrics,” *Microwave and Optic. Tech. Letts.*, vol. 26, no. 2, pp. 75–78, Jun. 2000. 2, 76

[33] A. Buerkle, and K. Sarabandi, “A circularly polarized magneto-dielectric resonator antenna with wideband, multi-resonant response,” in *the Proceeding of IEEE AP-S Int. Symp. Antennas Propagat.*, vol. 1B, Jul. 2005, pp. 487–490. 2

[34] K. Min, T. V. Hong, and D. Kim, “A design of a meander line antenna using magneto-dielectric material for RFID system,” in *the proceedings of asia-pacific conference on microwave*, vol. 4, Dec. 2005, pp. 1–4. 2

[35] A. Foroozesh, and L. Shafai, “Size reduction of a microstrip antenna with dielectric superstrate using meta-materials: artificial magnetic conductors versus magneto-dielectrics,” in *the Proceeding of IEEE AP-S Int. Symp. Antennas Propagat.*, vol. 1B, Jul. 2006, pp. 11–14. 2

[36] L. Yousefi, B. Mohajer-Iravani, and O. M. Ramahi, “Enhanced bandwidth artificial magnetic ground plane for low profile antennas,” *IEEE Antenna Wireless Propagat. Lett.*, vol. 6, pp. 289 – 292, Jun. 2007. 2

[37] H. Mosallaei, and K. Sarabandi, “Magneto-dielectrics in electromagnetics: concept and applications,” *IEEE Trans. Antennas Propagat.*, vol. 52, no. 6, pp. 1558 – 1567, Jun. 2004. 2

[38] S. A. Schelkunoff and H. T. Friis, *Antennas: theory and practise.* John Wiley and Sons Inc, 1952. 2

[39] A. Ishimaru, S. Lee, Y. Kuga, and V. Jandhyala, “Generalized constitutive relations for metamaterials based on the quasi-static lorentz theory,” *IEEE Trans. Antennas Propagat.*, vol. 51, no. 10, pp. 2550–2557, Oct. 2003. 2

[40] M. G. Silverinha, “A metamaterial homogenization approach with application to the characterization of micro-structured composites with negative parameters,” *Physical Review Letter B*, Mar. 2003. 2

[41] D. R. Smith and J. B. Pendry, “Homogenization of metamaterials by field averaging,” *Journal of Opt. Soc. Am. B*, vol. 23, no. 3, pp. 391–403, Mar. 2006. 2

[42] L. Chen, C. K. Ong, and B. T. G. Tan, “Cavity perturbation technique for the measurement of permittivity tensor of uniaxially anisotropic dielectrics,” *IEEE Trans. Instrum. Meas*, vol. 48, pp. 1023–1030, Dec. 1999. 3, 43

[43] K. Buell and K. Sarabandi, “A method for characterizing complex permittivity and permeability of meta-materials,” in *the Proceeding of IEEE AP-S Int. Symp. Antennas Propagat.*, vol. 2, Jun. 2002, pp. 408–411. 3, 43

[44] R. B. Greegor, C. G. Parazzoli, K. Li, B. E. C. Koltenbah, and M. Tanielian, “Experimental determination and numerical simulation of the properties of negative index of refraction materials,” *Optics Express*, vol. 11, pp. 688–695, Apr. 2003. 3, 43, 55

[45] A. F. Starr, P. M. Rye, D. R. Smith, and S. Nemat-Nasser, “Fabrication and characterization of a negative-refractive-index composite metamaterial,” *Phys. Rev. B*, vol. 70, p. 113102, Sep. 2004. 43

[46] D. R. Smith, D. Schurig, and J. J. Mock, “Characterization of a planar artificial magnetic metamaterial surface,” *Phys. Rev. E*, vol. 74, p. 036604, Sep. 2006. 3, 43, 55

[47] N. J. Damascos, R. B. Mack, A. L. Maffett, W. Parmon, and P. L. E. Uslenghi, “The inverse problem for biaxial materials,” *IEEE Trans. Microwave Theory Tech.*, vol. 32, no. 4, pp. 400–405, Apr. 1984. 3, 43, 44

[48] H. Chen, J. Zhang, Y. Bai, Y. Luo, L. Ran, Q. Jiang, and J. A. Kong, “Experimental retrieval of the effective parameters of metamaterials based on a waveguide method,” *Optics Express*, vol. 14, no. 26, pp. 12 944–12 949, Dec. 2006. 3, 43, 44

[49] F. Yang and Y. Rahmat-Samii, “Reflection phase characterizations of the ebg ground plane for low profile wire antenna applications,” *IEEE Trans. Antennas Propagat.*, vol. 51, no. 10, p. 2691 2703, Oct. 2003. 11, 13, 16

[50] Z. Li and Y. Rahmat-Samii, “Pbg, pmc and pec ground planes: A case study of dipole antennas,” in *the Proceeding of IEEE AP-S Int. Symp. Antennas Propagat.*, vol. 2, Jul. 2000, p. 674 677. 11, 16

[51] J. M. Bell and M. F. Iskander, “A low-profile archimedean spiral antenna using an ebg ground plane,” *IEEE Antenna Wireless Propagat. Lett.*, vol. 3, pp. 223–226, Jun. 2004. 11

[52] T. H. Liu, W. X. Zhang, M. Zhang, and K. F. Tsang, “Low profile spiral antenna with pbg substrate,” *Electron. Letts.*, vol. 36, no. 4, p. 779 780, Apr. 2000. 11

[53] D. Sievenpiper, *Ph.D. dissertation on high-impedance electromagnetic surfaces.* Deptartment of Electrical Engineering, University of California at Los Angeles, 1999. 12, 15, 16

[54] S. A. Tretyakov, *Analytical Modeling in Applied Electromagnetics.* Artech House, 2003. 12

[55] S. A. Tretyakov and C. R. Simovski, “Dynamic model of artificial reactive impedance surfaces,” *J. Electromag. Waves and Apps.*, vol. 17, no. 1, pp. 131–145, Jun. 2003. 13

[56] R. C. Hansen, “Effects of a high-impedance screen on a dipole antenna,” *IEEE Antenna Wireless Propagat. Lett.*, vol. 1, pp. 46–49, Jun. 2002. 13

[57] H. Nakano, K. Nogami, S. Arai, H. Mimaki, and J. Yamauchi, “A spiral antenna backed by a conducting plane reflector,” *IEEE Trans. Antennas Propagat.*, vol. 34, no. 6, pp. 791–796, Jun. 1986. 16

[58] X. Chen, T. M. Grzegorczyk, B. Wu, J. Pacheco, and J. A. Kong, “Robust method to retrieve the constitutive effective parameters of metamaterials,” *Phys. Rev. E*, vol. 70, no. 1, pp. 016 608.1–016 608.7, Jul. 2004. 24

[59] R. W. Ziolkowski, “Design, fabrication, and testing of double negative metamaterials,” *IEEE Trans. Antennas Propagat.*, vol. 51, no. 7, pp. 1516 – 1529, Jul. 2003. 24

[60] R. Schinzinger and P. A. A. Laura, *AConformal mapping: methods and applications.* Elsevier, 1991. 28, 37

[61] S. Ramo, J. R. Whinnery, and T. V. Duzer, *Fields and waves in communication electronics.* John Wiley and Sons, 1994.

[62] C. R. Paul, *Analysis of multiconductor transmission lines.* John Wiley and Sons, 1994.

[63] H. Kober, *Dictionary of conformal representations.* Dover Publications, 1957. 28

[64] M. K. Karkkainen, S. A. Tretyakov, and P. Ikonen, "Numerical study of pifa with dispersive material fillings," *Microwave and Optic. Tech. Letts.*, vol. 45, no. 1, pp. 5–8, Feb. 2005. 32, 75, 81

[65] M. E. Ermutlu, C. R. Simovski, M. K. Karkkainen, P. Ikonen, S. A. Tretyakov, and A. A. Sochava, "Miniaturization of patch antennas with new artificial magnetic layers," in *the proceeding of IEEE international workshop on antenna technology*, vol. 1B, Mar. 2005, pp. 87–90.

[66] L. Yousefi and O. Ramahi, "Miniaturized wideband antenna using engineered magnetic materials with multi-resonator inclusions," in *Antennas and Propagation Society International Symposium, 2007 IEEE*, Jun 2007, pp. 1885–1888.

[67] P. Ikonen, S. Maslovski, and S. Tretyakov, "Pifa loaded with artificial magnetic material: Practical example for two utilization strategies," *Microwave and Optic. Tech. Letts.*, vol. 46, no. 3, pp. 205–210, Jun. 2005.

[68] M. K. Karkkainen and P. Ikonen, "Patch antenna with stacked split-ring resonators as artificial magnetodielectric substrate," *Microwave and Optic. Tech. Letts.*, vol. 46, no. 6, pp. 554–556, Jul. 2005. 32, 75, 81

[69] H. Mosallaei and K. Sarabandi, "Design and modeling of patch antenna printed on magneto-dielectric embedded-circuit metasubstrate," *IEEE Trans. Antennas Propagat.*, vol. 55, pp. 45–52, Jan. 2007. 32, 33

[70] P. M. T. Ikonen and S. A. Tretyakov, "Comments on design and modeling of patch antenna printed on magneto-dielectric embedded-circuit metasubstrate," *IEEE Trans. Antennas Propagat.*, vol. 55, pp. 2935–2936, Oct. 2007.

[71] H. Mosallaei and K. Sarabandi, “Reply to comments on design and modeling of patch antenna printed on magneto-dielectric embedded-circuit metasubstrate,” *IEEE Trans. Antennas Propagat.*, vol. 55, pp. 2936–2937, Oct. 2007. 32, 33

[72] A. Erentok, R. W. Ziolkowski, J. A. Nielsen, R. B. Greegor, C. G. Parazzoli, M. H. Tanielian, S. A. Cummer, B.-I. Popa, T. Hand, D. C. Vier, and S. Schultz, “Low frequency lumped element-based negative index metamaterial,” *Appl. Phys. Lett.*, vol. 91, pp. 1 841 041–1 841 043, Nov. 2007. 32, 33

[73] E. A. Parker and A. N. A. E. Sheikh, “Convoluted array elements and reduced size unit cells for frequency-selective surfaces,” in *the proceeding of Inst. Elect. Eng.Microw., Antennas, Propag.*, vol. 138, 1991, pp. 19–22. 33

[74] J. McVay, A. Hoorfar, and N. Engheta, “Peano high-impedance surfaces,” in *the Proceeding of Radio Sci.*, vol. 40, 2005. 33

[75] J. McVay, N. Engheta, and A. Hoorfar, “Numerical study and parameter estimation for double-negative metamaterials with hilbert-curve inclusions,” in *the Proceeding of IEEE AP-S Int. Symp. Antennas Propagat.*, vol. 2B, Jul. 2005, pp. 328–331. 33

[76] V. Crnojevic-Bengin, V. Radonic, and B. Jokanovic, “Fractal geometries of complementary split-ring resonators,” *IEEE Trans. Microwave Theory Tech.*, vol. 56, no. 10, pp. 2312–2321, Oct. 2008. 33

[77] V. Pierro, J. McVay, V. Galdi, A. Hoorfar, N. Engheta, and I. M. Pinto, “Metamaterial inclusions based on grid-graph hamiltonian paths,” *Microwave and Optic. Tech. Letts.*, vol. 48, no. 12, pp. 2520–2524, Dec. 2006. 33

[78] J. Franklin and A. Daoud, *Proof in mathematics: an introduction.* Quakers Hill Press, 1996. 36, 37

[79] A. Kabiri, L. Yousefi, and O. M. Ramhi, “Magnetic loss tangent optimization in design of artificial magnetic slabs,” in *the Proceeding of IEEE AP-S Int. Symp. Antennas Propagat.*, Jul 2008. 38

[80] ——, “On the fundamental limitations of artificial magnetic material,” in *Proceeding of NATO Advanced Research Workshop in Marrakesh Morocco*, May 2008. 38

[81] J. Baker-Jarvis, E. J. Vanzura, and W. A. Kissick, "Improved technique for determining complex permittivity with the transmission/reflection method," *IEEE Trans. Microwave Theory Tech.*, vol. 38, no. 8, pp. 1096–1103, Aug. 1990. 44

[82] P. Queffelec, P. Gelin, J. Gieraltowski, and J. Loaec, "A microstrip device for the broad band simultaneous measurement of complex permeability and permittivity," *IEEE Transactions on Magnetics*, vol. 30, no. 2, pp. 224–231, Mar. 1994.

[83] Y. Heping, K. Virga, and J. Prince, "Dielectric constant and loss tangent measurement using a stripline fixture," *IEEE Trans. on Advanced Packaging*, vol. 21, pp. 441–446, Nov. 1999.

[84] J. Hinojosa, L. Faucon, P. Queffelec, and F. Huret, "S-parameter broadband measurements of microstrip lines and extraction of the substrate intrinsic properties," *Microwave and optical technology letters*, vol. 30, no. 1, pp. 65–69, Jul. 2001.

[85] V. Bekker, K. Seemann, and H. Leiste, "A new strip line broad-band measurement evaluation for determining the complex permeability of thin ferromagnetic films," *Journal of Magnetism and Magnetic Materials*, vol. 270, no. 3, pp. 327–332, Mar. 2004.

[86] J. Hinojosa, "Permittivity characterization from open-end microstrip line measurements," *Microwave and Optical Technology Letters*, vol. 49, no. 6, pp. 1371–1374, Jun. 2007. 44

[87] H. A. Wheeler, "Transmission-line properties of parallel strips separated by a dielectric sheets," *IEEE Trans. Microwave Theory Tech.*, vol. 13, no. 2, pp. 172–185, Mar. 1965. 45, 47

[88] R. A. Pucel and D. J. Masse, "Microstrip propagation on magnetic substrates," *IEEE Trans. Microwave Theory Tech.*, vol. 20, pp. 304–313, May 1972. 45, 46, 47

[89] L. Yousefi and O. M. Ramahi, "New artificial magnetic materials based on fractal hilbert curves," *Proceeding of IWAT07*, pp. 237–240, 2007. 46, 49, 52

[90] J. E. Dennis and R. B. Schnabel, *Numerical methods for unconstrained optimization and nonlinear equations.* New Jersey, USA: Prentice-Hall, 1983. 47

[91] L. Yousefi, H. Attia, and O. M. Ramahi, "Broadband experimental characterization of artificial magnetic materials based on a microstrip line method," *Journal of Progress In Electromagnetics Research(PIER)*, vol. 90, pp. 1–13, Feb. 2009. 54

[92] D. M. Pozar, *Microwave Engineering, 2nd Edition.* John Wiley and Sons, 1998. 56

[93] R. W. Ziolkowski, "Design, fabrication, and testing of double negative metamaterials," *IEEE Trans. Antennas Propagat.*, vol. 51, no. 7, pp. 1516–1529, Jul. 2003. 59

[94] A. F. Starr, P. M. Rye, D. R. Smith, and S. Nemat-Nasser, "Fabrication and characterization of a negative-refractive-index composite metamaterial," *Physical Review B*, vol. 70, p. 113102, 2004. 74

[95] S. Maslovski, P. Ikonen, I. Kolmakov, and S. Tretyakov, "Artificial magnetic materials based on the new magnetic particle: Metasolenoid," *Progress In Electromagnetics Research(PIER)*, vol. 54, pp. 61–81, 2005. 74

[96] D. R. Smith, D. Schurig, and J. J. Mock, "Characterization of a planar artificial magnetic metamaterial surface," *Physical Review E*, vol. 74, p. 036604, 2006. 74

[97] H. Chen, J. Zhang, Y. Bai, Y. Luo, L. Ran, Q. Jiang, and J. A. Kong, "Experimental retrieval of the effective parameters of metamaterials based on a waveguide method," *Optics Express*, vol. 14, no. 26, pp. 12 944–12 949, 2006. 74

[98] R. B. Greegor, C. G. Parazzoli, K. Li, B. E. C. Koltenbah, and M. Tanielian, "Experimental determination and numerical simulation of the properties of negative index of refraction materials," *Optics Express*, vol. 11, pp. 688–695, 2003. 74

[99] J. S. Colburn and Y. Rahmat-Samii, "Patch antennas on externally perforated high dielectric constant substrates," *IEEE Trans. Antennas Propagat.*, vol. 47, no. 12, p. 1785 1794, Dec. 1999. 76

[100] Y. Hwang, Y. P. Zhang, G. Zheng, and T. K. C. Lo, "Planar inverted f antenna loaded with high permittivity material," *Electron. Letts.*, vol. 31, no. 20, pp. 1710–1712, Sep. 1995. 76

[101] J. Bandler, R. Biernacki, S. H. Chen, P. Grobelny, and R. Hemmers, "Space mapping technique for electromagnetic optimization," *Microwave Theory and Techniques, IEEE Transactions on*, vol. 42, no. 12, pp. 2536–2544, Dec 1994. 88, 96, 98

[102] J. Bandler, R. Biernacki, S. H. Chen, R. Hemmers, and K. Madsen, "Electromagnetic optimization exploiting aggressive space mapping," *Microwave Theory and Techniques, IEEE Transactions on*, vol. 43, no. 12, pp. 2874–2882, Dec 1995. 98

[103] M. Bakr, J. Bandler, N. Georgieva, and K. Madsen, "A hybrid aggressive space-mapping algorithm for em optimization," *Microwave Theory and Techniques, IEEE Transactions on*, vol. 47, no. 12, pp. 2440–2449, Dec 1999. 98

[104] J. Bandler, Q. Cheng, N. Nikolova, and M. Ismail, "Implicit space mapping optimization exploiting preassigned parameters," *Microwave Theory and Techniques, IEEE Transactions on*, vol. 52, no. 1, pp. 378–385, Jan 2004. 98, 99, 100

[105] G. Shaker, M. Bakr, N. Sangary, and S. Safavi-Naeini, "Space mapping-based optimization exploiting tolerant cauchy approximations," in *Microwave Symposium Digest, 2009. MTT '09. IEEE MTT-S International*, Jun 2009, pp. 521–524. 101, 108

[106] M. Bakr, J. Bandler, M. Ismail, J. Rayas-Sanchez, and Q.-J. Zhang, "Neural space-mapping optimization for em-based design," *Microwave Theory and Techniques, IEEE Transactions on*, vol. 48, no. 12, pp. 2307–2315, Dec 2000. 98

[107] M. Bakr, J. Bandler, K. Madsen, J. Rayas-Sanchez, and J. Sondergaard, "Space-mapping optimization of microwave circuits exploiting surrogate models," *Microwave Theory and Techniques, IEEE Transactions on*, vol. 48, no. 12, pp. 2297–2306, Dec 2000. 98

[108] M. Bakr, J. Bandler, R. Biernacki, S. Chen, and K. Madsen, "A trust region aggressive space mapping algorithm for em optimization," in *Microwave Symposium Digest, 1998 IEEE MTT-S International*, vol. 3, Jun 1998, pp. 1759–1762 vol.3. 88, 96, 98

[109] R. J. Cameron, R. Mansour, and C. M. Kudsia, *Microwave Filters for Communication Systems : Fundamentals, Design and Applications.* John Willey and Sons, 2007. 92